Vienna University of Technology

Ph.D. Thesis

Oxygen Reduction and Carbon Monoxide Oxidation on Pt
- from Model to Real Systems for Fuel Cell Electrocatalysis

accomplished to fulfill the requirements for the degree of a
"Dr. techn." under the special direction of

Univ. Prof. DI Dr. techn. Christoph Fabjan

E164 - Institute for Chemical Technologies and Analysis

performed at the Lawrence Berkeley National Laboratory
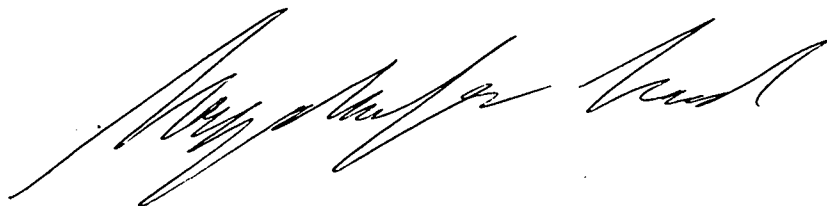Material Science Division; Berkeley CA, USA
Submitted at the Vienna University of Technology,
Faculty of Technical Chemistry by

DI Karl J.J. Mayrhofer
Mat. Nr. E9625999
Adlerstr. 34, 9523 Landskron

Vienna, December 2005

1st Reviewer: Professor Univ. Prof. DI Dr. C. Fabjan

2nd Reviewer: Professor AO Univ. Prof. Dr. phil. H. Vinek

Date of the exam: January 16, 2005

Die lohnensten Erfindungen sind diejenigen, welche, indem sie den Denker erfreun, zugleich der Menscheit nützen.

The most rewarding inventions are those, which, by delighting the thinker, at the same time yield profit to mankind.

Christian Doppler   (1803-1853)

Objective of the Work

The objective of this work is to investigate the somewhat edged out fundamental knowledge gained from single crystal model systems and link certain aspects to the features of high-surface area catalysts, in order to demonstrate the importance of fundamental research and create a connection to practical applications. This is achieved by treating the ideal systems not as "one-to-one" models, but rather rationalize the effects that can be correlated to real catalysts, while always keeping the structural and electronic differences in mind. In this regard important fuel cell reactions such as the CO oxidation and oxygen reduction are investigated, and novel insights into the origin of the particle size effects are demonstrated. Based on this information from Pt systems more complicated catalysts like the promising Pt-alloys can be analyzed unambiguously. With the variety of systems discussed in this work, it can be considered as a benchmark for the further development of novel catalysts. Moreover the presented perception resulting from the applied "surface science approach" reflects the state of the art for the complex electrocatalysis of fuel cell reactions, and can consequently be supportive for everybody in the field, to researchers in industry as well as at university.

Preface

Already during the early days of my studies at the TU Vienna, a time when the public environmental conscience was improving and topics such as global warming were heavily discussed, I was able to satisfy my personal interests therein by taking some of the great variety of elective courses offered back then, such as "Climate Research" or "Energy Technologies". Especially fuel cells as an alternative mean for energy conversion caught my eye, so I focused more on the basic electrochemistry in courses by Prof. Lechner and Prof. Fabjan and further in a course of "Advanced Electrochemistry" by A.J. Bard during a year abroad at the University of Texas in Austin. With a summer internship and my Masters Thesis one year later at Ballard Power Systems, one of the leading PEM fuel cell companies, I could gain hands-on experience from the production to the testing of fuel cells at the state of the art. Despite the exaggerated confidentiality policy in particular against student employees, my supervisors V. Peinecke, A. Muetschele, S. Limmer and C. Cremer, besides others, helped me improving in the field and writing a decent thesis [1]. Furthermore I realized the still unresolved issues that prevent the current commercialization of the technology, and decided to go back to University to investigate the basics of electrocatalysis on a more fundamental level. Thanks to my unbureaucratic supervisor of this PhD Thesis at the TU Vienna Prof. Fabjan, and the partial financial support of the Austrian government (scholarship by the BMBWK), I was able to join the internationally well-known research group of Phil Ross and Nenad Markovic at the Lawrence Berkeley National Laboratory in the USA for two years to work independently on my thesis. My work has been build on the excellent preceding work of the previous group members Hubert Gasteiger, Thomas J. Schmidt and Ursula Paulus and all active members. Great support came from Matthias Arenz who taught me how to perform reproducible electrochemical and in-situ FTIR measurements, and was my first contact person when I needed advice or just somebody to talk to. Vojislav Stamenkovic introduced me into AES and LEISS, and was always there for me no matter if it was professional or personal. The same applies for Berislav Blizanac, who I also have to thank for all the discussions during cigarette breaks and of course the editing of the graphics in this work. In addition I would like to acknowledge Simon Mun's XPS work at the Advanced Light Source, and Vera Zhuang as well as Phil Ross for being there with their advice. Last but definitely not least I

Table of Contents

List of Abbreviations

Common abbreviations:

AES	Auger Electron Spectroscopy
CE	Counter Electrode
CO_b	CO bulk oxidation
cs-	carbon supported
CV	Cyclovoltammogram
DFT	Density Function Theory
DOS	Density of States
EDX	Energy dispersive X-ray spectroscopy
fcc	face centered cubic
FTIR	Fourier-Transform Infrared Spectroscopy
GC	Glassy Carbon
HER	Hydrogen Evolution Reaction
HRTEM	high resolution Transmission Electron Microscopy
HSAC	high surface-area catalyst
Hupd	under potentially deposited Hydrogen
IRAS	Infrared Absorption Spectroscopy
IRRAS	Infrared Reflection Absorption Spectroscopy
LBNL	Lawrence Berkeley National Lab
LEED	Low-Energy Electron Diffraction
LEISS	Low-Energy Ion Scattering Spectroscopy
NHE	Normal Hydrogen Electrode
OH_{ad}	oxygenated species
ORR	Oxygen Reduction Reaction
Pt(hkl)	Platinum Single crystals
Pt-poly	polycrystalline Platinum
pzfc	potential of free zero charge
pztc	potential of total zero charge
RDE	Rotating Disc Electrode

RRDE	Rotating Ring Disc Electrode
RE	Reference Electrode
SCE	Standard Calomel Electrode
SHE	Standard Hydrogen Electrode
STM	Scanning Tunneling Microscope
SXS	Surface X-ray Scattering
TEM	Transmission Electron Microscopy
TM	Transition Metal
UHV	Ultra High Vacuum
UPS	Ultraviolet Photoelectron Spectroscopy
WE	Working Electrode
XPS	X-ray Photoelectron Spectroscopy

Formula abbreviations:

A_{geo}	geometric area of the electrode
A^*_{geo}	corrected geometric area of the electrode
A_{real}	real surface area of the catalyst
B	Levich constant
c_{O2}	concentration of O_2
c_0	concentration in the bulk of the electrolyte
c_s	concentration at the surface
d	particle diameter
D	diffusion coefficient
D_s	surface dipole
E	potential of the electrode
E_1, E_2	energy of the states
ΔE	difference between energy of the states
E_a	activation energy
E_f	final kinetic energy of the scattered ions
E_i	initial kinetic energy of the scattered ions
$\bar{E}^i$	electric field vector of the incident beam

v	sweep rate
v_M	molar volume
z	number of transferred electrons

Greek letters:

α, β	angle of incident and refraction in FTIR
β	transfer coefficient, symmetry factor
γ	transfer coefficient, symmetry factor
δ_{RDE}	thickness of the diffusion layer
η	overpotential
η_{O2}	overpotential versus the reversible oxygen potential
Θ	scattering angle in LEISS
Θ_{ad}	total surface coverage
Θ_{anions}	surface coverage with anions
Θ_{OH}	surface coverage with oxygenated species
μ	dipole moment
μ_c	chemical potential
μ_p	d-band center
ν	kinematic viscosity
ν_0	absorption frequency (FTIR)
ν_{CO}	absorption frequency of CO
Φ	workfunction
Ψ_1, Ψ_2	quantum states of energy
ω	rotation rate
ω_{tp}	transition probability

1. Introduction

The fields of electrochemistry and heterogeneous catalysis exist as long as chemistry itself. Berzelius'[2] introduction of the term catalyst, as a substance that enhances the rate of a chemical reaction without being consumed nor generated during the process, dates back to as early as 1835. In analogy to catalysis, electrocatalysis, i.e. the combination of these two areas of physical chemistry, commonly describes the study of electrode processes involving charge transfer reactions and materials that accelerate these reactions. Although also the era of electrocatalysis had its dawn already in the 1930s[3], it has been approximately the last thirty years that this field started to flourish[4,5]. The basic theories on thermodynamics and kinetics have been established early, but the connection with the activity of catalysts was not always straightforward. The development of UHV-technology and the introduction of model catalysts in the late 60s marked the beginning of the "Surface Science Approach" to traditional catalysis. Single crystalline samples have been the model catalysts of choice from the beginning, due to their regular and simple surface structure compared to polycrystalline materials. By means of these well-defined extended surfaces of catalysts prepared and analyzed under UHV conditions, the reaction rate of a process could now be associated with the atomic and electronic structure of the solid-vacuum interface of the catalyst. Initially, the chemisorption properties and mechanism of some catalytic reactions have also been deduced from UHV experiments[6], which were consistent and satisfactory in this specific environment but not always applicable for processes under atmospheric pressure, not to mention solid-liquid interfaces. This *pressure gap* was soon afterwards the focus of investigations of surface science, with model systems characterized before and after the studied reaction in a coupled UHV chamber[7]. But especially for electrocatalysis, where the surface of the catalyst is most definitely modified during the observed reaction by either reaction intermediates or *spectator* species[8], the development of in-situ techniques was essential to improve the understanding of the microscopic processes at electrode surfaces. For instance in-situ Fourier Transform Infrared Spectroscopy (FTIR) and in-situ Raman Spectroscopy have become powerful tools for analyzing

various adsorbates during electrochemical reactions [9], and in-situ scanning tunneling microscopy (STM) permits the investigation of catalysis on electrode surfaces with atomic resolution [10,11]. Based on these methodologies with their resulting new or extended perceptions on model catalysts, recent research efforts have been aiming at the understanding of more complex and practical catalytic systems. Consequently the present focus for application purposes is filling the gap between well-established single crystal model systems and the characteristics of real catalysts that arises from the finite size and the presence of a support material.

Virtually every electrochemical reaction, in which chemical bonds are broken and formed, can be considered electrocatalytic, and the kinetic activity varies by order of magnitudes for different electrode materials. This was already figured for the probably most simple and intensively studied electrochemical reaction, the hydrogen evolution – oxidation reaction (HER/HOR). The first successful attempt to correlate electrode properties to the intrinsic rate of the reaction, defined by the exchange current density i_0, was demonstrated by Bockris and Conway, who found a linear relationship between $\log i_0$ and the workfunction Φ of the metal, and attributed this to the metal-hydrogen interaction energy [12]. Around the same time Parsons and Gerischer [13,14] independently derived from classical transition state theory the relation between $\log i_0$ and the Gibbs energy of adsorbed hydrogen (ΔG^0_{Had}). The general form of this relation possesses a *volcano* shape, with elements at the top that adsorb hydrogen not too strongly but still interact vividly with the molecules, following the Sabatier principle [15,16].

Much more complex than the HER/HOR and even more interesting is the oxygen reduction reaction (ORR). In contrary to the HER, the ORR is a multi-electron reaction that consists of number of elementary steps with various reaction intermediates. Plenty of reaction mechanisms have been proposed over the years [17], with the simplified version of the scheme given by Wroblowa [18] somehow to stand out:

$$k_1$$

$$O_2 \longrightarrow O_{2,ad} \underset{k_4}{\overset{k_2}{\rightleftarrows}} H_2O_{2,ad} \overset{k_3}{\longrightarrow} H_2O$$

$$\Big\updownarrow k_5$$

$$H_2O_2$$
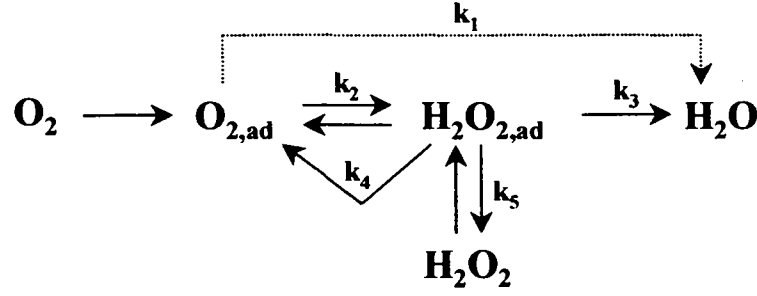
Figure 1.1: Reaction scheme for the oxygen reduction reaction proposed by Wroblowa

Briefly described, it states that adsorbed oxygen can react via a direct four-electron reduction step, and/or in a series pathway with two two-electron reduction steps and hydrogen peroxide as an adsorbed or dissolved intermediate. Depending on the nature of the electrode material, the electrolyte and the reaction conditions, the reduction can occur in the direct or series pathway, or in both simultaneously. For years researchers have been puzzled by the fact, that even with the most active electrocatalysts, namely the Platinum group metals, noticeable currents are obtained only below 1 Volt, far more negative than the equilibrium potential of 1.23 Volt versus a standard hydrogen electrode [19]. Therefore kinetic studies on ORR often use the current density at a fixed potential instead of the exchange current density as a measure of activity. Similar to HER, a volcano relationship was found for the reaction rate when plotted against the heat of adsorption of oxygen on different electrode materials [20]. Consequently even for some noble metals like Pt, the interaction with the reaction intermediates seems to be so strong that at practical current densities the ORR can only take place at a remarkably high overpotential. Considering these findings and assuming that the rate-determining step is the addition of the first electron, the basic expression for the reaction rate has been extended by terms including the total surface coverage Θ_{ad}, consisting of the coverage with anions Θ_{anions} and oxygenated species Θ_{OH} [21,22]:

$$i = nFKc_{O_2}(1 - \Theta_{ad})^x \exp\left(-\frac{\beta FE}{RT}\right)\exp\left(-\frac{\gamma r \Theta_{OH_{ad}}}{RT}\right) \tag{1.1}$$

This relationship was further confirmed by studies on Platinum single crystals (*Pt(hkl)*), where a significant structure sensitivity of the reaction rate depending on the type of electrolyte could be

found [23-25]. Thus it was proposed that not only the heat of adsorption of reaction intermediates, but also the surface coverage by spectator species or anions determines the sensitivity of the ORR to the geometry of the active sites, as shown extensively by Markovic et al. [8]. Although mainly investigated in model systems, this anion effect exerts certainly also a major impact on practical catalysis, where equation (1.1) necessarily remains valid. Very intriguing is the issue of peroxide production during the ORR, which can provide essential information on the actual reaction mechanism. Again, according to rotating ring disc measurements on single crystals, this reaction has been found to be strongly structure sensitive. On Platinum electrodes the peroxide production is in general negligible, but when surface sites that are necessary for the breaking of the oxygen-oxygen bond are blocked by for instance adsorbed hydrogen, chloride or bromide, peroxide can be detected quantitatively at the ring electrode [22,24]. Electrode materials like carbon or gold on the other hand, reduce oxygen in alkaline solution in a series pathway without significant amounts of peroxide as a side product, whereas in acid solution the reaction stops at peroxide without further reduction to water. Ross rationalized this in a way that the interaction between the dissolved oxygen and the electrode surface in acid electrolyte is extremely low, and consequently the O-O bond-breaking step becomes rate determining for the overall reaction [26]. For a complete review of electrochemistry on the relevant reactions on model catalysts, the interested reader should refer to reference [8].

Another reaction of high fundamental as well as practical interest is the electrooxidation of carbon monoxide. CO often serves as a model *fuel* in electrochemistry, for it is an intermediate in the oxidation of many organic molecules, such as methanol or formic acid. Moreover it is also of major interest for applied research, because of its occurrence in reformate gas and hydrogen used to run fuel cells, concomitant with its poisonous nature for Pt. On an emersed electrode it has been found that the CO saturation coverage is higher than observed in a gas phase [27]. The structure of the CO-adlayer on Pt(111) was determined to be p(2x2)-3CO in CO-saturated solution using in-situ surface X-ray scattering (SXS) [28] and in-situ STM [29], with one on-top and two hollow-site CO-molecules per p(2x2) unit cell resulting in a CO-coverage of approximately 0.75. This is the only single crystal for which a CO structure with long-range order has been found, but from CO-stripping data similar CO-coverages could be established for the other single crystals. In solutions without CO, the structure of the preadsorped CO-adlayer is dependent on the potential. At potentials close to 0.0 V_{RHE} the same p(2x2) symmetry was observed, whereas at higher potentials various different structures were reported [8]. By using additional information

from electrochemical oxidation of a CO monolayer it becomes clear, that partial oxidation of the CO_{ad} already starts as soon as at 0.3 V_{RHE} and consequently the surface structure begins to change [30,31]. Upon sweeping the potential of a Pt-electrode positive from 0.05 V_{RHE} in CO-saturated solution, first "weakly adsorbed" CO_{ad} is getting oxidized in the so-called pre-ignition or pre-oxidation potential region, and the remaining CO-molecules stabilize in a more "strongly adsorbed" adlayer [30,32]. At a more positive potential, the ignition potential, also these remaining CO-molecules become oxidized. The mechanism for the reaction has been proposed to be a Langmuir-Hinshelwood type, where CO_{ad} and the oxidizing agent OH_{ad} have to be co-adsorbed on adjacent sites at the same time.
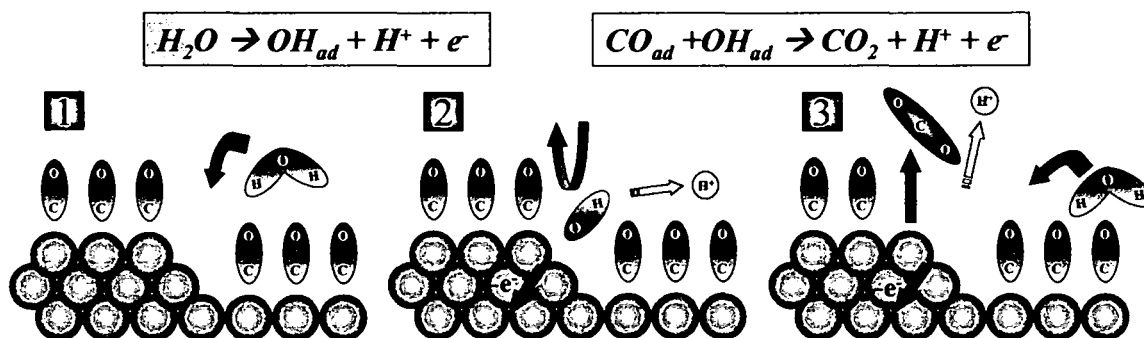
Figure 1.2: Scheme of the oxidation of pre-adsorbed CO on a Pt surface by a Langmuir-Hinshelwood mechanism. Water is being adsorbed (1) and dissociated (2) at a free step site, where it can react with a adjacent CO_{ad} molecule (2) to CO_2, which desorbs into the electrolyte (3). Thereafter the sequence starts over again with more sites available for OH_{ad} adsorption from water.

The strange behavior of the oxidation when the CO partial pressure is reduced, i.e. positive reaction order in the pre-oxidation region and negative one at the ignition potential, was assigned to non-competitive adsorption and competitive adsorption, respectively, of CO_{ad} and OH_{ad} [8]. Studies of Pt-electrodes with different facets show varying results for CO-electrooxidation in both pre-ignition and ignition region, with a tendency that the onset potential increases the less stepped a surface is [33,34]. As seen by this structure sensitivity, steps and defect sites play an important role as active centers for the reaction (Figure 1.2). Additionally the role of the anions of the supporting electrolyte must not be underestimated. They can drastically inhibit the oxidation of adsorbed CO by blocking sites for OH_{ad} adsorption, i.e. preferentially those crucial step sites. It is therefore not surprising that in alkaline solution, where only OH⁻ anions and no *spectator* anions can be found,

the catalytic activity is superior [35]. This short overview reflects only a small part of the complexity of this irreversible reaction, which is described in more detail in reference [8].

In the previous paragraph the current knowledge of major electrochemical reactions based on data from single crystal and polycrystalline model systems has been demonstrated. Now the next question arises, whether this is also applicable to practical catalysts and which additional properties have to be considered to understand the whole picture. In general there are two important characteristics of real systems that cannot be accounted for by model systems. Firstly, real catalysts are usually mechanically supported to achieve a high degree of dispersion, i.e. the ratio of surface catalyst atoms to the total number of catalyst atoms. These supports are inexpensive and highly porous materials with high surface areas themselves, often used are various high surface area carbons (Vulcan, Shawinigan Black...), metal oxides (Al_2O_3, TiO_2) or metals that are cheaper than the actual active catalyst (e.g. noble metals) in some cases. Although mostly considered as inert phases, they can sometimes substantially interfere with the catalytic activity and selectivity. For instance can strong metal-adsorbate interaction lead to alloying with or migration of the support material onto the catalyst particles, or the support can alter the electronic properties of the active component and therefore change its adsorption and catalytic properties [36,37]. The metal-support interaction of carbon supported Pt particles, which are applied in this work, is primarily of interest for the preparation and dispersion of the catalyst, and has no influence on the catalytic activity [38]. But a second effect occurs in real systems, which has been shown in numerous efforts on various systems, viz. both the reactivity and the selectivity of a catalyst can depend on the particle size. Since it is impossible to cover the whole work dealing with this phenomenon, the focus will be the improvements in this regard for two very important but also controversial electrochemical reactions.

With the advancement in phosphoric acid fuel cell technology in the seventies, research on carbon supported Platinum catalysts became much livelier. Bregoli was one of the first to indicate that by decreasing the particle size of Pt to increase the active surface area, also concomitantly the specific activity for oxygen reduction, i.e. the activity per surface site, is decreasing [39]. Ross found a similar but more pronounced behavior on Pt-particles with higher surface area [40]. This influence of the platinum crystallite size on the electrocatalytic reduction of oxygen molecules is therefore further labeled simply as the *particle size effect*. Initially the particle size effect was attributed to the

changes in the morphology of the crystallites, because the relative amount of surface atoms in different crystal facets changes with size. Therefore smaller particles should behave like a (110)-single crystal, since they feature more edge and corner sites, and larger particles should exhibit similarities to (111) and (100) because of their more extended surfaces. Also Kinoshita could observe a clear correlation between the varying single crystalline fractions of surface atoms and the specific activity [41]. Furthermore the mass activity reached a maximum at a Pt particle size of about 3nm, which correlates closely to the maximum in mass-averaged distribution of (111) and (110) surface atoms on Pt particles with cubo-octahedral shape. The implications concluded from the kinetics of the oxygen reduction on Pt(hkl) electrodes in different electrolytes by Markovic et al. [42] supported the model of Kinoshita as well. Watanabe, however, proposed a completely different explanation for this effect [43]. In his *territory theory* he claims that a mutual influence on the diffusion, "or some other parameters", exist when Pt-particles are close together, so that not all of the Pt surface area is usable for the reaction. The particle size effect is thereafter not truly dependent on the crystallite size, but rather on the inter-particle distances, with a critical distance of 20nm above which the specific activity was constant. But this hypothesis was disproved in an extensive effort by Giordano et al. [44], who could not find conclusive evidence for the significance of the inter-particle distance on the electrocatalytic activity. Interesting to notice is also, from the measurement of the zero point of charge of the Pt/C they concluded, that the interaction between the electrocatalyst and the carbon support is negligible, and does not influence the oxygen reduction. More recently Takasu et al. [45] have attributed the particle size effect to stronger binding of reactants, in particular molecular oxygen, to the catalyst surface. This was derived from XPS-measurements of the core-level binding energy of electrochemically aged Pt particles on a glassy carbon electrode, which however can be rather ascribed to a final state effect of the spectroscopy technique [46]. A similar conclusion was drawn from in-situ XAS studies by Mukerjee [47], viz. the adsorption of OH_{ad}, among other molecules, is stronger on smaller particles. These stronger adsorbed oxygenated species act as blocking species and can inhibit the oxygen reduction reaction to a certain extent [22].

In contrary to the oxygen reduction, the CO oxidation reaction was not studied on Pt particles until recently. Although of major practical importance for fuel cells, better catalysts for the CO oxidation than pure Pt were soon found in Pt-alloys whose bifunctional mechanism became the center of attention [48,49]. Only now with the increasing interest for nanostructured materials and their properties, more commitment to fundamental research on model supported-

catalysts has been undertaken. Pt-particles supported on gold were studied by Friedrich et al. [50;51], who displayed the shift of the vibrational frequencies to lower wavenumbers in in-situ FTIR with decreasing size. Their reasoning suggested that both lateral dipole field interaction between the adsorbed CO-molecules and the coordination of the Pt-adsorbate cannot be responsible for that, and explained the effect by particle-substrate interaction. For carbon supported Pt catalyst Wieckowski et al. [52] came to a similar conclusion, although Park et al. [53] emphasized the influence of size-dependent surface coordination of Pt atoms. Furthermore Friedrich realized that on smaller particles a CO-monolayer is oxidized at a higher overpotential than on a bulk polycrystalline Pt-crystal in a so-called CO-stripping experiment. This was accounted for by a change in reaction mechanism from the classically valid Langmuir-Hinshelwood to Eley-Rideal, inferred from time-dependent transient measurements. That this is very unlikely was shown recently by model calculations by Dunietz et al. [54] on electrooxidation of CO at full coverage conditions, where they concluded that a vacancy adjacent to an adsorbed CO is needed to facilitate the reaction at moderate applied potentials, otherwise the full layer completely inhibits the oxidation. Savinova et al. also found a decreased activity for CO-stripping for Pt-particles deposited on glassy carbon electrodes, and a tentative model of slow CO surface diffusion acted as a makeshift in their case [55;56], which is somehow in disagreement with results from single crystals. The reason why smaller particles, which are supposedly more oxophillic, are less active for CO-oxidation is therefore still considered unresolved.

One promising development towards improved catalytic activities seem to be alloys of Pt with transition metals like Ni, Co or Fe [57-60] for the ORR and other atoms like Ru [48;61] or Sn [49;62] for the CO-oxidation. While the benefits of the bifunctional mechanism in latter case are already well established, the effects for the ORR have only recently attracted more attention. Fundamental studies of extended Pt-alloy surfaces [59;60] have unambiguously demonstrated that a controlled arrangement of the two elements in the electrode surface region is in direct correlation to the kinetic activities of these materials. By applying certain preparation steps in combination with surface sensitive analytical techniques in UHV, it was possible to generate well-characterized alloy structures that are of high stability in electrochemical environment and up to three times more active than pure Pt. This was explained on the basis of a positive electronic impact of the transition metal onto the adsorption properties of the alloy, based so far only on theoretical considerations and model calculations. The rapid development of computational power and the

simultaneous improvements in electronic structure calculation algorithms over the last two decades have rendered first principle calculations relevant additional tools for experimental investigations in surface science and heterogeneous catalysis. Considering these recent theoretical efforts, especially the work of Hammer and Norskov on establishing chemisorption trends and characterization of reaction pathways should be pointed out [63;64]. They introduced a simplified theory of adsorbate bonding on transition metal surfaces, in which electronic states in the entire valence band of the metal surface are responsible for chemisorption, and not only the density of the states at the Fermi level nor the empty states above it. Under the assumption that interactions of adsorbates with metal sp-bands is only dependent on the nature of the adsorbate and therefore constant from metal to metal, changes in the hybridization energy between the bonding and anti-bonding adsorbate states and the metal d-bands determine trends in chemisorption. According to this theory, the shift in the characteristic center of the d-band for Pt-alloys versus pure Pt should be correlated to a *reduced* heat of adsorption of molecules like H_2, O_2 and CO [65;66], which has still to be approved.

2. Experimental

In this chapter the experimental techniques applied in the investigations of this work will be described. Emphasis is placed mostly on the in-situ methods, i.e. the Rotating (-Ring)-Disc-Electrode (RRDE) and Fourier-Transform Infrared-Spectroscopy (FTIR), but also a short overview of Auger Electron Spectroscopy (AES), X-ray Photoemission Spectroscopy (XPS), Low Energy Ion Scattering (LEISS) and Transmission Electron Microscopy (TEM) is given.

In addition some general comments regarding electrolyte preparation, cleaning procedures of electrochemical glassware and experimental conditions will be included, since a clean working manner is of outmost importance to obtain quality scientific results and is unfortunately far to often underestimated in electrochemistry. Details about preparation and transfer procedures to the electrochemical cell for single crystal electrodes as well as high surface area catalysts will be described later in the respective chapters.

2.1. Electrochemical measurements

2.1.1. Rotating Ring Disc Electrode (RRDE)

Plenty of electrochemical techniques have been applied in which the electrode moves relatively to the electrolyte solution. This methods involving convective mass transport of reactants and products have the advantages that the rate of mass transport to the electrode surface is typically larger than by diffusion only, so that the electron transfer kinetics are accessible in a wider potential region. Especially for reactions involving gases, which have generally a low solubility in the range of 10^{-4} to 10^{-5} mol/dm^3, methods with convective mass transport become a necessity. Furthermore a steady-state condition at the electrode surface is attained rather quickly, and measurements can be made with high precision. The most convenient and widely used system is the rotating disc electrode (RDE), because of its easy construction with a variety of electrode

materials [67;68]. Moreover adequate theoretical solutions have been found for the hydrodynamic problem of the RDE (e.g. determining solution flow velocity profiles as function of rotation rates, solution viscosities and densities) under steady-state conditions, which can rarely be achieved for different geometries [69].

Figure 2.1: Sketch of a rotating disc electrode with schematical streamlines (top and side view) in the electrolyte. The rotation axis is denoted 'z'
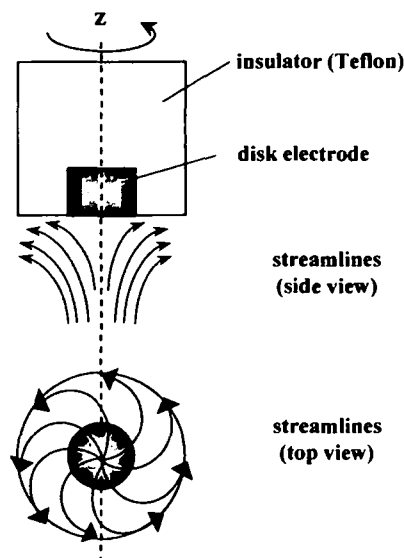
The RDE consists generally of a smooth circular electrode embedded in an insulator, with the electrode surface perpendicular to the rotation axes. In rotating mode, the electrolyte is being dragged towards the electrode surface where centrifugal forces fling the solution outward from the center in radial direction (Figure 2.1). Knowing the hydrodynamic profile, the mass transfer can be further investigated. Levich first introduced a theoretical treatise [70] in which it is assumed that the mass transfer of the electrolyte up to a certain distance from the electrode surface is convective and diffusion takes place afterwards. The thickness of the diffusion layer δ_{RDE} is given by:

$$\delta_{RDE} = 1.61 D^{\frac{1}{3}} v^{\frac{1}{6}} \omega^{-\frac{1}{2}}$$
(2.1)

where D, v and ω denote the diffusion coefficient of the reactant in the electrolyte, kinematic viscosity of the electrolyte and the angular velocity or rotation rate of the electrode, respectively. According to (2.1), the thickness of the diffusion layer depends only on the rotation rate and is

independent from the disc radius, in contrast to an electrode in quiescent electrolyte where the thickness of the diffusion layer increases with time until natural convection becomes determining. Not only is therefore the diffusion layer thickness roughly one to two orders of magnitudes lower ($\approx 20\mu m$ instead of $\approx 500\mu m$ [68]) and a steady state is reached faster, but also it becomes externally controllable. Using Fick's law, the current density measured at the disc electrode can be expressed in terms of the concentration of reactants in the bulk of the electrolyte c_0 and at the electrode surface c_s,

$$j = nF\frac{D}{\delta}(c_0 - c_s) \qquad (2.2)$$

with n and F being the number of transferred electrons per reaction and the Faraday constant, respectively. In the case if reaction rate at the electrode is significantly faster than diffusion processes, i.e. every reactant immediately reacts and c_s becomes virtually zero, the current density becomes diffusion limited and (2.2) can be rewritten to:

$$j_D = nF\frac{D}{\delta}c_0 \qquad (2.3)$$

Substituting the expression for the RDE diffusion layer thickness (2.1) into (2.3), the *Levich-Equation* for the diffusion limited current density on a RDE can be obtained:

$$j_{D,RDE} = 0.620nFc_0 D^{\frac{2}{3}}v^{-\frac{1}{6}}\omega^{\frac{1}{2}} = Bc_0\omega^{\frac{1}{2}} \qquad (2.4)$$

Consequently the diffusion-limited current is time-independent and is only determined by the rotation rate of the electrode. Note, that the definition of the Levich-constant B in literature is not consistent, however, here it is defined including the bulk reactant concentration c_0.

An extension to the above-described RDE is the rotating ring disc electrode (RRDE), where in addition to the disc electrode a concentric ring with inner and outer radius r_2 and r_3, respectively, form an electrode. The disc and the ring are separated from each other by an insulating gap, usually made of Teflon.

isolator (Teflon)

ring

disk

Figure 2.2: Schematic diagram of a rotating ring
disc electrode with ring, disc and insulating gap
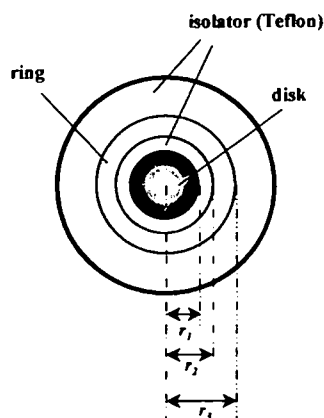
First described and theoretically treated by Frumkin [71], the RRDE enables one to study adsorption processes and multi-step electrode reactions. Analogous to the RDE the diffusion limiting current density of the ring electrode is given by:

$$j_{D,ring} = \kappa^{2/3} B \omega^{1/2} \qquad (\text{with } \kappa = r_3^3 / r_1^3 - r_2^3 / r_1^3) \qquad (2.5)$$

In collection mode, the species that are generated on the disc electrode are collected on the ring electrode where they react further. The potential of the ring electrode can be adjusted independently, and has to be set at a value where the reaction is limited by diffusion only. Depending on the geometries of the assembly, only a fraction of the species that are generated at the disc can be recovered at the ring, which is defined by the collection efficiency N:

$$N = {-I_{ring}} \Big/ I_{disc} \qquad (2.6)$$

Experimentally the collection efficiency is evaluated by a standard method using potassium ferrocyanide/ferricyanide, for the electrode configuration in this work N was determined to be 0.21 ± 0.02. A more detailed description of the RRDE method can be found in the following references [67-71].

2.1.2. Cyclic Voltammetry (CV)

This potential scan method has become the most popular technique in electrochemistry, not only for initial studies of new systems but also for obtaining information about fairly complicated electrode reactions. As a specific case of linear potential sweep chronoamperometry or linear sweep voltammetry, the potential is usually varied linearly with time while the current is recorded as a function of the potential, which is obviously equivalent to recording against time. In cyclic voltammetry (CV) the potential is scanned with a constant sweep rate (usually in the order of mV/sec to 100V/sec) in a certain potential range and once the potential limit is reached, the direction of the scan is reversed. Thus obtained current-voltage relationship can be depicted in a so-called voltammogram. Due to the correlation between the potential scale of a CV and the energy scale, this method is a very powerful tool for revealing the nature and the energetic properties of processes at the electrode surface, especially for adsorption processes. For the more interested reader, references [5;67;72;73] can provide further insight into this topic.

2.1.3. The Electrochemical cell

All electrochemical measurements were carried out in a thermostatable three-compartment electrochemical cell equipped with a water jacket (Figure 2.3). Although very conductive aqueous solutions are used as electrolytes, the application of the Rotating (Ring) Disc Electrode for kinetic studies makes a three-electrode configuration absolutely necessary to avoid any measurement errors due to resistances in electrolyte.

Legend

1. Water Jacket
2. Water from Thermostat
3. Water to Thermostat
4. Teflon Cap
5. Counter Electrode (Pt)
6. Gas Bubbler
7. Glass Frit
8. Working Electrode
9. Luggin Capillary
10. Gas Line (to gas bubbler)
11. Electrode Shaft (to rotator)
12. (Closed) Electrolytic Bridge
13. Reference Electrode (SCE)
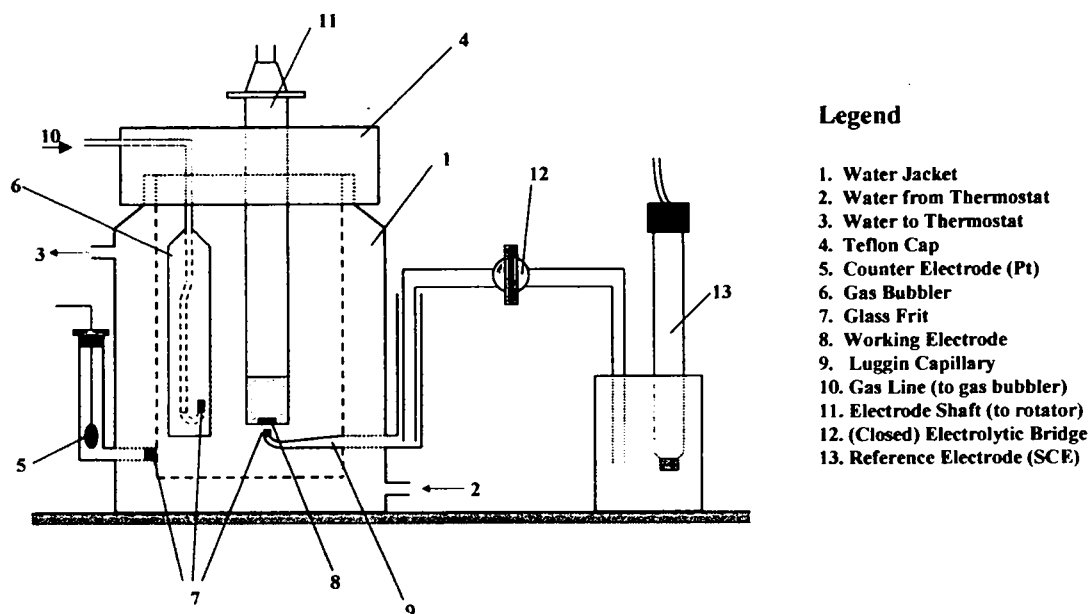
Figure 2.3: Sketch of a three-compartment electrochemical cell

In this special setup, a variable current source passes a current through the working and the counter electrode (CE). Resulting changes in the potential of the working electrode (WE) are monitored relative to a reference electrode (RE). The device used to measure this potential difference has a high input impedance, so that ideally no current is drawn through the reference electrode. Consequently, its potential will remain constant at all times and equal to its open circuit value, and the measured potential change between WE and RE is determined by the change in potential at the WE only. Since the reference electrode has to be placed somewhere between the WE and CE, a certain potential drop between them will still be included in the measured potential. In order to minimize this uncompensated resistance, the RE has to be positioned as close as possible to the WE (without interfering with mass flow patterns in the cell), which is facilitated with a fine tip called Luggin capillary [67;72]. The counter electrode should be stable under the experimental conditions and the formation of side products that would cause interfering reactions at the working electrode should be avoided. Therefore a Pt-mesh with high surface area served as a CE in above shown configuration, cleaned by flame annealing before every measurements and placed in a compartment separated from the main cell by a glass frit. A Standard Calomel Electrode (SCE) was used as the reference electrode in all measurements, however, in the following chapters the potential is always referred to the Reversible Hydrogen

Electrode (RHE) in the same solution, which was calibrated at the beginning of each experiment by oxidation/reduction of H_2 (see Figure 2.4).
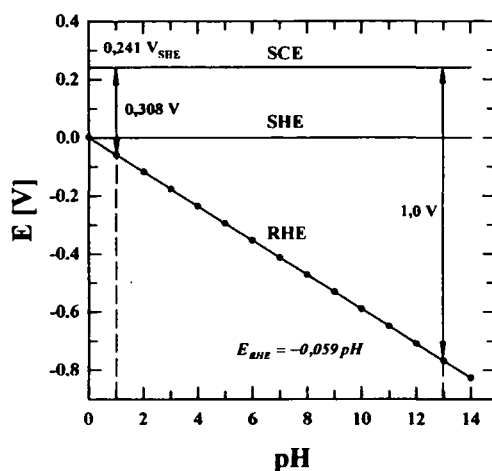
Figure 2.4: Potential relation between the experimentally applied Standard Calomel electrode (SCE), the Standard Hydrogen Electrode (SHE) and the Reversible Hydrogen Electrode (RHE) at standard temperature. All potential values in the text are referred to the RHE.

The RE was always kept at constant temperature and was connected to the Luggin-capillary over a closed electrolyte bridge, preventing possible chloride contamination of the electrolyte from the SCE. The working electrode was pressed tightly into a U-cap out of Teflon, in a way that the sides of the electrodes were protected from leaking and only the surface would be in contact with the electrolyte. Moreover this setup was mounted in an insertable disc (-ring) electrode assembly (*Pine Instruments*), which was linked to the rotator by a shaft. A circulating constant temperature bath (*Fisher Scientific*) maintained the temperature of the electrolyte within ± 0.5K. All parts of the cell were stored in distilled water when not used, and before measurements always boiled twice in distilled water and carefully rinsed with triply-pyrolitically distilled water. Also the electrolytes of research quality, $HClO_4$ (*Merck*), H_2SO_4 (*J.T. Baker*) and KOH (*J.T. Baker*), were diluted to desired concentration with this triply-pyrolitically distilled water to avoid traces of organic or ionic impurities. For saturation of the electrolyte research grade Hydrogen, Argon, Carbon Monoxide or compressed Oxygen (all *Airgas*) were introduced through the gas line.

2.2. Fourier transform Infrared Spectroscopy (FTIR)

Infrared Absorption Spectroscopy (IRAS) has proven to be a powerful method not only for analyzing bulk absorption properties of liquids, but also for investigating adsorbed molecules at solid-gas as well as solid-liquid interfaces. Latter will be of the main interest in this work, but first the fundamentals of IRAS, i.e. the interaction of light with molecules, shall be briefly reviewed.

2.2.1. Principles of Infrared Spectroscopy

Light absorption by a molecule generally occurs when a photon of the energy $h\nu_0$ hits a molecule in the initial state of energy E_1 and excites it to a higher state of energy E_2, thereby satisfying the Planck relation [74]:

$$h\nu_0 = \Delta E = E_2 - E_1 \qquad (2.7)$$

When using a quantum mechanical approach, the transition probability for this process can be calculated by solving the time-dependent Schrödinger equation utilizing the time-dependent perturbation method. Without going into details, this would lead to the calculation of a matrix element, which is directly proportional to the transition probability ω:

$$\omega_{tp} \propto \langle \Psi_1 | \vec{\mu}\vec{E} | \Psi_2 \rangle \qquad (2.8)$$

where Ψ_1 and Ψ_2 are wave functions of state 1 and 2, respectively, μ is the vector of the dipole moment and E is the electric field vector. Only transitions between states for which the transition probability ω and the dipole moment μ are non-zero are allowed, i.e. only molecules with an electric dipole moment of non-zero and also a matrix element (2.8) different of zero are IR active [74]. The matrix element is non-zero for discrete changes in vibrational quantum numbers. All this leads to what are known as the selection rules for Infrared Spectroscopy, where the IR-beam is directed through a homogeneous sample (gas or liquid phase).

In contrast to conventional IR-spectroscopy, in Infrared Reflection Absorption Spectroscopy (IRRAS) the IR-beam is directed onto a solid surface at a certain angle α and the change in intensity due to absorption of the adsorbed molecules are detected in the reflected beam.

$$\vec{E} = \vec{E}_p + \vec{E}_s$$

$$\vec{E}_p \perp \vec{E}_s$$
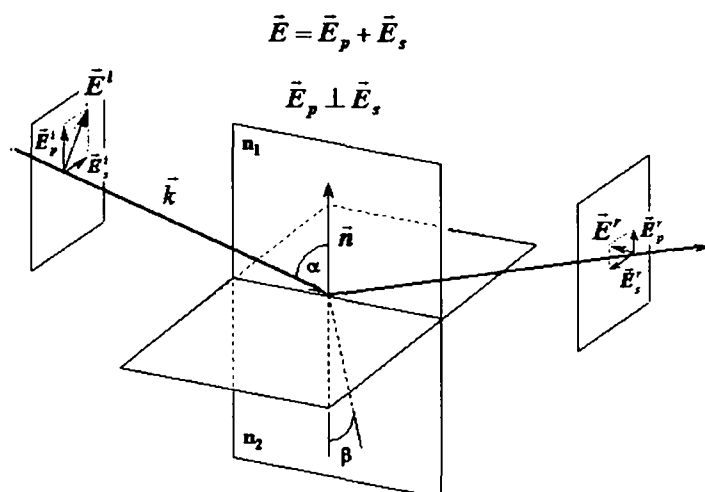
Figure 2.5: Reflection of an electromagnetic wave at the boundary between two homogenous media of different refractive indices n_1 and n_2

Consequently to completely capture the nature of IRRAS it becomes necessary to expand conventional IR-theory by outlining the basics of reflexion of light. When light is reflected at the boundary of two homogeneous, isotropic phases, viz. the surface, both the intensity and the state of polarization are affected [74]. Figure 2.5 illustrates the relation between the electric field vector of the incident beam E^i and the reflected beam E^r. Formally, at the phase boundary of the two phases both the incident and the reflected electric field vector are simultaneously present. The direction of propagation parallel to the wave vector k and the unit vector n perpendicular to the plane of reflection define the plane of incidence. In order to simplify the mathematical description of the reflection, it is useful to separate the electric field vector of the electromagnetic wave into two perpendicular parts, E_p and E_s respectively. The former vector lies in the plane of incidence (p-polarization) whereas the latter vector is perpendicular to the plane of incidence (s-polarization). Now, having the electromagnetic field vector in this form, the change of the amplitude and the phase of these two vectors upon reflection can be described by Fresnel's law (2.9):

$$E_p^r = -E_p^i \frac{\tan(\alpha - \beta)}{\tan(\alpha + \beta)} \quad \text{and} \quad E_s^r = -E_s^i \frac{\sin(\alpha - \beta)}{\sin(\alpha + \beta)} \quad (2.9)$$

The angle of incidence α and the angle of refraction β are dependent on the refractive indices n_i of the two phases and can be calculated using Snell's law (2.10):

$$n_1 \sin \alpha = n_2 \sin \beta \quad (2.10)$$

Since for the reflexion on metal electrodes the case of $\alpha + \beta > \pi/2$ and $n_1 < n_2$ is always fulfilled, the phase angles of the p-polarized and s-polarized light are changed, more precisely the change in the phase angles of E_p and E_s are 0 and π respectively. This means consequently that the incident and reflected waves tend to cancel out for s-polarization, whereas for p-polarization both waves add in phase. Therefore the interaction between the IR-beam and the adsorbed molecules will only be important for those molecules who have an electric dipole moment perpendicular to the surface in the adsorbed state. This restriction constitutes the so-called surface selection rule [74].

2.2.2. In-situ FTIR-setup and experimental details

As already mentioned, in IRRAS an IR-beam is directed onto a surface and the remaining intensity in the reflected beam is acquired, yielding the so-called sample spectrum. A second spectrum is recorded, i.e. the background (or reference) spectrum, at a moment when no adsorbed species interfere with the IR-beam. The spectrum showing the frequencies absorbed by the adsorbed molecules is obtained by subtracting the background from the sample spectrum. The Fourier Transform (FT) enables one to use an incident beam of a wide frequency range and to gain the final frequency-intensity relationship by a mathematical backtransformation. As a consequence the recording time of one spectrum is drastically reduced and therefore signal to noise ratio can be improved by adding up several spectra. To simplify, in the following chapters in-situ Fourier Transform Infrared Reflection Adsorption Spectroscopy will be referred to as FTIR, since this is the only way it was applied in this work.

The most obvious obstacle applying FTIR in solution or at a solid/liquid interface, respectively, is the strong absorption of the IR-beam by the solvent, i.e. in general water. This

difficulty has only recently been overcome with the introduction of the thin layer configuration [9]. Using this configuration, the pathway of the IR-beam through the electrolyte is minimized by pressing the electrode surface on an IR transmitting prism, most commonly a CaF_2 prism (Figure 2.6). One major drawback is, however, that the diffusion of the electrolyte into- or out of the thin layer is significantly obstructed. In this setup the thin layer behaves approximately like a closed system. Unfortunately this limits in some cases the ability to investigate surface reactions, e.g. if irreversible adsorption occurs. Furthermore it is important to note that the thickness of the thin layer cannot be calibrated in such a defined way that would meet the demands of controlling the IR-intensity. For that reason the sample and background spectra from which the ratio is calculated must be recorded in one set of measurement with identical thin layer. No lifting of the electrode or other geometric adjustments when acquiring a set of spectra is allowed. In case of the presented experiments, where the potential dependent absorption of molecules will be analyzed, the background spectrum will therefore be recorded either at a potential at which the very molecule hasn't yet adsorbed or one at which it already desorbed.
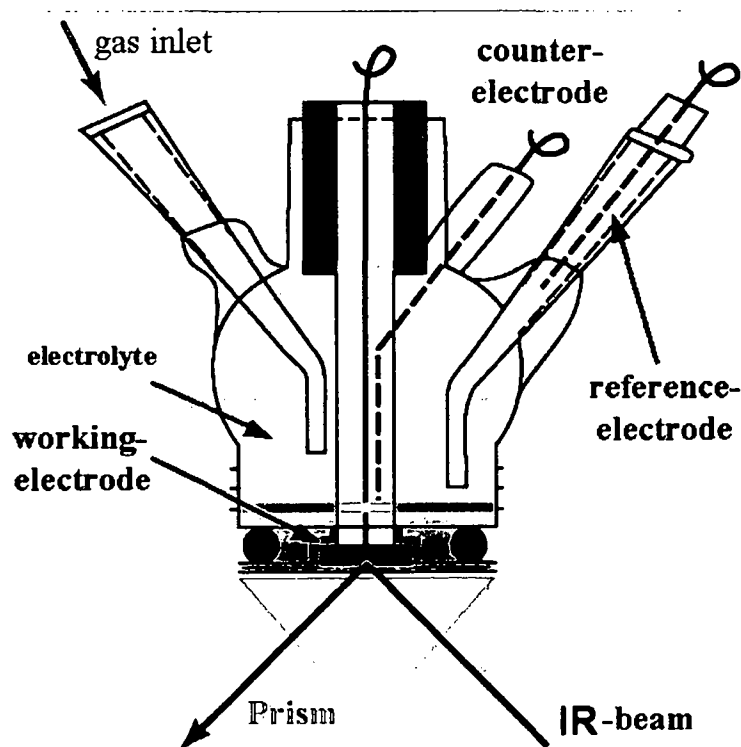
Figure 2.6: Sketch of the thin layer configuration in an in-situ FTIR cell

In FTIR spectroscopy at solid/liquid interfaces under potential control, two main factors determine the absorption frequency of the adsorbed species. The first one is based on the metal-adsorbate interaction and can be classified as a "chemical" effect. Since this interaction is dependent on the electrical field, the absorption frequency is also dependent on the applied electrode potential as evidenced by the electrochemical Stark-tuning shift [75;76]. Secondly, also the dipole-dipole field interactions between the vibrating adsorbed molecules need to be considered. This lateral "dipole" effect is strongly subject to the nature of the adsorbate itself and the surface coverage. Both effects are simultaneously influencing the absorption frequencies and their individual contribution cannot be unambiguously determined. For further detailed reviews on FTIR and its application in electrochemistry, the interested reader should study references [74;77;78].

For the in-situ FTIR experiments a Nicolet Nexus 670 spectrometer with a liquid nitrogen cooled MCT (Mercury Cadmium Telluride) detector was available. All IR measurements were performed in a spectroelectrochemical glass cell designed for an external reflection mode in a thin layer configuration (see Figure 2.6). The cell is coupled at its bottom with a CaF_2 prism beveled at 60° from the surface normal. Spectra were recorded with a resolution of $4cm^{-1}$ using p-polarized light. Absorbance spectra were calculated as the ratio $-\log(R/R_0)$, where R and R_0 are the reflectance values corresponding to the sample and the reference spectrum respectively. The reference potential in the spectroelectrochemical cell was controlled by a Standard Calomel Microelectrode (SCE), separated by a glass frit from the main electrolyte compartment to avoid leaking of impurities. All potentials, however, are given with respect to the Reversible Hydrogen Electrode (RHE), calibrated from the hydrogen evolution/oxidation reaction in a separated cell using the same electrolyte. Prior to each individual measurement cyclic voltammograms were recorded in order to check the cleanliness of the electrode surface and electrolyte. All FTIR measurements were performed without thermostat at room temperature ($T \approx 295K$).

2.3. Transmission Electron Microscopy (TEM)

Electron Microscopy is an imaging technique, mainly used in catalysis to determine size, shape and arrangement of particles. Valuable information on the degree of order and atomic-size defects can be obtained in a nanometer range.

A transmission electron microscope (TEM) is patterned very similar to an ordinary optical microscope, except that a beam of electrons and electromagnetic lenses are replacing light and optical lenses. An electron source forms a stream of electrons of 100-400 keV, which is directed towards the specimen by applying a positive potential. While passing through a condenser system, the stream is focused and confined by metal apertures and magnetic lenses into a thin, focused and monochromatic beam. This beam then hits the surface where it is transmitted, diffracted, backscattered or induces the emission of photoelectrons, x-ray fluorescence or Auger electrons. The transmitted electrons form a two-dimensional projection of the sample, depending on the density and thickness, which is magnified by electron optics and depicted by a so-called bright field image. When analyzing the diffracted beams, the resulting dark field images contain additional crystallographic information about the specimen. Furthermore the detection of the induced x-rays can provide knowledge about the composition of a fraction of the sample; this technique is called energy dispersive X-ray spectroscopy (EDX).

The high-resolution transmission electron micrographs of the investigated carbon supported catalysts in this work were primarily used to gain some insight into this nanostructures, but also to determine particle size distributions of the catalysts. More on HRTEM and TEM can be found in references [79,80]

2.4. Auger Electron Spectroscopy (AES)

Electron-excited Auger electron spectroscopy (AES) is probably the most widely used of all surface analytical techniques. Because of its easy implementation and its significance in qualitative surface analysis, it has become the accepted standard for establishing surface cleanliness.

In principle, a primary electron of an energy greater than the binding energy of an electron in a core level of the atom can excite that electron into an unoccupied state above the Fermi level. As the atom, in a series of transitions, relaxes back to the ground state, an electron from a higher level will fill up the core vacancy left behind. During these decay transitions the energy is

conserved by the emission of x-ray photons or Auger electrons (Figure 2.7). Since core level electrons for solids don't participate in bindings (remain localized), the kinetic energy of the emitted Auger electrons is characteristic for each element and therefore the surface composition can be obtained qualitatively by AES [81].

Auger electrons that are emitted from atoms close to the surface reach the detector with a much higher probability than those from the bulk [82]. Latter are rather lost due to inelastic scattering, which depends on the inelastic mean free path length of electrons and differs with the initial kinetic energy of the electron and the nature of the solid. Therefore AES is generally considered as a surface sensitive technique, although not completely surface specific as for example LEISS. Although primarily AES serves as a monitor of the cleanliness of the sample surface, it can also provide semi-quantitative information of the surface in some cases. Especially when working with samples of known surface structure and using additional surface specific methods. Details about AES can be found in references [81,83].
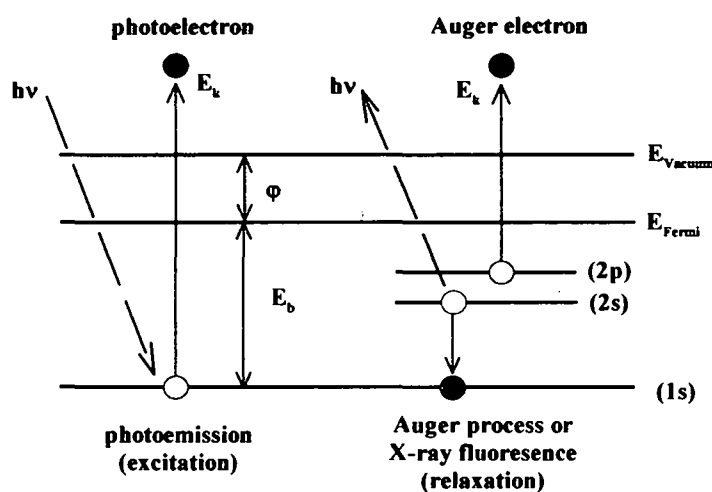
Figure 2.7: Principle of the photoemission process, Auger process and X-ray fluorescence

AES measurements were performed in an UHV system under a base pressure of about 2×10^{-10} Torr, equipped with an angular resolving double pass cylindrical mirror analyzer (PHI-DPCMA Φ15-255GAR) with an electron at its center axis. The spectra were recorded in derivative mode in the range of 80 – 880eV using a 3 keV electron beam energy, 3 $eV_{p\text{-}p}$ modulation and -5μA beam current.

2.5. Photoelectron Spectroscopy

Photoelectron spectroscopy utilizes photo-ionization and energy dispersive analysis of the emitted photoelectrons to study the composition and electronic state of the surface region of a sample. According to the energy of the excitation radiation it has basically been divided into X-ray and Ultraviolet photoelectron spectroscopy, XPS and UPS respectively.

XPS, with an excitation energy of 200 to 2000 eV, has been mainly used to determine the chemical composition of sample surfaces. Based on the photoelectric effect (Figure 2.7), an atom of the specimen absorbs an X-ray photon of energy $h\nu$, which leads to the emission of a core electron with an element characteristic binding energy E_b. Knowing the work function Φ of the material, the binding energy can be calculated from the kinetic energy of the emitted photoelectron [84]:

$$E_k = h\nu - E_b - \Phi \tag{2.11}$$

In UPS an incident radiation of 10 to 80 eV, in this case coming from the synchrotron at the Advanced Light Source at LBNL, is only capable of ionizing electrons from the valence levels in atoms. The binding energy of valence electrons carries more chemical information about the oxidation state and binding to neighbor atoms than element specific information compared to XPS. Consequently this method cannot be used to determine the elemental composition of the surface, but instead permits the complete mapping of the electronic band structure [84,85].

2.6. Low Energy Ion Scattering Spectroscopy (LEISS)

The most reliable surface sensitive method for determining the composition of a bimetallic surface is low energy ion scattering spectroscopy or short LEISS [86]. A beam of noble gas ions, usually Helium or Neon, with an energy of 0.1 to 10 keV is directed towards the surface of the investigated crystal at a certain angle, and the kinetic energy of the backscattered ions is detected (see Figure 2.8).
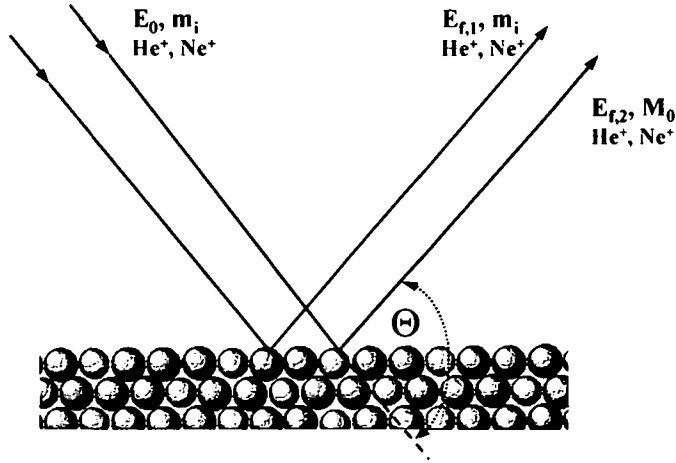
Figure 2.8: The principle of LEISS. The incoming ions are deflected from the surface with a different kinetic energy, depending on the mass of the atom it hits.

Since the kinetic energy depends on the mass of the target atom on the surface, an analysis of the recorded spectra allows the determination of the surface composition of the sample. The inherent surface sensitivity of this method can be attributed to the large neutralization probability of the incident ions by the metal. For example, for an 1 keV He^+ ion beam about 99% are neutralized when passing through one layer of substrate atoms [84]. Consequently the vast majority of ions that reach the detector are the ones scattered from the top surface layer. The fundamentals of the scattering of the inert gas ions can be described using a classical theory, since the de Broglie wavelength of the caroming ions is short compared to the interatomic distance of the crystal. An expression can be derived in which the ratio of the final and initial kinetic energy of the elastically scattered ions, E_f and E_i respectively, depends, besides the scattering angle θ, only on the masses of the incident ion m_i and the target atom m_t (2.12).

$$\frac{E_f}{E_i} = \left(\frac{\cos\theta + \sqrt{(m_t/m_i)^2 - \sin^2\theta}}{1 + (m_t/m_i)} \right)^2 \qquad (2.12)$$

LEISS was applied in this work solely to determine the surface composition of Pt-alloys with metals of the fourth period, i.e. Ti, V, Cr, Fe, Co and Ni. Since their mass is so much lower than that of Pt, the ratios of E_f/E_i are for instance 0.79 for Ni and 0.94 for Pt, and the peaks in the spectra can thus be easily resolved. The principles and applications of LEISS are described with more detail by Niehus et al. [87,88].

3. Model Systems - polycrystalline-Pt and Pt(hkl)

With the rapid progress of UHV technologies in the 1960's, and the concomitant development of novel surface analytical tools such as Auger Electron Spectroscopy (AES), X-ray Photoelectron Spectroscopy (XPS) or Low-energy Ion Scattering (LEISS), traditional aspects of chemistry could also gain some new incentives. The frontiers in heterogeneous gas-phase catalysis and later also in electrocatalysis advanced by the visions introduced by the "surface science approach", in which macroscopic kinetic properties of materials are linked to the surface structure and energetics on the atomic scale. For that matter well-characterized metal single crystals and polycrystals have been playing a major role as model systems for understanding the behavior of real, commercial catalysts. The low-index lattice planes of single crystals, the so-called low-index facets, of the pure metals provide an insight into the structure sensitivity of various reactions, whereas the higher index or stepped surfaces can reveal whether low coordination sites on a surface are specifically active. Also polycrystalline samples are still necessary model systems, especially for comparing results from the ideal systems with the real practical catalysts. In general, the purpose of studying a model catalyst is to understand a complex catalytic phenomenon that cannot be rationalized otherwise, in contrast to the intention of exploring a new method of catalyst preparation with the goal of practical applications. With success, however, the understanding can in turn be applied to the synthesis or improvement of new or existing catalysts [89].

Despite the massive demand for alternative fuel cell catalysts, the noble metal Platinum and its alloys (see chapter 4 and 5) continue to be the applied standard systems everything else is compared to. And although they are far away from perfect performance, no other electrocatalyst has been able to fulfill the requirements of a reasonable substitute so far. Consequently recent efforts have been launched to revisit the electrochemical reactions occurring on Pt model surfaces, in order to further improve our knowledge and eventually optimize catalysts for practical

applications. In this manner some of the previous work on the surface structure of these model systems will be reviewed and afterwards related to the kinetic information obtained by electrochemical measurements in this chapter.

3.1. Surface Structure of model systems

The current knowledge of the surface structure and composition on the atomic scale at the metal-liquid interface has originally emerged out of ex-situ UHV studies. Techniques such as XPS, AES, LEISS or low-energy electron diffraction (LEED) enable the study of the clean metal surfaces, before the influence of the electrolyte is introduced. Single crystal samples, which can be characterized by a set of Miller indices that indicate the particular crystallographic orientation of the surface plane relative to the bulk lattice [90], have been generally applied in this context due to their high two-dimensional periodic structure. In particular those with low indices, i.e. (100), (110) and (111) for a face-centered cubic (fcc) metal like Pt (see Figure 3.1), are of special interest for fundamental studies in heterogeneous catalysis [91].
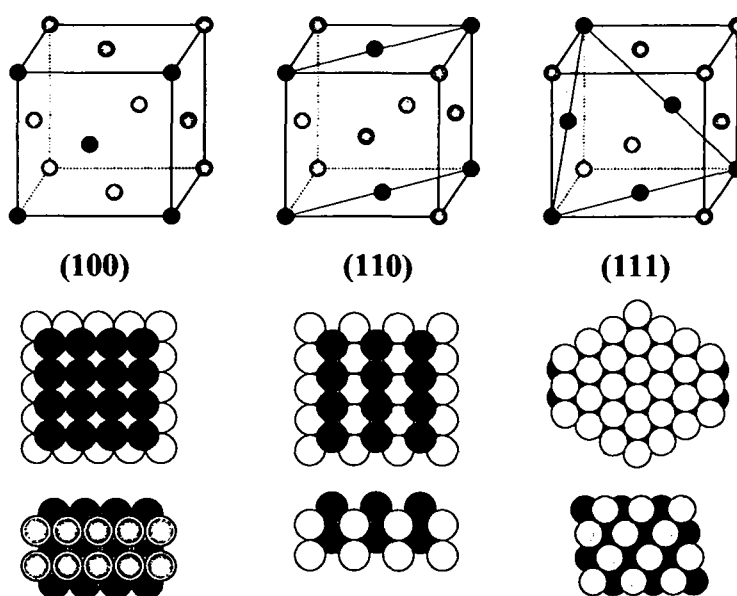

Figure 3.1: Surface structure of ideal face-centered cubic single crystals

28

As on most metals, however, even these ideal structures can be modified by surface atom rearrangements to minimize their surface energy relative to their environment. In order to accommodate for unsaturated coordination compared to the ideal bulk lattice, either the interlayer spacing changes in the near-surface region by relaxation, or even more drastic displacements of atoms in the outermost layer from their equilibrium position can be observed by so-called reconstruction. Moreover the adsorption of molecules like hydrogen, oxygen or carbon monoxide, and formation of other strong adsorbate-substrate bonds can alter the relaxation as well as the reconstruction dramatically. Unfortunately the full spectrum of these phenomena goes far beyond the scope of this work, details can however be found for instance in the review by Markovic et al. [8].

Many of the properties of the metal-gas interface have also been highly relevant for the understanding of the metal-liquid interface. Additional advances in the in-situ methods of Scanning Tunneling Microscopy (STM) [92] and Surface X-ray Scattering (SXS) [93], accompanied by the development of the flame-annealing preparation method by Clavilier [94], have rendered the determination of the surface structure possible even during electrolyte exposure and under potential control. Again, reconstruction and relaxation due to the solvent or anion adsorption have been studied extensively and are reported in refs. [8;95]. Hence it was shown for instance for a well-ordered Pt(111) electrode that anions, hydrogenated and oxygenated species only adsorb reversibly as long as the potential remains between 0.0 and $0.8V_{RHE}$, and the structure remains intact and well-ordered. If the potential however is increased beyond 0.8V to form an "oxide", place exchange between OH_{ad} and Pt atoms in the first layers initiates an irreversible roughening of the surface, creating ad-atoms and vacancies on the originally smooth surface until a complete loss of periodicity occurs [96]. Similar findings on the other single crystal facets substantiate the importance of this oxidation effect, which has an extensive impact on the corrosion of real catalysts amongst others.

In order to examine the role of edges and corners, as well as step- and defect-sites, which are essential parts of real catalysts, high Miller Index surfaces of metals with step like imperfections in an otherwise atomically flat low index surface are usually investigated. This approach using controlled step density and step geometry was pioneered by Somorjai et al. [97] for gas-phase catalysis and only considerably later introduced to electrochemistry [98;99], due to the additional difficulties of electrolyte- and potential-induced reconstruction. The impact of stepped surfaces for instance on the electrochemical oxidation of a CO monolayer on Pt was recently

demonstrated in the work of Lebedeva et al. [33;100], and the profound consequences for the same reaction on real catalysts will also be discussed later in this work (see sections 3.2.2 and 4.4.1).

3.2. Electrochemical Measurements

The experiments discussed in this chapter were conducted on polycrystalline Pt and Pt single crystals (Pt(hkl)) with the same geometric area of 0.283 cm² (the Pt-alloy crystals as well as the glassy carbon electrode support for the Pt high surface area catalysts were also of the same size). The preparation procedure of the Pt-poly and the Pt(hkl) samples (*MaTeck,*), and the subsequent mounting in the RRDE or thin layer configuration strictly followed the method described by Markovic et al. [24]. Before each measurement the crystals, for which a miscut of 0.5° was determined by using X-ray diffraction [101], were flame annealed in a hydrogen flame and afterwards slowly cooled down to room temperature in a mild stream of Argon [102;103]. To protect the crystal surface against contamination from the atmosphere, it was immediately covered by a droplet of ultra pure, triply-pyrolitically distilled water [24] upon removal from the Ar-stream. The crystal was transferred onto a clean polypropylene film, with the surface facing down. The edges were carefully dried and then it was mounted either into the disc electrode position of an insertable disc electrode assembly (*Pine Instruments*) or in the electrode position of the spectroelectrochemical cell. Afterwards the electrode was transferred into the corresponding electrochemical cell and immersed into the Argon (Ar) saturated electrolyte under potential control.

3.2.1. Cyclovoltammetry in Ar purged solution

The determination of cyclic voltammograms in an electrolyte saturated with an inert gas such as Ar are essential experiments for all types of electrodes, providing information regarding the interaction between the surface and the electrolyte, e.g. about ranges of potential limits of stability or the thermodynamics of various adsorption/desorption processes. In other words, CV's are the electrochemical fingerprints of a particular electrode surface in a certain electrolyte and at a given temperature. However, in contrast to gas phase catalysis where a distinction between different adsorbates is rather simple, additional and more selective experimental techniques have to be employed to correctly resolve and interpret the CV data. Unfortunately this is not always possible, subsequently the assignment of CV characteristics for single crystals and later also for

nanoparticles is often intuitive and indirect (see 4.1.2.1 and 4.3.2). The cyclovoltammograms for various extended Pt crystals in Ar purged perchloric acid solution between 0.05 and $1V_{RHE}$ are demonstrated below in Figure 3.2.
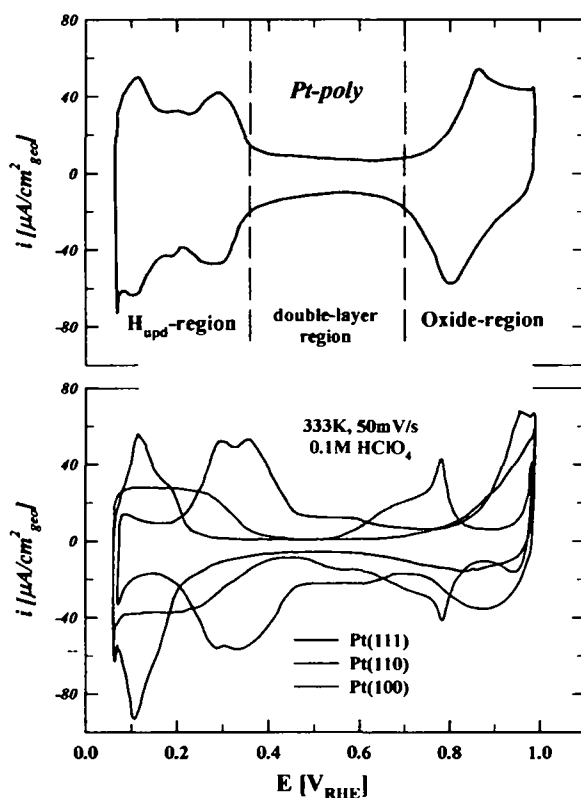
Figure 3.2: Cyclovoltammograms of flame-annealed Pt-poly (top) and Pt(hkl) surfaces (bottom) in Ar saturated, 0.1M perchloric acid at 333K with a scan rate of 50mV/s.

The voltammetric curve in Figure 3.2 for Pt-poly can be divided into the three characteristic potential regions as indicated. Between the negative limit of 0.05V, where approximately the hydrogen evolution starts at low hydrogen partial pressure, and ~0.4V two current peaks occur, which have been attributed to the reversible adsorption/desorption of underpotentially deposited hydrogen, hereafter denoted as H_{upd} [8]. From 0.4V to ~0.7V a small, constant current describes the so-called double-layer region, where the charge is considered to establish the electrochemical double layer at the surface without any specific adsorption process taking place. Positive of 0.7V the adsorption of oxygenated species initiates the oxidation of the Pt surface, which is partially irreversible as can be seen from the unsymmetrical shape and the negative shift of the oxide reduction peak compared to the anodic curve. There is a general uncertainty about the exact physical processes associated with either the reversible adsorption of OH_{ad} or with the irreversible "oxide" formation, since they are often not clearly separated. To avoid getting lost in a discussion

about the formalism of mechanism that cannot be distinguished by our means anyway, adsorbed oxygenated species will hereafter simply be denoted as OH_{ad}.

Usually the positive potential limit for the cyclovoltammograms of the Pt(hkl) is restricted to about 0.6V in order to prevent disordering of the well-oriented surfaces (see section 3.1). When the potential is increased to values exceeding ca. 1.0V, an "oxide" can be formed by site-exchange between OH_{ad} and Pt atoms in the first layer and the surface becomes irreversibly roughened [104]. However, considering the potential interval in which the ORR and CO_{ad} oxidation takes place, the CV's in Figure 3.2 for Pt(hkl) were recorded with an anodic potential limit of 1.0V in order to identify the adsorption phenomena caused by the electrolyte. All curves are in agreement with those previously reported in literature for well ordered single crystal surfaces, whose surface structure and composition were determined by ex-situ and in-situ techniques [105]. The main features of the Pt(111) surface are highly symmetrical peaks for H_{upd} and the so-called "butterfly" peak (0.5V-0.85V), but also an irreversible adsorption of OH_{ad} above 0.9V. The "butterfly" peak is associated with the formation of a well-ordered anion overlayer and is especially pronounced in sulfuric and perchloric acid, because of the perfect symmetry match between the fcc (111) face and the C_{3v} geometry of the oxygen atoms in the sulfate and perchlorate anion. The main characteristics of the Pt(110) and Pt(100) crystal are also a reversible H_{upd} region and asymmetric OH_{ad} adsorption/desorption peaks at potentials above ~0.75V. Although still denoted as H_{upd}, it has been shown that for both surfaces the features in this region correspond to the *coupled* processes of hydrogen adsorption and anion desorption. This is due to the different adsorption enthalpies on terrace sites compared to step sites for these model systems, produced by the miscut and the reconstruction phenomena occurring in electrolyte [8]. The fact that OH_{ad} can be adsorbed even at potentials as low as 0.2V has a considerable effect on the kinetics of in particular the CO oxidation (see chapter 3.2.2 and 4.4).

Since CV's are also the first indicators of the presence of anionic and organic impurities that can alter the reaction mechanism at the Pt surfaces [8], the electrodes have only been used for further analysis of the reactions of interest, when well-known, reproducible curves in Ar-purged solution were obtained.

3.2.2. Anodic CO Oxidation Reaction

The surface electrochemistry of CO adsorbed on transition metal surfaces has been the subject of intensive theoretical and experimental work [8]. In these studies emphasis has been focused on linking the microscopic structure information concerning the CO adlayer structures on single crystal surfaces to the thermodynamics and other macroscopic electrochemical responses at electrified interfaces. Whereas information regarding macroscopic properties has been provided by classical electrochemical techniques, the chemical, physical and structural properties that occur on the atomic scale have been obtained from either a combination of in-situ scanning tunneling microscopy and vibrational spectroscopy [29;106] or surface X-ray diffraction and vibrational spectroscopy [29]. Since it is sheer impossible to cover all the aspects of the reaction in its entirety, the focus will be on some of the more practical issues that will also be significant for the later investigation of the same reaction on high-surface area catalysts. For this reason the following two subchapters deal first with the intriguing results concerning the oxidation of an adsorbed monolayer of CO and afterwards with the bulk oxidation of dissolved CO.

3.2.2.1. CO monolayer oxidation – CO stripping

The adsorption of CO molecules at potentials below $0.5V_{RHE}$, where thermodynamically immediate oxidation to CO_2 should occur, is strongly irreversible on a Pt surface. As a consequence of this affinity, the catalyst becomes fully covered and inhibited for any reaction promotion, which is usually an undesired process. However, for fundamental purposes one of the ways to examine the kinetics of the oxidation of CO molecules is based exactly on this effect. Namely, with the CO stripping method, which can be done either potentiodynamic or chronoamperometric, the oxidation of such an adsorbed monolayer of CO is analyzed in an electrolyte free of dissolved CO. Typical potentiodynamic CO stripping curves for polycrystalline Pt and single crystals in perchloric acid at room temperature can be seen in Figure 3.3:
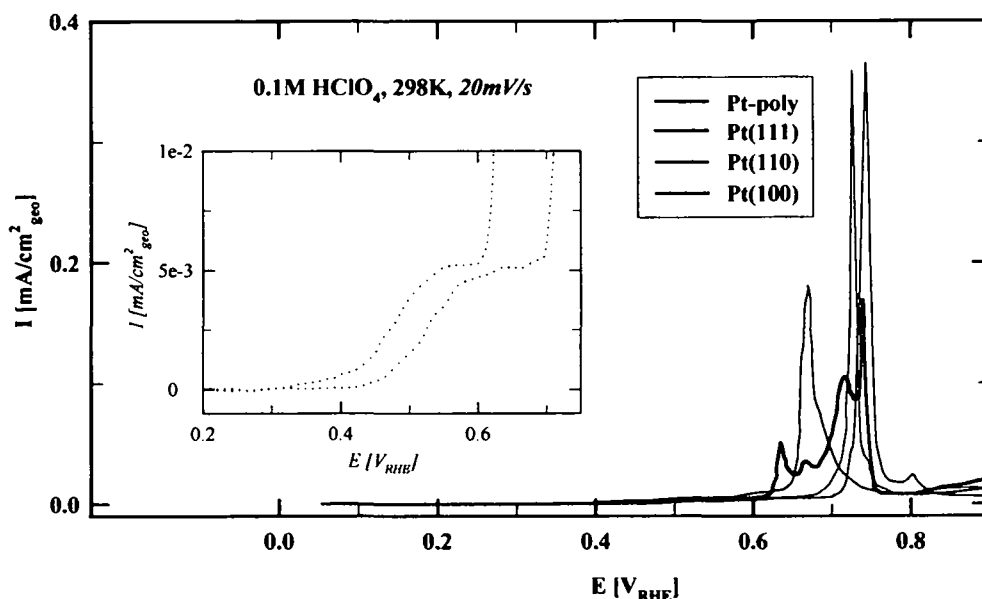
Figure 3.3: CO stripping curves for Pt-poly and Pt(hkl) in 0.1M perchloric acid at 298K with 20 mV/s; insert (b) shows a magnification of Pt(111) and poly-Pt in the pre-ignition region.

Previous to recording of the polarization curves, CO was adsorbed at the electrode while the potential was held at 0.05V for at least five minutes with occasional rotating of the disc, to ensure a saturated coverage of the surface. Afterwards the electrolyte was purged with Argon for more than twenty minutes to remove of residual CO from solution. When the potential is then swept to positive values, initially no current signal is detected up to approximately 0.3V, indicating the irreversible adsorption. The onset of the oxidation, which is more obvious from the magnified insert (b) of Figure 3.3, is very difficult to determine exactly from simple electrochemical measurements, but lies somewhere in the vicinity of 0.35V. Since the Langmuir-Hinshelwood mechanism was proposed as the most plausible reaction mechanism (see introduction), i.e. both CO_{ad} and OH_{ad} have to be co-adsorbed on the surface in order to react with each other, this supports the previous suggestion that the adsorption of OH_{ad}-species already begins in the H_{upd} region at potentials below 0.4V (see 3.2.1). Only relatively small currents are observed thereafter up to about 0.6 to 0.7V depending on the type of electrode, at which finally the oxidation of the main part of CO occurs more rapidly, indicated by a sharp peak in the CV. Accordingly, the point where the reaction rate increases steeply is generally labeled as the "ignition potential", whereas the potential region before that is simply referred to as the "pre-ignition region" [31,32]. Originally

this behavior was rationalized by two different states of CO adsorption on Pt, characterized by a low and a high enthalpy of adsorption, respectively. This was inferred from the UHV studies on the Pt/CO system, where the heat of adsorption of CO is found to be strongly coverage dependent and arises primarily from repulsive adsorbate-adsorbate interactions [107]. Thus it was suggested that at high coverages all CO_{ad} molecules are in a weakly adsorbed state due to the internal repulsions, and only when the CO coverage is reduced by oxidative removal of CO, the remaining CO_{ad} molecules relax into a more strongly adsorbed adlayer, which is oxidized at much higher potentials [34]. Also other models have been proposed for the CO oxidation, for instance Bergelin et al. [108,109] suggested that in the pre-ignition region the CO oxidation proceeds through an Eley-Rideal rather than a Langmuir-Hinshelwood mechanism. However, a reaction between "activated" water molecules and CO_{ad} in the electrical double-layer of the electrode surface does not seem very likely, considering the recent calculations by Dunietz et al. [54].

In order to further investigate this issue, a novel procedure to form a saturated CO adlayer on the Pt nanoparticles was introduced. In contrast to the former procedure, denoted hereafter as "oxide-annealing", in which the catalyst was cycled in Ar saturated solution until a well-established cyclic voltammogram was observed before CO was adsorbed at 0.05 V, in the second procedure, denoted hereafter as "CO-annealing", the electrode was cycled in CO saturated solution between 0.05 < E < 1.0 V for 5min, before holding at 0.05 V for 5min and then purging the CO from the electrolyte with Ar for 20min. This experimental approach was applied because it was recently found that the "CO-annealing" pretreatment of Pt(111) may facilitate the removal of surface irregularities, which are inherently present on the Pt(111) surface after the flame annealing preparation method [110]. As a consequence, upon CO-annealing of the (111) surface the domain size of the p(2x2)-3CO structure, which is formed on Pt(111) at low potentials, is significantly improved [111]. As demonstrated further below, the catalytic and spectroscopic properties of single crystals pre-treated by these two methods are completely different.
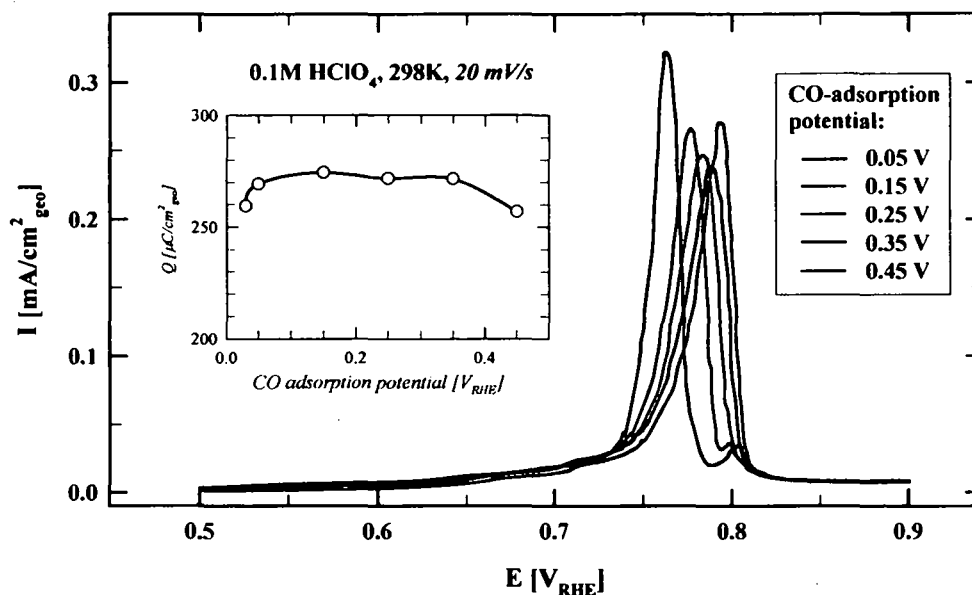
Figure 3.4: CO stripping on Pt(111) of CO adlayers adsorbed at various potentials; in 0.1M perchloric acid at 298K with 20 mV/s; inset (b): integrated charge underneath the peak areas against the potential where CO was adsorbed initially. The integration was done in the interval from 0.5V to 0.85V, without correcting for the capacity obtained in a standard CV, which is the same for all adsorption potentials.

Before the stripping curves acquired after different pretreatment are compared to each other, however, one uncertainty that evidently arises with these procedures has to be eliminated. Namely, the formation of the CO adlayer by the CO-annealing technique takes place during the final negative sweep of the annealing procedure and thus mainly at potentials around 0.4V-0.5V, whereas after oxide-annealing CO is adsorbed at the constant electrode potential of 0.05V. The impact of the CO adsorption potential on the CO monolayer oxidation on an oxide-annealed Pt(111) surface is analyzed in Figure 3.4. Thereby it becomes obvious that over an adsorption potential range from 0.03V to 0.45V the CO stripping peak only varies by ca. 30mV, slightly shifting positive with a more positive adsorption potential. This can be rationalized, in line with the conclusions drawn from the results described in the following, by an enhanced co-adsorption of supporting anion from electrolyte at higher CO adsorption potentials, which in turn inhibits the adsorption of reactive OH_{ad} at defects suitable to initiate the oxidation. Note that the charge required to oxidize the CO adlayer, calculated from the area underneath the peak (see insert Figure 3.4b), is almost independent of the adsorption potential. Only a slight decrease in the

oxidation charge is noticed at the highest potentials, indicating that a full coverage by CO cannot be achieved any more, since partial oxidation already starts during the adsorption.

When the stripping curves of CO from the electrodes prepared by the two different methods discussed earlier are now compared to each other, a similar positive shift in the oxidation peak potential for the CO-annealed surface becomes obvious in Figure 3.5, however, to a more pronounced extent. To make completely sure that this is not an artifact due to the extraordinary adsorption conditions, a third oxidation experiment was conducted. Immediately upon the total removal of the CO-adlayer after the measurement of the CO-annealed surface (stripping curve 2), the potential was reversed and stopped at the negative limit of 0.05V, to avoid any modification of the surface structure by adsorption of irreversible oxide species from electrolyte [96]. Thereon CO was adsorbed and stripped following the same procedure as for the oxide-annealed surface (stripping curve 1). From the according stripping curve 3 it can be clearly seen, that despite the equivalent adsorption potential as for the oxide-annealed surface, a significant positive shift in the peak position of about 50mV occurs indicating a less defected surface. The difference between the peaks in curve 2 and 3 is thus approximately 30mV, which equals the variation demonstrated earlier in Figure 3.4 between the adsorption potential of 0.05V and 0.45V. This in turn means that the 50mV difference between the curves 1 and 3 originates from a real change in the surface structure due to the annealing process and therefore in the way the CO adlayer is oxidized, and is no experimental artifact.
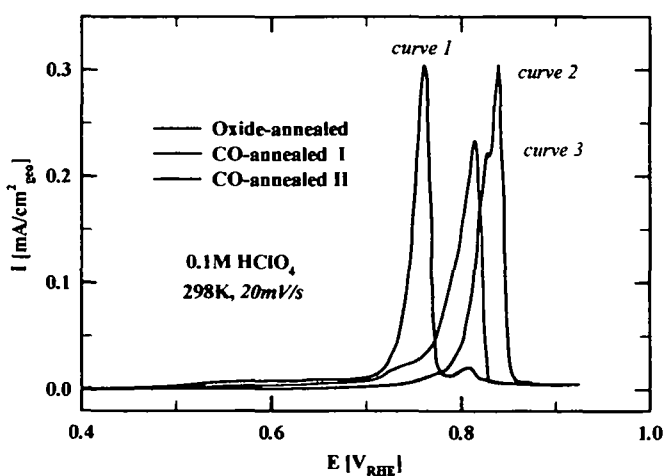
Figure 3.5: CO-stripping on Pt(111): comparison of oxide annealing (curve 1), CO-annealing (curve 2) and the second sweep after CO-annealing (curve 3); for details see text.

Considering that the oxide-annealed Pt(111) surface, which contains much more defects than the well-ordered CO-annealed surface, is more reactive, it is concluded that the oxidation rate of a CO monolayer (CO stripping conditions) is controlled by the presence of catalytically active OH_{ad} that is formed on defect sites, rather than by the Pt-CO bond strength or the CO surface mobility. Castell et al. [112] came to a similar conclusion for the gas-phase CO oxidation from their studies of laser-induced defects on a Pt(111) surface. They attributed the higher reactivity to a higher sticking coefficient of oxygen to defects compared to smooth terrace sites. This assumption is further supported by the finding that the rate of electrooxidation of CO on stepped single crystal surfaces is proportional to the step fraction, proving that steps and defects are the active centers for the CO adlayer oxidation [33;100].
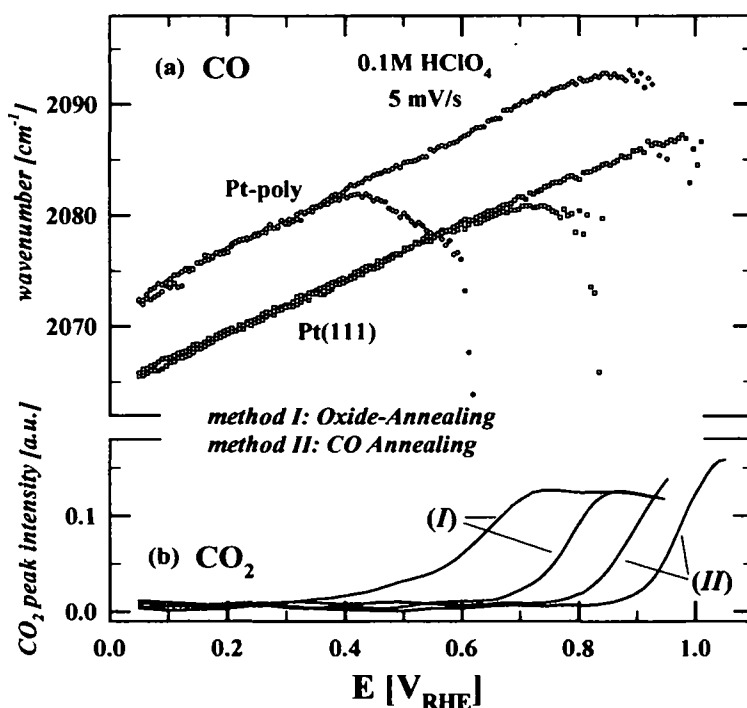
Figure 3.6: Comparison of CO stripping on Pt(111) (oxide annealed is red and CO annealed dark red) and poly-Pt (oxide annealed is blue and CO annealed dark blue) using FTIR. The top part depicts the frequency of the on-top adsorbed CO band, at the bottom is the peak intensity for dissolved CO_2 on the same potential scale.

The effect of the different preparation procedures on the Pt model systems can alternatively be investigated with the FTIR methodology for extended surfaces, which will also aid the understanding of the later analysis of the high-surface area catalysts (section 4.4.1.2) substantially. The characteristic C-O stretching frequencies of CO_{ad} in CO-free, 0.1M $HClO_4$ electrolyte at the

adsorption potential of 0.05V are presented in Figure 3.6 for the Pt single crystals and poly-Pt. For the background correction a spectrum was collected at 0.9V, where CO_{ad} is completely oxidized, and subtracted from the original ones for each system. As previously described by several authors [113;114], at potentials below 0.3V the C-O stretching bands near 2070cm^{-1} and 1740cm^{-1} predominate in the spectra of for instance Pt(111), which can be assigned to CO bound on atop and three-fold hollow sites, respectively. When the potential is swept to more anodic potentials, another band at ca. 1800cm^{-1} appears, indicating the transformation of the adlayer structure and the formation of bridge-bonded CO (not shown). In literature [28] this has been attributed to the loss of the ordered p(2x2)-3CO structure, which is initiated by the onset of the CO oxidation in the pre-ignition region. Concomitantly, a peak starts to develop at around 2343cm^{-1} for the product of the reaction CO_2. In contrast to the characteristic CO signals, however, the peak position of CO_2 is independent of the applied potential because the molecule is dissolved in electrolyte and not adsorbed at the surface of the electrode.

In Figure 3.6 (b) and (c) it is exemplarily demonstrated how the frequency of atop CO and the intensity of the CO_2-band is changing with the potential for Pt(111) as well as poly-Pt (Pt(110) and Pt(100) are not shown for clarity, but behave very similar). Three distinct potential regions can be discerned from the v_{CO} vs. E and I_{CO2} vs. E plots, the same as already described above for the CV. For oxide-annealed poly-Pt the CO-adlayer is stable initially up to about 0.35V, since no CO_2 production is visible and a linear frequency shift dv/dE of about 25mV/cm^{-1} is observed, consistent with the so-called electrochemical Stark-tuning effect [75]. Between ~0.35 and ~0.6V the Stark-tuning slope changes its sign while simultaneously a weak CO_2 band is detected in the spectra. This indicates a slow but finite CO oxidation rate, in accordance with the previous statements about the pre-ignition region. Finally above the ignition potential at ca. 0.6V a fast increase in I_{CO2} as well as a complete disappearance of the atop CO peak is observed by facile CO oxidation kinetics. Comparing Pt(111) to poly-Pt it becomes obvious, that the oxidation of a CO monolayer is slower on former electrode due to the fewer defects on the surface. The necessary OH_{ad} atoms cannot adsorb at the same low potential, which leads to a shift in the onset of the ignition region of almost 200mV under given reaction conditions. Moreover the significant impact of the CO-annealing procedure is clearly shown for both electrodes. Hardly any pre-ignition region can be detected, instead only an ignition point at the remarkably positive potential of ~0.9V can be discerned.

Recapitulating, in this chapter the current literature on the subject of the CO monolayer oxidation was succinctly reviewed. In addition novel evidence for the major role of "irregularities" or "defects" in the surface structure on the reaction kinetics were presented, by utilizing two different preparation procedures for the electrodes. This was demonstrated by electrochemical techniques as well as in-situ FTIR measurements.

3.2.2.2. CO bulk oxidation

Although CO stripping curves provide valuable information on the oxidative removal of CO, in practical applications the catalyst usually experiences a continuous supply of CO to the surface. This can be simulated by means of RDE measurements in a CO saturated electrolyte, i.e. CO bulk oxidation or CO_b. The forced electrolyte convection leads to well-defined diffusion characteristics at the disc electrode [71], which are necessary for the analysis of reaction kinetics. Considering Pt(110) as an example, a typical CO bulk oxidation curve for the Pt single crystals is presented below.
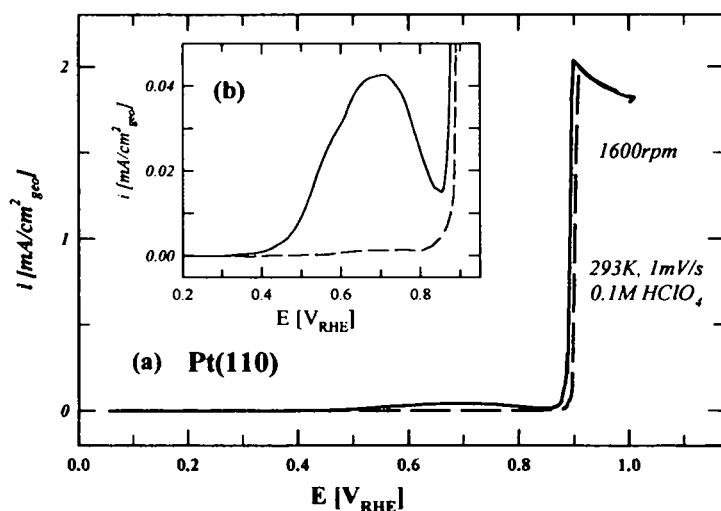
Figure 3.7: Positive sweeps of the CO bulk oxidation on Pt(110). The solid curve displays the "oxide" annealed and dashed the CO annealed surface. Both experiments were conducted under the same conditions; 293K, 1mV/s and 1600rpm in 0.1M $HClO_4$. Insert (b) shows a magnification of the pre-ignition region.

Similar to the previously described CO-stripping, initially no current signal is detected up to approximately 0.3V because a stable CO adlayer is inhibiting the adsorption of oxygenated species necessary for the oxidation. Then a small but distinct peak in between 0.3 and 0.9V (see insert in Figure 3.7) arises due to the oxidation of CO in the pre-ignition region. At the ignition potential the current rises steeply from almost zero to the diffusion limit, i.e. thereafter every CO molecule

diffusing to the electrode surface is immediately oxidized and the reaction is controlled by mass-transfer only. Upon the reversal of the electrode potential at 1.0V, the surface becomes covered again by poisoning CO at about the ignition potential when the signal drops back to zero. Analog to the CO stripping, the above described features of the bulk oxidation were originally explained by a distinction between weakly and strongly adsorbed CO (see 3.2.2.1), where the former are removed in the pre-ignition region and as a consequence the remaining layer becomes more strongly adsorbed and is not oxidized up to the ignition potential [8]. Quite interesting is furthermore that a positive reaction order with respect to the partial CO pressure was found in the pre-ignition region, whereas at the ignition potential the corresponding order is negative. This was explained in accordance with the Langmuir-Hinshelwood mechanism by a change from non-competitive to competitive adsorption of the reactants OH_{ad} and CO_{ad}.

Based on the results from CO-stripping, however, the CO_b curves can also be interpreted in a different fashion. The initiation of the reaction again overlaps with the initial adsorption of OH_{ad} at the defect sites, which leads to more free surface sites in adjacent positions. Reducing the number of those surface defects by CO annealing makes the pre-ignition region vanish completely (dashed curve in Figure 3.7). In contrast to stripping, the rotation of the electrode promotes the diffusion rate and adsorption of dissolved CO instead of reactive OH_{ad} and consequently the continuation of the reaction is inhibited, which is obvious from the decrease in the pre-ignition peak before the ignition potential is reached. Moreover the ignition potential itself, where the equilibrium between CO oxidation at defects and CO re-adsorption switches to the benefit of the former and the reaction becomes self sustained, shifts in positive direction relative to the stripping peak for the monolayer oxidation on the same electrode, due to the virtual stabilization of the CO adlayer by the continuing adsorption of CO. From this finding the somewhat surprising negative reaction order at the ignition potential can be ascribed to the fact that the reduction of the CO partial pressure decreases the probability of CO adsorption. Since the equilibrium surface coverage by CO_{ad} is lower at small CO partial pressures, more active sites remain available for OH_{ad} adsorption and thus the ignition of the oxidation process shifts to more negative potentials.

The role of the anion from the supporting electrolyte on the kinetics of CO electrooxidation has been pointed out previously in more detail [35;115] by comparing polarization curves in various solutions. In alkaline electrolyte the oxidation begins at lower potential in the pre-ignition as well as in the ignition region, since no other anion is competing for adsorption sites with the oxidizing

species OH. In contrast in acid electrolyte anions like ClO_4^- or HSO_4^- occupy especially defects and step sites as spectator/blocking species, since the excess surface charge of those sites is intrinsically attractive for anions, and prevent the formation of OH_{ad}. Furthermore the addition of anions that are specifically adsorbed with a higher strength, i.e. Cl^- or Br^-, inhibits the oxidation of CO even stronger.

Unfortunately, as will be demonstrated later in section 4.4.1.3 for HSAC, it is impossible to correlate FTIR measurements in CO saturated solutions to the CO bulk oxidation at a rotating-ring electrode because of the decisively different hydrodynamic conditions. In the thin-layer setup the diffusion to as well as from the electrode is extremely hindered, since the surface is pressed tightly onto the FTIR prism. Therefore no meaningful data can be extracted from such an experiment, and the aid from spectroscopic techniques remains restricted to the CO monolayer oxidation.

3.2.3. Cathodic Oxygen Reduction Reaction (ORR)

The reduction of oxygen is considered to be one of the most important electrocatalytic reactions due to its major role in electrochemical energy conversion, corrosion and several industrial processes. Despite the decades of research efforts on the subject, the complex kinetics still continue to be challenging. The reasons for not achieving the thermodynamic reversible potential of 1.23V for a four-electron reduction even on the best catalysts and the concomitant marginal exchange current densities in the order of 10^{-10} A/cm^2 remain an especially intriguing problem [116;117]. With the advances in structure sensitive analytical techniques, recent work has primarily focused on relating the surface properties with the activity of electrocatalysts, and the progress has been presented in numerous reviews [8;118]. Following this surface science approach, this chapter should serve as an introduction into the current knowledge about the ORR on extended Pt surfaces, but also to build a basis for a possible explanation of the effects seen on high surface area catalysts later on (see paragraph 4). In addition the activities of those model systems will be benchmarked to be able to compare them to the Pt nanoparticles, and discuss potential sources of errors in the estimation.

3.2.3.1. The mechanism of the ORR on Pt

Based on selected examples the results from the measurements of the ORR on extended surfaces in weakly adsorbing acid electrolyte will be presented. Below in Figure 3.8 anodic curves for the ORR (a) and the simultaneously pertained H_2O_2-production (b) are presented for Pt(111) as a function of the rotation rate of the RRDE.
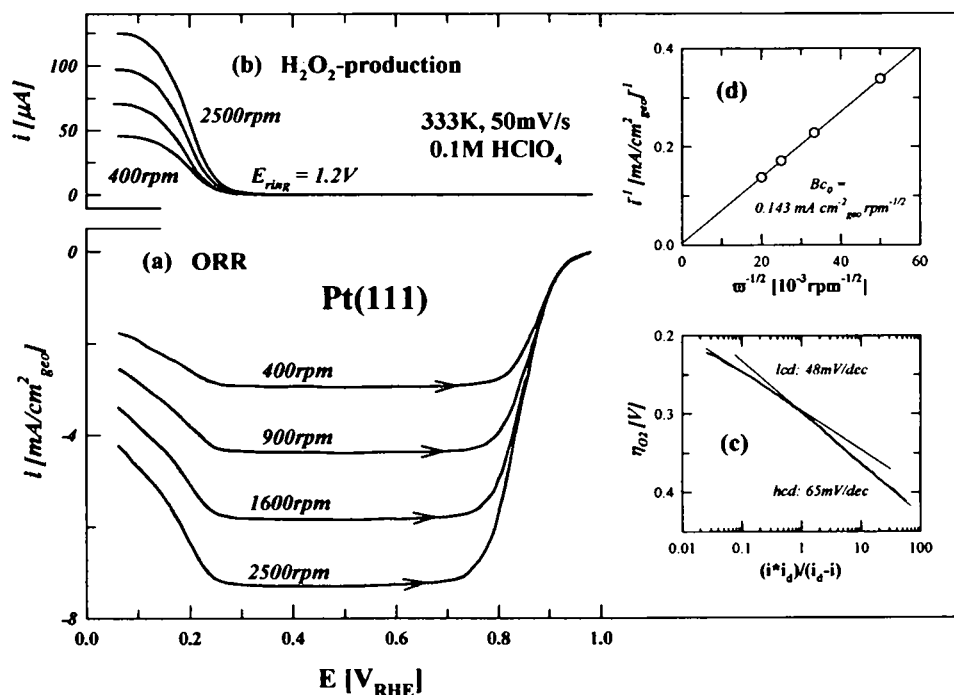
Figure 3.8: ORR (a) and H2O2-production (b) on a Pt(111) disc electrode at various rotation rates. Measurements were conducted at 333K with 50mV/s in 0.1M HClO₄. (c) Tafel plot of the specific activity with linear approximations for the high and low current density region (hcd and lcd). (d) Levich-Koutecky plot derived from the diffusion-limited current for the ORR at 0.6V.

In all potentiodynamic studies of the ORR only the positive sweep was analyzed, since then the Pt surface is initially free of OH_{ad} as discussed previously in section 3.2.1. Between 1.0V to 0.8V the reaction proceeds under pure kinetic and mixed-kinetic/diffusion control. A constant current down to about 0.3V indicates that the reduction proceeds thereafter at the diffusion-limited rate, which depends only on the thickness of the diffusion layer as a function of the rotation rate (chapter 2.1.1). Negative of 0.3V in the H_{upd} region the absolute current declines again and concomitantly significant peroxide production occurs, which can be detected at the ring (Figure 3.8b). This is in particular pronounced for the Pt(111) surface and to a lesser degree for the other single crystals and Pt-poly (not shown), and was attributed to the blocking of O-O bond

breaking sites by adsorbed hydrogen dependent on the crystallographic orientation [23]. Note that the potential of the ring was held constant at $1.2V_{RHE}$ during the whole measurement, since then the peroxide oxidation proceeds in the diffusion-limited region (see 2.1.1).

The linear dependence of the diffusion limited currents in a Levich-Koutecky plot in Figure 3.8d indicates that the ORR is of first order with respect to the oxygen partial pressure. The slope Bc_0 of 0.143 $mAcm^{-2}_{geo}rpm^{-1/2}$ (see equation (2.3)) is close to the theoretical value of 0.136 $mAcm^{-2}_{geo}rpm^{-1/2}$ for a four-electron reaction [8], which is a confirmation of adequate quality of the hydrodynamic conditions for the measurements and therefore enables the following derivation of the essential equation (3.1). Since usually the potential region where the current is solely depending on the electron transfer (i.e. the diffusion limitations can be neglected) is too narrow, a simple mathematical correction is introduced to evaluate the intrinsic catalytic activity, i.e. the kinetic current density j_k (or also the specific activity), from the experimental current density j in the mixed kinetic/diffusion controlled region using the diffusion limited current density j_d:

$$\frac{1}{j} = \frac{1}{j_d} + \frac{1}{j_k} \quad \text{or} \quad j_k = \frac{j_d \times j}{j_d - j} \tag{3.1}$$

The potential can be plotted against the logarithmic value of the resulting kinetic current density in a so-called Tafel plot, as shown in Figure 3.8c for Pt(111). Note that curves for the same crystal but different rotation rates overlap from this aspect due to the correction for the diffusion limit. In the case of Pt(111) two straight Tafel lines with different slopes could be extracted, one of 48mV per decade for the low current density region above 0.9V and one of 65mV/dec for the high current density region. At different temperatures the polarization curves for the ORR on Pt(111) and the pertaining Tafel plots differ slightly from that taken at 333K, which are displayed in Figure 3.9.
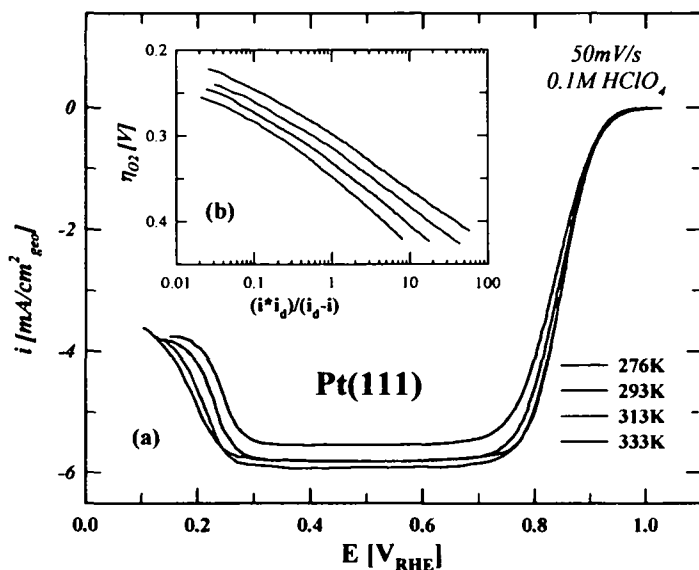
Figure 3.9: Temperature dependence of the ORR on Pt(111) in 0.1M HClO4. (a) polarization curves as recorded plotted against the RHE. Insert (b): Tafel plots using the overpotential against the theoretical potential of a reversible oxygen electrode as the y-axis.

When the recorded curves are compared with each other on the scale of the RHE (Figure 3.9a), almost no difference can be observed. However, the Tafel plots in Figure 3.9b using the overpotential η_{O2}, calculated against the theoretical potential of a reversible oxygen electrode, clearly demonstrate the increasing reaction rate with temperature. This trend is generally expected from exothermic reactions considering the principal laws of kinetics. Unfortunately the true activation energy E_a which is defined in electrochemistry at an overpotential of $\eta=0$ (equilibrium state), is not directly accessible for the ORR because of its irreversibility. Furthermore efforts to deduce this value by extrapolating Tafel plots to the reversible oxygen potential and utilizing thus achieved exchange current density j_k^0 usually fail due to the non-linear behavior of such plots (see Figure 3.11). As a consequence the energetic parameter of choice for comparisons of the ORR on various Pt-systems is the apparent activation energy E_a^* at a fixed overpotential, which can be calculated from the Tafel plots at various temperatures with:

$$\left.\frac{\delta(\log j_k)}{\delta(1/T)}\right|_\eta = \frac{\Delta E_a^*}{2.3 * R}$$

(3.2)

The determination of the apparent activation energies of Pt-poly and Pt(hkl) at an overpotential of 0.3V is given in Figure 3.10. The absolute values calculated from the slope of a linear approximation are not very significant as they are depending on the potential. However, the small

variation between 25kJ/mol to 32kJ/mol suggests that the basic reaction mechanism is the identical on all the crystals studied.
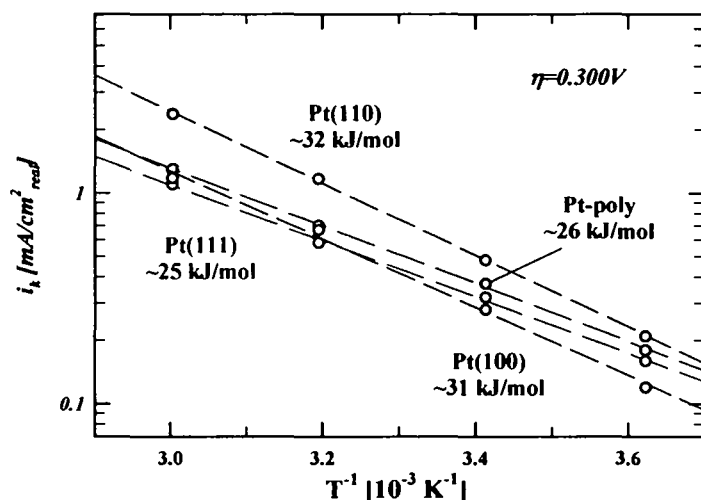
Figure 3.10: Arrhenius-plot for the ORR on various Pt model systems. The apparent activation energy was calculated from the kinetic current densities at an oxygen overpotential of 0.3V, using measurements at four different temperatures, 276K, 293K, 313K and 333K respectively.

It seems to be generally accepted that the ORR on Pt proceeds via a parallel reaction in acid electrolyte, with predominately a series pathway of four-electrons and adsorbed peroxide as an intermediate (see Figure 1.1), although the detailed mechanism still needs formulation. Different suggestions have been proposed regarding the first reaction step, which is considered to be rate determining (RDS). The most plausible perception was originally described by Damjanovic et al. [119] and later supported by the work of Sepa et al. [120;121], and is based on a slow charge transfer step, which occurs either simultaneously or is followed by a fast protonation reaction. The change in the Tafel slope from the low current density to the high current density region (from -RT/F to -2RT/F in their measurements), which is usually a sign for a change in the reaction mechanism, was explained alternatively by a variation in the adsorption conditions for the reaction intermediates. Since the energy of adsorption of these reaction intermediates decreases with increasing coverage with oxygen species, the energy of activation for a process involving strong adsorption of reaction products in the RDS increases. Therefore, at low current densities intermediate coverages exist and the ORR proceeds under Temkin adsorption conditions relatively sluggish, while in the high current density region the coverage with oxygen species is below a certain level and the RDS can be described assuming Langmuir adsorption. It should be pointed out here that the formation of OH_{ad} in above mechanism is assumed to originate from

the interaction of O_2 with Pt, however several other workers proposed that it is rather a product of the reaction of the aqueous electrolyte with the Pt surface at sufficiently positive potentials [23;122]. Using a slightly different approach, Yeager et al. proposed that the RDS for the ORR involves the chemisorption of an O_2 molecule at the surface without a proton transfer, based on the lack of a hydrogen-deuterium kinetic isotope effect [123]. Considering all this, the reaction rate of the ORR is determined either by the free platinum sites available for the adsorption of O_2 $(1-\Theta_{ad}$ term in equation (1.1)) and/or by the change of the Gibbs energy of adsorption of reaction intermediates with Θ_{OHad} ($f\Theta_{OHad}$ term in equation (1.1)).
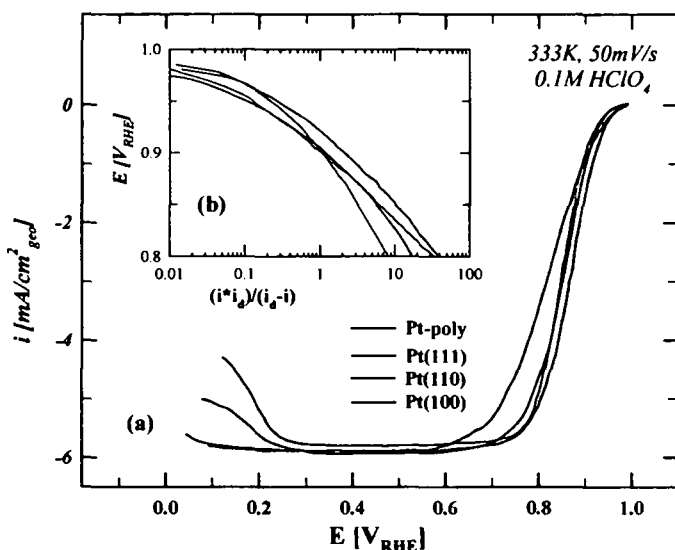
Figure 3.11: Comparison of the ORR on various Pt(hkl) and poly-Pt at 333K in 0.1M HClO₄. (a) polarization curves with 50mV/s and (b) diffusion-corrected kinetic current densities.

Although no change in reaction mechanism is expected because of the similar apparent activation energies shown above, a slight variation in the reaction rate of the ORR on poly-Pt and Pt(hkl) surfaces with the crystal face can be found in the specific activities in Figure 3.11, the reaction is therefore considered to be structure sensitive. This was also demonstrated in other electrolytes, partially to a much more pronounced effect because of stronger interactions between the Pt surface and the supporting anions that can block active sites [23;124]. In 0.1M perchloric acid between 0.8V and 0.9V the activity increases in the order of Pt(100)<Pt(111)~Pt-poly<Pt(110), with a factor of approximately 2-4 from the lowest to the highest current density. In agreement with the preceding discussion this structural sensitivity can be explained by the crystal orientation dependent adsorption of OH_{ad} spectator species, and its influence on the adsorption of O_2 and/or reaction intermediates [23].

3.2.3.2. Benchmarking of the ORR activities of Pt surfaces

For fundamental studies as well as practical applications unambiguous activity benchmarks are a prerequisite, in order to evaluate and compare results from catalysts with different composition and structure, or under various reaction conditions. Since the rotating disc method for extended surfaces has been introduced already in the 1960's, one would expect also very well established benchmark activities for such an important reaction as the ORR, which is however not the case. Based on the current knowledge a brief study should try to capture what causes the reported variations in literature.

The bulk crystal used for the purposes of this study exhibited a H_{upd} charge of 195 $\mu C/cm^2$ in perchloric acid electrolyte, averaged over a set of more than ten measurements. In literature H_{upd} charges for polycrystalline Pt samples range from about 190 to 220 $\mu C/cm^2$ in perchloric and sulfuric acid, indicating the subjectivity of its estimation. However, this would only lead to an error in precision of approximately 10% and can consequently not account for differences in activity in the order of several magnitudes. Roughly the same applies for the allocation error of the potential and current reading. When the potential of the reversible hydrogen electrode is obtained immediately before or after the oxygen reduction reaction, the precision due to the potential reading should be optimized and remain less than 5%.
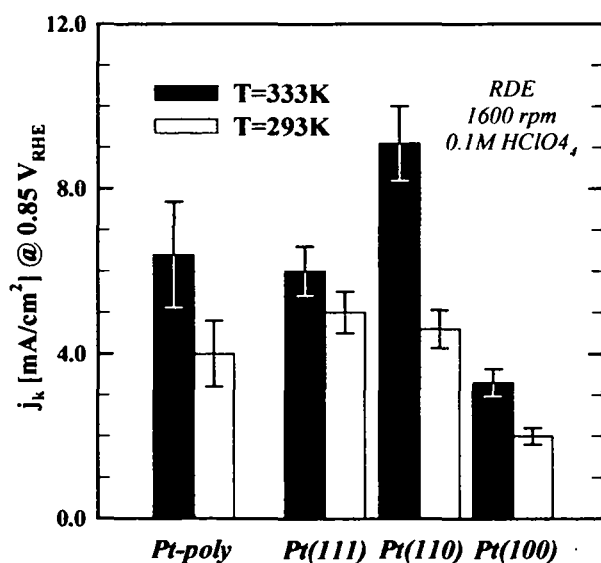
Figure 3.12: Activity comparison of Pt(hkl) and Pt-poly in 0.1M perchloric acid at 333K and 293K. The kinetic current density was calculated from the diffusion corrected current density at 0.85V at 1600rpm.

Another error could be introduced by the differences in the preparation procedures that have been applied for bulk Pt samples. The polycrystalline Pt in this study was flame annealed in a hydrogen flame and cooled down in Argon for 5 minutes [94;102]. The crystal was then protected by a drop of triply-pyrolitically distilled water and transferred onto a clean film, dried on the edges and mounted into the RDE-position. This well-established procedure has been proven to yield very reproducible results, especially for Pt(hkl) model systems [8], for which the total error is only determined by the reading precision. So in perchloric acid, considered as a non-specifically adsorbing acid electrolyte, a sequence for the activity of low-index single crystals of Pt(100)<Pt(111)<Pt(110) was demonstrated (Figure 3.12), with a factor of about 2-3 between the lowest and highest, depending on the applied potential and temperature. For polycrystalline samples a larger deviation of up to 20% was found for the ORR reaction rate, based on a set of more than 10 individual experiments. It was concluded that in this case the activity is determined by the relative amount of different facets on the surface formed during the preparation process, since the activity value for Pt-poly was always situated between the lowest and highest single crystal values. Other preparation procedures that have been used are for instance electrochemical annealing, polishing plus treatment in concentrated acid, or UHV sputtering. Assuming a clean transfer to the electrochemical cell, the same parameters as already discussed for flame annealing should be also applicable for these procedures, i.e. due to variations in the surface structure a precision of approximately 20% can be expected.
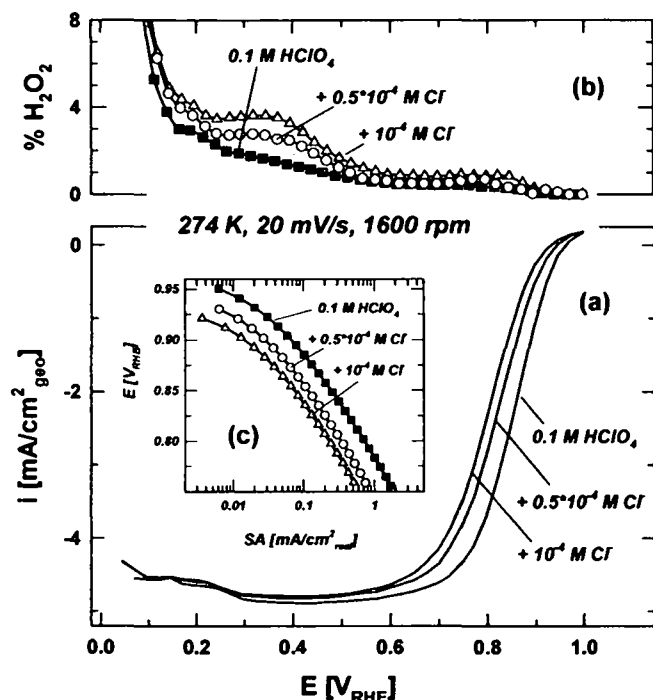
Figure 3.13: Influence of chlorides added to the electrolyte on the ORR at the disc (a) and the peroxide production at the ring (b). Measurements were performed on the 1nm catalyst at 274K, with 20mV/s and 1600rpm. The specific ORR activities are shown in insert (c). Ring potential was fixed at $1.2V_{RHE}$. For experimental details on HSAC see section 3.

Since these measurements can therefore be performed fairly precise, only a systematic error can account for the major inaccuracy of the reported data. As shown extensively in the work of Markovic et al. [8], anions from the supporting electrolyte can have a major impact on the electrocatalysis of various reactions. The most prominent example is probably the specific adsorption of SO_4^{2-}/HSO_4^- on Pt(111) and the concomitant inhibition of the ORR. But also other anions can act as spectator species and significantly block active surface sites for reactions even at very low concentrations. This is especially pronounced for the RDE study of extended surfaces, since the electrolyte volume to catalyst surface ratio is usually very large. Even though latter ratio is significantly lower for HSAC, the influence of anions can still be extraordinary, as depicted in Figure 3.13 exemplarily for 1nm particles (the experimental details for HSAC will be described in chapter 4). The polarization curve for the ORR shifts decisively to more negative potentials compared to the one in the same solution without anions added, due to the strong Pt-chloride interaction. It is noteworthy that also an increase in the peroxide current at the ring can be noticed in the potential region of the anion adsorption around 0.3V to 0.7V because the O – O bond splitting is inhibited by the adsorbed anions.

From the impact of anion "impurities" it becomes obvious that an ultra clean setup for the electrochemical cell, the use of high quality water and electrolyte solutions, and a careful sample transfer procedure is of top priority for reproducible results from electrochemical measurements. During the benchmarking process for Pt samples reported here, electrolytes prepared with triply-pyrolitically distilled water were found to behave identical compared to those prepared using Millipore® water. However, a significant difference could be detected between research grade concentrated perchloric acid solutions provided by various suppliers. So even under the most rigorous experimental conditions, an influence of anions and other impurities cannot be completely avoided. Summarizing, these varying concentration of spectator species and their poisonous impact are considered accountable for the deviations in the reported catalytic activities for the electrochemical reduction of oxygen on Pt in literature. Although average data that was obtained in the most careful manner is listed here, it is impossible to claim that this is the accurate absolute catalytic activity for Pt-poly. However, since all experiments were carried out under the same conditions, a valid comparison between the results obtained with various bulk Pt surfaces, as well as for Pt nanoparticles, which will be described later in section 4.5 is possible.

3.3. Summary

The surface structure sensitivity of the crucial electrocatalytic CO oxidation and oxygen reduction reaction has been demonstrated using Pt model systems. Thereby a novel explanation for the electrochemical response during a CO stripping as well as a CO bulk experiment was proposed. In both cases low-coordinated atoms serve as initial adsorption sites for reactive OH_{ad} on a CO pre-covered surface. The oxidation process starts from these sites and proceeds over the entire surface in dependence of the applied diffusion conditions. This was i.a. supported by the introduction of CO annealing as a preparation procedure, which can cure defects and lead to a more ideal surface. As a consequence the pre-ignition region diminishes and the ignition potential shifts to more positive values compared to a regular oxide-annealed surface, clearly indicating a lower activity for the oxidation. Similar to the CO oxidation, the adsorption of OH_{ad} also plays a decisive role for the structure sensitivity of the ORR. Instead of the promoting effect however, strongly adsorbed OH_{ad} blocks active reaction sites at relatively high potentials and thus inhibits the adsorption of oxygen and its subsequent reduction. The adsorption of OH_{ad} and other

blocking species is dependent on the surface geometry, therefore the activities of the low-index single Pt crystals are slightly different. The reason for varying absolute activity values in literature was also discussed and the important impact of anion species on the ORR pointed out.

4. Platinum High Surface Area Catalysts (HSAC)

Much effort has been invested into the research on low-temperature polymer electrolyte fuel cells over the last two decades leading to a dramatic progress of its performance. The catalyst of choice, however, still remains carbon-supported (cs) high surface area Platinum/Ruthenium on the anode and cs-HSA Platinum on the cathode side. Whereas the anodic hydrogen oxidation on Platinum is facile and well understood, the exact mechanism of the CO oxidation is still puzzling. Furthermore the strong inhibition of the cathodic ORR causes high overpotentials and therefore deteriorates the energy conversion efficiency of a PEM fuel cell to a major extent. Consequently, the development of an improved catalyst would have a major boost for the technology on the road towards its aspired commercialization.

Utilizing the results gained from the model systems in the previous chapter, the electrocatalysis on Pt HSA catalysts, i.e. "real systems", will now be investigated. Although they are generally similar in their electrochemical behavior, also significant differences can be noticed due to the distinctive electronic and geometric structure.

4.1. Application of the RRDE-Method for investigating HSAC

Since testing of highly dispersed catalysts in actual fuel cells is too intricate and time-consuming, a straightforward alternative was developed on the basis of the rotating disc electrode method by Gloaguen et al. [125]. The supported catalyst was deposited onto a glassy carbon disc and could be readily tested in an ordinary electrochemical glass cell. The initially strong Nafion film diffusion resistance, as demonstrated by Gojkovic et al. [126], due to the relatively thick catalyst layer with high Nafion content, however, complicated an extraction of kinetic data of the catalyst and made mathematical modeling necessary [127;128].

With the development of the thin-film RDE method by Schmidt et al. [129], where only a sub-micrometer thick film of Nafion is attached to a glassy carbon electrode disc, the film diffusion resistance became negligible and kinetic current densities could be collected directly using the general mass-transport correlations of the RDE [130,131]. Moreover, the significantly reduced catalyst loading expands the potential region where the kinetics can be studied, so that a comparison with ORR performance data from PEM-fuel cells can be established. The direct correlation of kinetic activities obtained applying both methods was recently verified by Gasteiger et al. [132].

First the standard experimental procedures applied in this work will be introduced in the upcoming subchapters. The sample preparation and the execution of the electrochemical as well as the in-situ FTIR measurements are described in more detail for reference. Afterwards some experimental parameters that are of great importance for the thin-film method in general and the later following results in particular, but have not been available in literature or have only been vaguely mentioned, will be considered.

4.1.1. Standard Experimental Procedures

Catalyst samples. Four different Pt high surface area catalysts were used in these studies. Three samples, supplied by TKK (Tokyo, Japan), were carbon supported Pt nanoparticles with mean diameters of 1-1.5nm, 2-3nm and 5nm, respectively (analysis by TKK). The fourth sample, consisting of a nanostructured Pt film supported on crystalline "organic whiskers" [133], was supplied by the 3M Company (St. Paul, M.N. USA). The particle size of the latter sample was roughly estimated to be about 30nm based on the charge required to oxidize a full monolayer of adsorbed CO in a CO-stripping experiment, i.e. from the estimated surface area of $8m^2/g_{Pt}$. The Pt loading of the catalyst was roughly 20% for the 1nm and 2nm catalysts, 50% and 91% for the 5nm and 30nm samples respectively. In the following, the catalysts will simply be denoted as 1, 2, 5 and 30 nm catalysts.

Electrochemical measurements. The catalyst was dispersed by ultrasonic treatment in ultrapure water and 20 µl of the suspension was pipetted onto a mirror-polished glassy carbon substrate (0.283 cm^2 geometrical area) leading to a Pt loading of $14\mu g_{Pt}/cm^2$ for the carbon supported catalysts (TKK 1, 2 and 5nm) and $42\mu g_{Pt}/cm^2$ for the 3M (30nm) sample. The dried (Ar atmosphere) catalyst film was attached to the substrate by a thin Nafion film. The thus prepared surface was

then transferred to the electrochemical cell protected by a drop of ultrapure water, immersed under potential control at 0.05 V in argon-saturated solution and cyclic voltammograms were recorded.

The electrochemical measurements were conducted in a standard three-compartment electrochemical cell identical with the one for extended surfaces (chapter 2.1.3). The reference electrode was a saturated calomel electrode (SCE) separated by an electrolytic bridge from the reference compartment. All potentials, however, are referenced to the potential of the reversible hydrogen electrode (RHE) calibrated from the hydrogen oxidation/reduction reaction measured in a rotating ring disc configuration in the same electrolyte. A Pt mesh was used as a counter electrode. The electrolyte was prepared using triply-pyrolitically distilled water and concentrated HClO$_4$ (*Aldrich, double distilled*), concentrated H$_2$SO$_4$ (*J.T.Baker*) or KOH pellets (*Aldrich, semiconductor grade*).

To record a stable cyclovoltammogram the electrodes were cycled between 0.05V and 1.0V$_{RHE}$ for at least 30 minutes in Argon saturated solution (Air Products 5N5 purity). For the oxygen reduction reaction the electrolyte was saturated with oxygen for approximately 20min and it was not recorded until more than 10 min. after the desired temperature has been reached at the thermostat. To reduce the error on the potential reading, the potential of the RHE was obtained immediately before or after the ORR at the very same temperature. The procedure for the CO oxidation requires some more attention due to its complexity. Two different procedures were used to form a saturated CO adlayer on the Pt nanoparticles. In the first procedure, denoted hereafter as "oxide-annealing", before CO is adsorbed at 0.05 V the catalyst was cycled in Ar saturated solution until a well-established cyclic voltammogram was observed. A complete CO adlayer was achieved by keeping the potential at a constant value of 0.05V for 10 min in CO-saturated solution. In the second procedure, denoted hereafter as "CO-annealing" the electrode was annealed in CO saturated solution by cycling of the electrode potential between 0.05 < E < 1.0 V for 5min, before holding at 0.05 V for 5min. This experimental approach was used because it was recently found that the "CO-annealing" pretreatment of Pt(111) facilitates the removal of surface irregularities, which after the flame annealing preparation method, are inherently present on the Pt(111) surface (see section 3.2.2). As a consequence, upon CO-annealing of the (111) surface the domain size of the p(2x2)-3CO structure, which is formed on Pt(111) at low potentials, is significantly improved [111]. On supported high surface area catalysts it was shown likewise that particles grown in CO atmosphere also contained much more extended

facets and provided fewer defect sites [134;135]. As demonstrated below, the catalytic and spectroscopic properties of high surface area catalysts pre-treated by these two methods are completely different. The stripping curves were recorded with a scan rate of 1mV/s and the upper potential limit was set to 1.0 V to ensure the complete oxidation of the CO adlayer. For the electrooxidation of CO dissolved in the electrolyte (CO bulk), before the potentiodynamic measurements were performed, the electrolyte was saturated with CO (1 atm) for 25 min while the electrode potential was held at 0.05 V.

Infrared spectroscopy. A new methodology, which has been recently described in detail in a separate paper [136], has been applied for measuring FTIR spectra on supported nanoparticles. In short, as for the electrochemical measurements the catalyst was dispersed ultrasonically in water and about 20 µl of the suspension were pipetted onto a heated (~130C) gold substrate (0.785 cm^2 geometrical area), cooled down in an argon stream and rinsed carefully with ultrapure water to remove loosely bounded catalyst particles. No further attachment to the substrate was necessary. The in-situ FTIR measurements were conducted in a Nicolet Nexus 670 spectrometer equipped with a liquid-N_2 cooled MCT detector. All IR measurements were performed in a spectroelectrochemical glass cell designed for an external reflection mode in a thin layer configuration [77]. The cell is coupled at its bottom with a CaF_2 prism beveled at 60° from the prism base. Prior to each experiment the solution was saturated with argon. The electrode was immersed into the electrolyte at a potential of 0.05 V and a CV recorded. For the CO stripping measurements recorded in the spectroelectrochemical cell, the above-described two different adsorption procedures for obtaining a saturated CO adlayer, i.e. oxide annealing and CO-annealing, were applied before pressing the sample onto the prism. Starting at 0.05V the potential was scanned with a scan rate of 1mV/s in positive direction while continually recording spectra. In order to obtain a single spectrum, four interferometer scans were coadded. The recording time was thus reduced to ca. 2.5s per spectrum. The resolution of the spectra was 4 cm^{-1} and p-polarized light was used. Absorbance spectra were calculated as the ratio $-\log(R/R_0)$ where R and R_0 are the reflectance values corresponding to the sample and reference spectra, respectively. Reference spectra were recorded either at 0.95 V or 0.05 V, where adsorbed CO (CO_{ad}) either is completely oxidized or well before the onset of CO_{ad} oxidation, respectively. The potential in the spectroelectrochemical cell was controlled by a SCE separated by a glass frit from the main compartment. All potentials, however, are referenced to the RHE calibrated from the hydrogen evolution/oxidation reaction in a special separated cell using the same electrolyte.

4.1.2. Additional parameters for thin-film RRDE measurements

The thin-film rotating-disc method, which was introduced by Schmidt et al. [129;131], has proven to be a very suitable and effective means for studying high surface area catalysts. Although the technique itself is inherently straightforward to implement, the experimental parameters have to be taken into consideration in more detail, to avoid objectionable errors in the interpretation of the obtained data. Thus it was already shown that a complete utilization of the catalyst surface and a high reproducibility of the loading could be achieved when exactly following the above mentioned electrode preparation method [129]. Furthermore it was demonstrated by Paulus et al. [130], that the effect of diffusion resistance of the thin Nafion film, which fixes the particles onto the glassy carbon, is negligible in these RDE measurements, both for the electro-oxidation of hydrogen and the ORR on Pt/Vulcan. The kinetic data for the relevant reactions can therefore be directly analyzed from the measured current densities without extensive mathematical modeling. Some more experimental parameters that are crucial for an unambiguous and reproducible determination of catalytic activities of high surface area catalysts by the thin-film method will extend those previous findings.

4.1.2.1. Determination of the Surface Area by H_{upd} and CO-stripping

The active Pt surface area of a carbon supported catalyst can be electrochemically determined by the charge it takes to either form a layer of adsorbed hydrogen in the so-called H_{upd} region in a CV, or to oxidize a pre-adsorbed monolayer of CO in a stripping (potentiodynamic) or a potential step experiment (chronoamperometric), the methods have been described previously for instance by Kinoshita et al. [137]. Traditionally the H_{upd} area has been used in most cases for high surface area catalysts due to ready access of CV's and convenience. Only when the actual CO-oxidation reaction is studied, this data are usually also used for determining the surface area [51;53]. In this work the real surface area was calculated from H_{upd} as well as CO-stripping, as an example Figure 4.1 depicts the potentiodynamic curves for three different loadings of the 1nm catalyst. Without offering a universal solution, only the respective advantages and disadvantages of both methods will be emphasized.
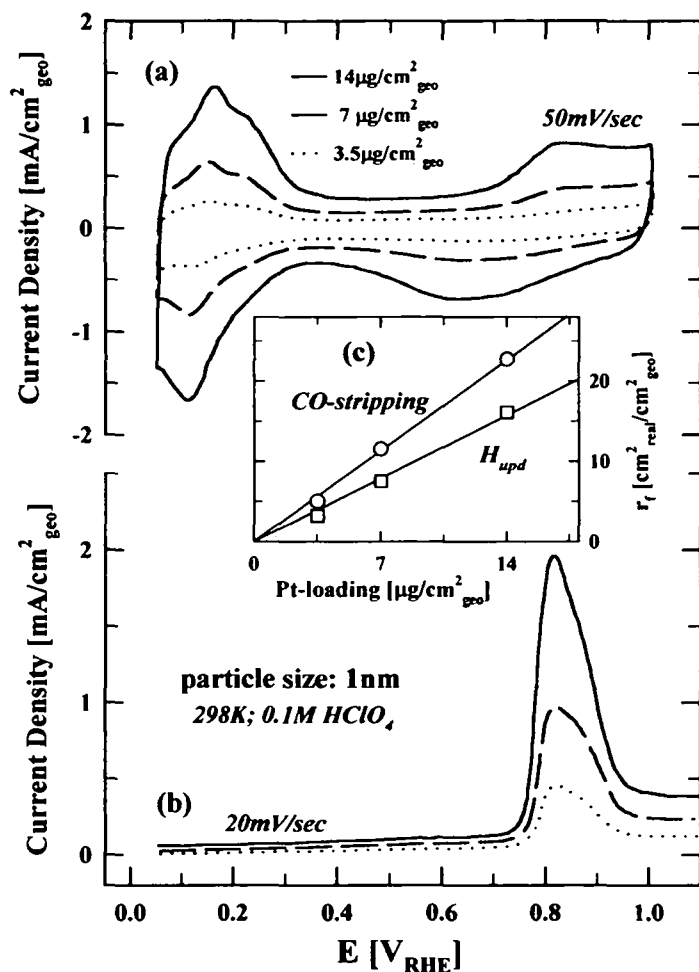
Figure 4.1: CV (a) and CO-stripping (b) for the 1nm catalyst for Pt-loadings of 14, 7 and 3.5μg/cm² respectively. Inset (c): Roughness Factor r_f calculated from (a) and (b), as a function of the Pt-loading. For further details see text.

The CV's for the catalyst show the usual shapes of a Pt electrode (see 4.3.2). The reversible H_{upd} region ranges from the negative potential limit at 0.05V to about 0.4V, where in turn the double layer region starts. The increase in anodic current above about 0.7V is attributed to the adsorption of oxygenated species that are irreversible adsorbed, as noticed by the shift of the reduction peak on the cathodic sweep to relatively negative potentials. The H_{upd} charge is estimated after a correction for the pseudocapacity seen in the double layer region, that originates mainly from the high surface carbon support. The CO-stripping curves in the lower part of Figure 4.1 were recorded in CO-free solution after adsorbing CO at 0.05V to complete coverage. The Pt-characteristic pre-ignition region between 0.3V and 0.6V is not distinct for the 1nm catalyst shown here and the CO-peak is shifted positive for about 150mV compared to polycrystalline Pt, the reason for which will be described in section 4.4.1. The CO peak area plus the area under the

CO peak in the pre-ignition region (if existent) is corrected for the background from the first following CV in the potential range between 0.4V and 1.0V to account for the adsorption of anions (OH⁻, ClO_4^-). Whereas one electron is transferred during the oxidation of adsorbed H_{upd}, the oxidation of CO to CO_2 involves two electrons and consequently the corresponding charge has to be halved. The charges (Q_H and Q_{CO}) are therefore given by

$$Q_H = \frac{j_{geo} \times E}{v} \quad \text{and} \quad Q_{CO} = \frac{j_{geo} \times E}{2 \times v} \quad (4.1)$$

with the potential E, the sweep rate v, and the current density j_{geo} relative to the geometric electrode area of $0.283 cm^2$. The roughness factor r_f of the catalyst, which denotes the ratio between the real Pt surface area A_{real} and the geometric area of the electrode A_{geo}, can then be calculated by

$$r_f = \frac{A_{real}}{A_{geo}} = \frac{Q_H \text{ or } Q_{CO}}{195 \mu C / cm^2} \quad (4.2)$$

assuming the charge density of bulk polycrystalline Pt is $195 \mu C/cm^2$ (see section 3.2). The insert in Figure 4.1 reflects the linear relationship of the roughness factor with the Pt loading for the 1nm catalyst with intercept at the origin, using both H_{upd}- and Co-stripping method. The slope of the linear approximation in this plot equals the active specific surface area in m^2/g_{Pt} of the high surface area catalyst. It is striking however, that the surface area calculated from CO is about 1.4 times higher than from H_{upd}, with 154 m^2/g_{Pt} to 112m^2/g_{Pt} respectively. This ratio is decreasing with increasing particle size, from 1.4 to approximately 1.25, 1.1 and 1.0, for 2nm, 5nm and 30nm respectively. Considering that CO/H_{upd} ratios of 0.7 to 0.9 were found on Pt-bulk crystals, which could be correlated to a CO-coverage of about 0.75 from SXS and STM studies [8], a ratio of greater than one for small particles would mean that more than one CO is bonded to a surface Pt-atom. This unusual behavior was also observed by Friedrich et al. as well as Park et al. [51,53], and was rationalized by an increasing edge-site coordination in small nanoclusters, which *could* result in higher packing densities for CO-molecules on the surface, however, does not necessarily explain a ratio higher than unity. For further investigation of this issue, the specific surface charge referred to the Pt mass obtained via CO-stripping and H_{upd} was derived for the four catalysts. Ideally, if the

amount of molecules per surface site adsorbed at saturation coverage is independent of the particle size, this magnitude should be direct proportional to the dispersion of the particles, the ratio between the atoms at the surface and the total number of atoms of the cluster. Assuming ideal octahedral cluster [138], as appropriate for fcc metals, the particle size dependent dispersion, and hence the surface charge per Pt mass, can be modeled and compared to the experimentally obtained values (Figure 4.2).
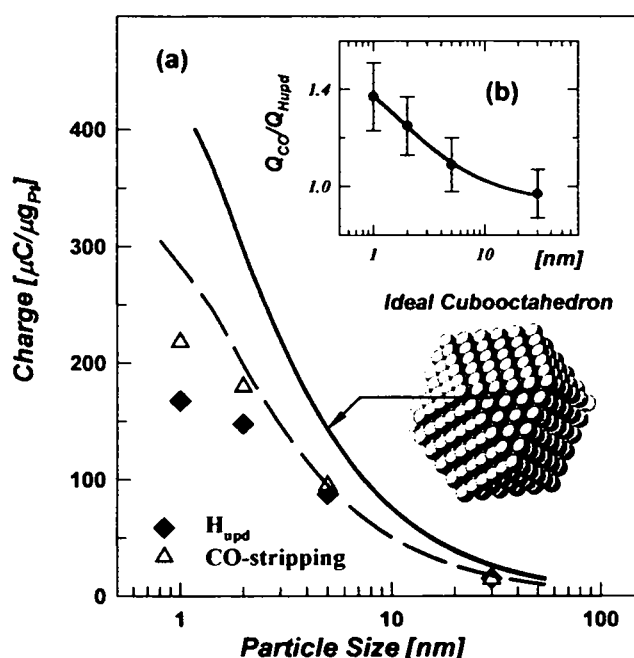
Figure 4.2: Charge per microgram Platinum as estimated from CO-stripping and H_{upd} versus the particle size. The solid line corresponds to a model for clusters consisting of ideal cubo-octahedrons, the dashed curve equals 2/3 of the model curve. 100% dispersion would be equivalent to $495\mu C/\mu g_{Pt}$. inset: ratio of the active surface area as determined by CO-stripping and H_{upd} versus the particle size in nm.

It can be clearly seen that the datapoints lie well below the theoretical estimation for one monolayer, from which can be concluded that the saturation coverage with H_{upd} and especially CO never exceeds unity. Note that real catalyst cluster with defects would exhibit a larger dispersion compared to the calculated ideal model case, so that the former assumption still holds goods. Interestingly, a curve corresponding to 2/3 of the model can be drawn with good agreement over the data from CO-stripping, with some variation for the smallest particle size. This correction is introduced to account for the fact that these particles are linked to the carbon support, and therefore not all the surface sites participate in electrochemical reactions. For smaller particles a higher fraction of the surface atoms is expected to bond to the support and be inactive for H_{upd} and CO adsorption, which would explain the lower measured surface charge to a certain extent.

In order to clarify the discrepancy between the findings obtained with the different methods, the systematic errors for the two different modes of determining the charges should be analyzed in more detail. On the one hand the integration of the CO-peak and the background subtraction for that purpose is fairly straightforward. The major uncertainty thereby is certainly the unaccounted anion adsorption in the H_{upd}-region that is neglected when the lower correction limit is set at ~0.4V. Assuming that the CO saturation coverage does not change substantially in the range of investigated particle sizes [51], the error of the calculated surface area will not exceed 10%, which complies with the results of several sets of measurements conducted in this work. On the contrary, the determination of the surface area via the H_{upd}-charge, by subtracting the capacitance of the double layer from the charge in the H_{upd} region as a background correction [137], is not quite as unpretentious as with CO-stripping, and is consequently afflicted with a larger error. A slight shift in the adsorption in the CV's to more negative potentials for smaller particles was found due to a negative shift in the potential of zero charge (pztc) [139]. However, the integration limit cannot be set to more negative potentials for smaller particles, because noticeable H_2 evolution already starts at about 0.05V positive of the RHE at the low H_2-partial pressure in Ar-purged solution and superposes the H_{upd}-charge. So as a compromise the integral intervals are set constant for particles of different sizes (0.05V- ~0.4V), well aware of the fact that the surface coverage with H_{upd} at 0.05V decreases with the particle size. Since however the charge in the integrated region is generally related to a full monolayer of H_{upd}, the specific surface area for small particles will be relatively underestimated. This could explain the variation in the CO/H_{upd} ratio with particle size as shown in the insert of Figure 4.2 and in particular a ratio greater than unity for smaller particles. Another shortcoming of the method is that it is not clear at all to this point whether the charge is related to the adsorption/desorption of H_{upd} only or actually quite the opposite assumption is reasonable. For instance Markovic et al. [8] have shown that anion species can be adsorbed in the H_{upd} region, thereby tampering the charge integration. The significance of this fact and especially its implication on catalyst particles of different sizes is widely unknown, which enhances the uncertainty of the surface area determination by H_{upd}.

Summarizing, both methods of determining the surface area of Pt electrodes are considered equally beneficial and important, but one should always be aware of the peculiarities of either approach. Due to the discussion above, data from CO-stripping will be used as a standard for the high surface area catalysts, however, without completely neglecting H_{upd}.

4.1.2.2. From geometric current density to specific current density

The kinetic properties of various model systems in section 3 have been established using the RDE, where the geometric area A_{geo} is considered equivalent to the real surface area A_{real} of the electrode. The latter fact has a special implication for the calculation of the intrinsic activity of the catalyst, which was not previously mentioned in the available literature. Namely, while the kinetic current i_k of a certain catalytic reaction depends on the active sites on the catalyst and therefore on the real surface area, the diffusion limited current i_d is a geometric property of the RDE setup. But since A_{geo} equals A_{real} in a first approximation, the well-known Koutecky-Levich equation can easily be modified to (3.1), using current densities instead of absolute currents. The specific current density j_k can thus be simply obtained from the measured current density j by a correction for the diffusion limited current density j_d.

However, for a high surface area catalyst deposited on the disc, for which A_{real} is different from A_{geo}, the equation (3.1) cannot be applied anymore. This has led to a lot of confusing remarks about catalytic activities when analyzing the reaction rate of reactions on carbon-supported catalysts measured with RDE. The origin of the looseness is demonstrated in Figure 4.3, where the ORR-polarization curves for bulk-polycrystalline Pt and the 1nm-catalyst on glassy carbon with two different Pt-loadings are compared to each other.
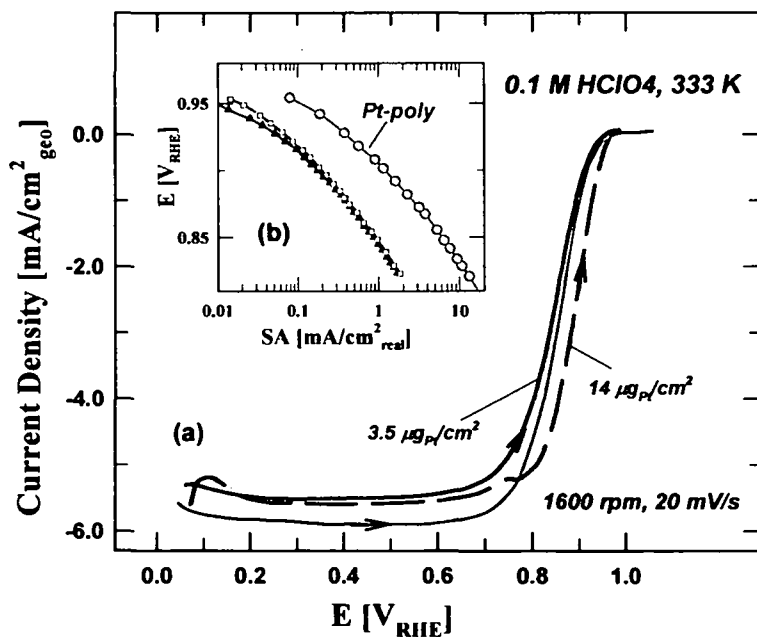

Figure 4.3: ORR-polarization (a) curves for Pt-poly and the 1nm catalyst with two different Pt-loadings in 0.1M HClO4. The temperature is 333K, sweep rate 20mV/sec and the rotation rate 1600RPM. Only the anodic sweep is displayed for all samples. Thereof estimated specific activities are presented in a Tafel-plot (b).

Since the geometric area of the bulk Pt equals the one of the glassy carbon, it is expected that the diffusion limited current density for all three samples should be the same and close to the theoretical value of $5.8mA/cm^2$ at 333K. The minor deviations seen in Figure 4.3 for the supported catalyst of less than 10% can be explained by the high pseudocapacity of the carbon support in the double layer region, which is noticeable in the ORR at the applied scan rate of 20mV/sec. However, in the region where kinetic data can be extracted, i.e. where $j < 0.8 * j_d$, all three polarization curves deviate significantly from each other. Namely, the 1nm catalyst shows a higher geometric current density compared to Pt-poly as well as a lower one, depending on the Pt-loading. If this would be diffusion corrected using (3.1) and depicted in a Tafel-plot, the same meaningless relationship for "activity" would be visible. It is therefore obvious that for RRDE studies of high surface area catalysts equation (3.1) has to be extended to account for the fact that $A_{real} \neq A_{geo}$, in order to obtain comparable catalytic properties:

$$j_k = \frac{i_k}{A_{real}} = \frac{i_d \times i}{i_d - i} \times \frac{1}{A_{real}} = \frac{j_d \times j}{j_d - j} \times \frac{A_{geo}}{A_{real}} = \frac{j_d \times j}{j_d - j} \times \frac{1}{r_f} \qquad (4.3)$$

The introduction of the roughness factor r_f of a catalyst, as defined in equation (4.3), enables the calculation of specific catalytic properties depending on the real surface area based on the correction for purely geometric diffusion limitations.

The Tafel-plot in the insert of Figure 4.3 shows the potential as a function of the specific activity SA calculated in the above-described fashion. The 1nm catalyst with the higher loading is also corrected for the 4 times larger roughness compared to the $3.5\mu g_{Pt}/cm_2$ sample, and consequently both exhibit the same catalytic activity in the kinetic region. Thus estimated specific activity is therefore the correct measure for the intrinsic catalytic activity of a high surface area catalyst in a thin film experiment, as well as for any other catalyst. Assuming a roughness factor of 1 for bulk Pt-poly, a valid comparison can now be made between these electrodes of such different structures. Moreover, catalytic activities that are obtained with practical systems, as for instance in fuel cells [132], can be linked to measurements on model systems in RRDE using the described approach.

In this context it should be further emphasized that the mass activity of a catalyst is only a arbitrary dimension unit derived from the specific activity, and is not an intrinsic property of the catalyst itself. It can be calculated from the SA using the Pt-loading per geometric area L_{Pt}:

$$j_{mass} = j_k \times \frac{r_f}{L_{Pt}}$$ (4.4)

Although the mass activity is without a doubt of major importance in practice, fundamentally the specific activity is the decisive and characteristic feature of a catalyst, especially when determining activities of such extraordinary structures as thin films or also bulk crystals.

4.1.2.3. The Pt- loading for thin-film RRDE-studies

As already shown in the previous studies on single crystals and Pt-poly (see section 3.2), the region in which kinetic information for the ORR is accessible through RRDE-measurements is limited. As a consequence, cs-HSAC should ideally be active in the same potential region to obtain comparable results. The behavior can be adjusted by the Pt-loading, which is shown in Figure 4.4 for the 30nm catalyst:
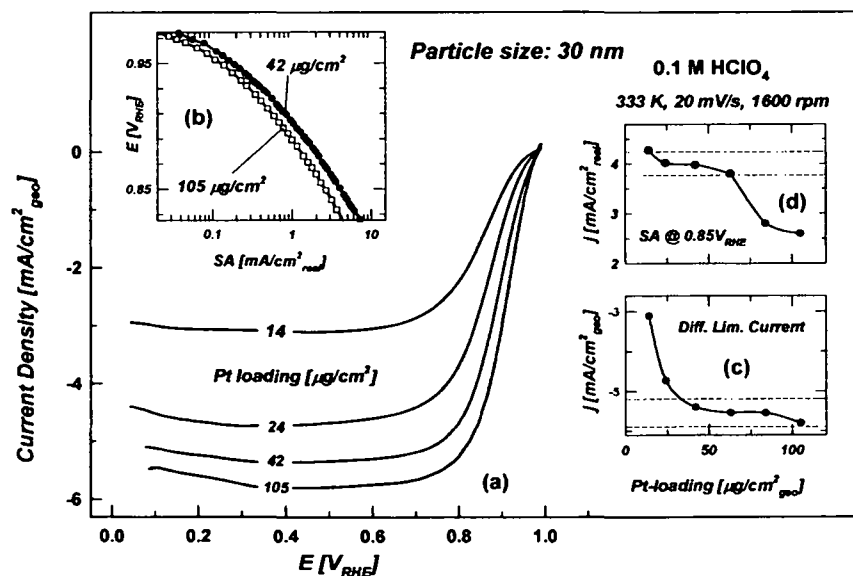

Figure 4.4: ORR-polarization curves of the 30nm catalyst for different Pt-loadings (a). Again only the anodic sweep is depicted. Thereof estimated specific activities are exemplarily shown for two loadings in (b). Inset: dependence of the diffusion-limited current density (c) and of the specific activity at 0.85V (d) from the Pt-loading.

One effect of the preparation procedure is reflected in the ORR-polarization curves in Figure 4.4 (a) and the insert (c). When going from high Pt-loading to lower loading, i.e. $105\mu g_{Pt}/cm^2_{geo}$ to $14\mu g_{Pt}/cm^2_{geo}$ for the 30nm catalyst, the diffusion limited current first remains constant around $5.7mA/cm^2_{geo}$, but drops significantly once the loading is decreased below $42\mu g_{Pt}/cm^2_{geo}$. This reason for this is that the low amount of supported catalyst is not capable anymore of spreading completely over the whole surface of the glassy carbon and therefore uncovered, inactive areas remain. This is especially emphasized in the case of the 30nm catalyst because of its low specific surface area of about $8m^2/g$ but less pronounced for the other 3 catalysts with surface areas larger than $60m^2/g$, where Pt-loadings of even $3.5\mu g_{Pt}/cm^2_{geo}$ still display correct diffusion limited currents. Analyzing the samples where i_d deviates from the theoretical value demands special attention, since the geometric area A_{geo} on which active catalyst is deposited is reduced to A_{geo}^*, resulting in a change of the roughness factor r_f^*.

$$j_k = \frac{j_d \times j}{j_d - j} \times \frac{1}{r_f} \times \frac{A_{geo}^*}{A_{geo}} = \frac{j_d \times j}{j_d - j} \times \frac{1}{r_f^*} \qquad (4.5)$$

Although the glassy carbon disc is not completely covered by Pt, the hydrodynamic solution for the RRDE remains valid, and the specific activity calculated with applying this correction for r_f^* results in overlapping graphs in the Tafel-plot in Figure 4.4b, where for clarity only the $42\mu g_{Pt}/cm^2_{geo}$ is shown. To avoid confusion, however, in general the catalyst loading should be adjusted so that the theoretical diffusion limit is attained.

For samples with higher Pt-loading deviations of the specific activities in the Tafel-plot arise, due to two different problems. Firstly, the activity becomes so predominant that the kinetic region decreases rapidly and the diffusion limit is reached at a much lower overpotential [129]. This is not only limiting the accessible potential region, but also the error due to the potential reading in the steep part of the polarization curve increases. In addition, for catalyst films thicker than $0.1\mu m$ the assumed, characteristic mass-transfer equations of the RRDE are not valid any more [127;128]. Unknown parameters, such as the agglomerate structure, particle contact and diffusivities in ionomer films, start to influence specific activity and therefore introduce a large uncertainty into the results of the measurements, as seen in Figure 4.4d.

The dependence of thin-film RRDE measurements on the catalyst loading has here been demonstrated with the ORR on the 30nm catalyst as an example. As illustrated by the various sources of errors that can occur, the amount of catalyst applied in similar types of experiments must always be considered very carefully. In this case it was found that ideally a Pt-loading of $42\mu g_{Pt}/cm^2_{geo}$ should be applied for the 30nm sample, which is right in between the zones of the previously mentioned issues. Similar experiments with the other three samples, i.e. 1, 2 and 5nm, yielded a common, optimal loading of about $14\mu g_{Pt}/cm^2_{geo}$, which will be further used in this work.

4.2. Surface characterization by TEM

Low magnification TEM- images of the Pt catalysts supported on carbon and on crystalline organic whiskers are summarized in Figure 4.5 parts a-c, and in Figure 4.5d, respectively.
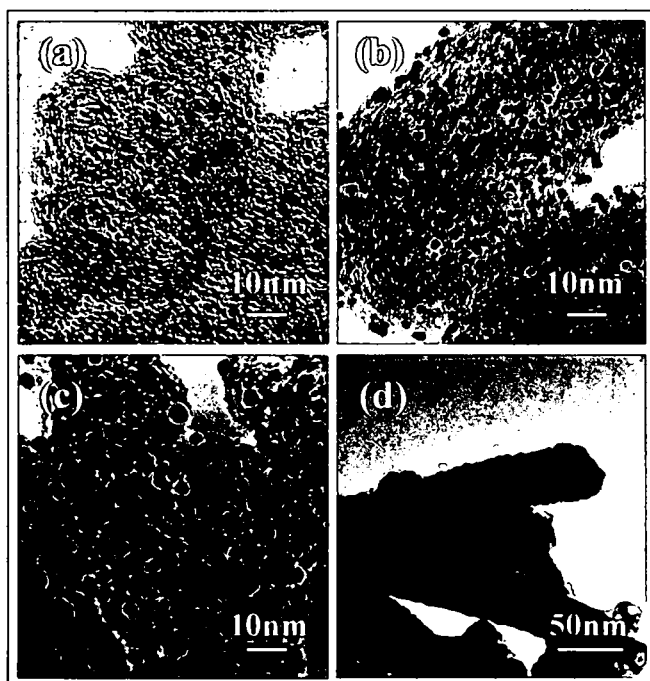

Figure 4.5: Transmission Electron Microscopy images of the four catalysts studied. In the left top corner is the 1nm (a), right top the 2nm (b), left bottom the 5nm (c) catalysts all by TKK. The right bottom picture shows the 30nm catalyst (d) supplied by 3M.

The images of the carbon-supported catalysts illustrate that the distribution of metal particles on the carbon support is rather uniform. Histograms of the particle size distribution (not shown), which included analysis of several different regions of the catalysts, established that the average particle size of Pt supported on carbon is ca. 1, 2 and 5nm respectively. This was also in very good agreement with the particle size calculated from electrochemical measurements, based on the charge required to oxidize a monolayer of adsorbed CO in a CO-stripping experiment. In contrary to the carbon-supported catalysts, the organic whiskers support is completely covered by Pt [133] (91% Pt content), and the establishment of a "particle size" from the TEM images was not possible. However, an estimation of the active surface area to approximately $8m^2/g_{Pt}$ was possible by using the CO-stripping charge, which would be equivalent with particles of about 30nm on a carbon support.
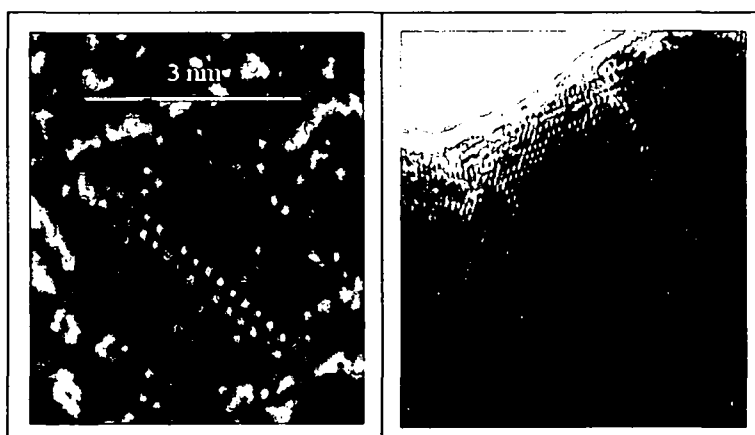
Figure 4.6: HR-TEM image of a carbon supported Pt nanoparticles (left) and the nanostructured Pt film supported on organic whiskers (right)

The analysis of images taken with higher resolution Figure 4.6 clearly indicates that the Pt crystallites are in general *not* perfect cubo-octahedrons and that the particles provide a variety of low-coordination sites for adsorption and catalysis that differ from the surface processes on regular facets. Although the basic shape of particles is cubo-octahedral, the faces of the crystals are found to be quite "rough" and "rounded", which is in good agreement with the findings published by Sattler and Ross [40]. The smallest particles still show mostly regular facets and uniform edge-corner sites, as would be expected from perfect cubo-octahedrons. However, for large particles, i.e. 30nm in Figure 4.6b, the presence of such irregular sites and steps, grain boundaries and occasionally twinned particles becomes quite obvious. From the TEM analysis it

appears that irregular surfaces of nanoparticles are the rule rather than the exception and that the relative amount of those defects increases with particle size. Consequently this may play an important role in the observed particle size effect on the oxidation of adsorbed CO molecules, as will be demonstrated in section 4.4.

4.3. Particle Size Effect considerations

As already mentioned in the introduction, the particle size effect, i.e. the variation of the reaction rate or selectivity with the characteristic dimension of metallic clusters at the electrified solid-liquid interface, has puzzled scientists for decades. One of the reasons is that no simple ideal structure can necessarily model all the aspects of nanoparticle catalysts, in particular in the identical configuration as they are used in electrolytic cells. The most prevailing strategy to predict what the particle size effect might be, is probably relating the surface characteristics of particles to well-defined single crystals. Thus, if the equilibrium shape of a nanoparticles is a cubo-octahedral structure, as is the case for the fcc Pt, a reasonable model based on (111) and (100) facets bounded by edge atom rows that are like the top-most rows in the (110) surface [140] should enable a prediction of the behavior of real catalysts. Although this approach did provide some new insight into the relationship between the structure sensitivity [35;100;114;141] and the particle size effect [50;55;142], in many cases this strategy suffers from significant weaknesses. Probably the most convincing examples that the catalytic activities observed on single crystal surfaces cannot be used as one-to-one models for *real* nanoparticles have been the oxidative removal of saturated CO adlayers on Pt nanoparticles in CO-free acid electrolytes on the one hand, but also the independence of the particle size effect for the ORR from the electrolyte on the other (see chapter 4.5). In particular, it has been found for the CO-oxidation that, although more oxophillic, smaller particles are less active than larger particles. It has been proposed that the reason for this phenomenon is a stronger bonding of CO to the surface of smaller particles and a concomitant decrease in CO diffusion [42;51;55], which will be closer investigated in section 4.4 using a different approach. Regarding the ORR the model would also predict different particle size effects when comparing results from different electrolytes, since the order of reactivity of single crystals varies decisively from e.g. perchloric to sulfuric acid (see chapter 3.2.3). As a consequence smaller particles with less extended (111) facets would be expected to be more active in sulfuric acid than

larger ones, however, the same trends in different electrolytes are obvious from the experiments presented in chapter 4.5.

In the scope of this chapter a novel approach to the issue of the particle size effect will be described, by introducing the results from the measurements of the potential of zero total charge by the CO displacement method, which corresponds to the workfunction of a material surface at the solid-liquid interface.

4.3.1. The potential of zero charge (pzc)

Frumkin and Petrii [143] first introduced the fundamental definitions describing the important influence of adsorption processes at the metal-electrolyte interface on the pzc, i.e. the potential of zero free charge (pzfc) and the potential of zero total charge (pztc). A direct relationship exists between the pzfc of an electrode, the point where the truly free, electronic excess charge density on the metal surface equals zero, and its work function in UHV [144;145]. However, specific adsorption in electrolyte solution alters this potential, so that the only experimentally accessible parameter is the pztc, the point at which the free, electronic excess charge density plus the charge density transferred during adsorption processes equals zero. As a consequence, the measured pztc's are not absolute values for electrode surfaces and cannot be compared between different electrolytes. When obtained under the same conditions, however, a perception of the changes in surface properties of various Pt-electrodes can be gained.

Among the experimental strategies used for estimating the pztc of Pt-electrodes, the recently described CO-displacement method by Climent and co-workers [146] is probably the most elegant one. In a potential region up to about 0.5V CO is strongly and irreversibly adsorbed on Pt, consequently at a certain electrode potential CO displaces the generally weaker adsorbed anions and cations completely. Moreover no net charge is considered to pass through the interface during the adsorption of CO on the surface, thus the resulting transient charge depends solely on the relative amount of initially adsorbed species. Assuming that the charge density remaining on the metal surface can be neglected and no other reactions occur [145;147], the pztc corresponds to the potential at which a charge density curve plotted against displacement potential crosses zero. Minimizing the effort, it was shown to be sufficient for extended Pt surfaces to obtain the displaced charge only at one single potential and refer the integrated voltammetric profile to this

value [146]. For a high surface area catalyst however, the overwhelming capacity of the carbon support would tamper thus received results. Hence, the CO-displacement charge was obtained at several potentials individually, as shown exemplarily for the 30nm catalyst in Figure 4.7:
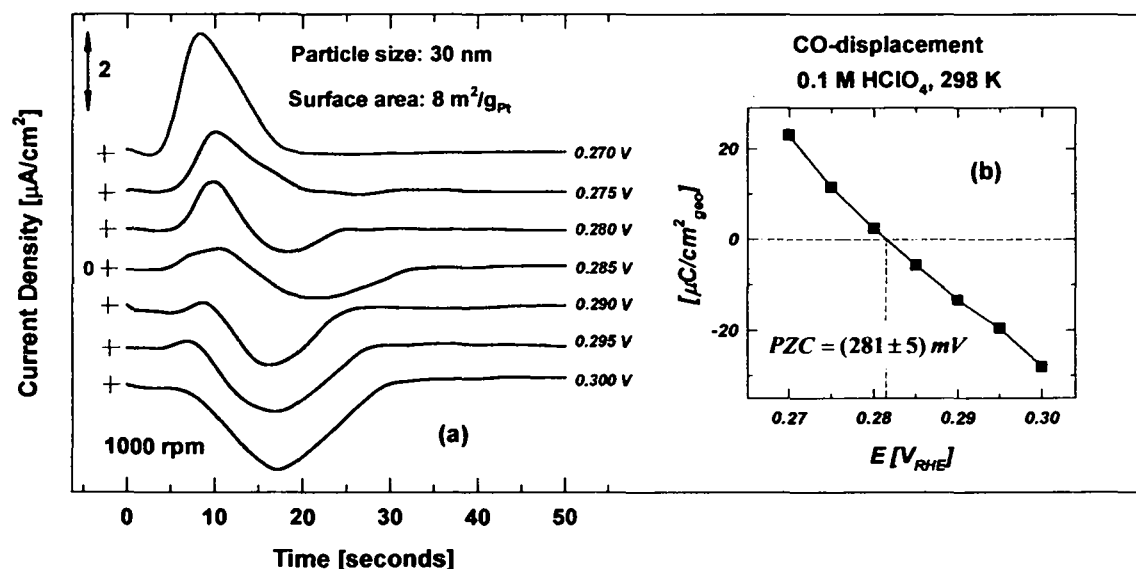
Figure 4.7: CO-displacement method for determining the pztc of carbon supported high surface area catalysts. Displacement charge versus time after introducing CO into the system (a), measured in 0.1M HClO₄ at 298K with a rotation rate of 1000rpm. The individual curves are offset from zero for clarity. Inset (b): Integrated charge under the CO-displacement peak versus the applied potential. The pztc corresponds to the potential where the regression crosses zero.

On the left hand side, the measured current density is displayed versus time, with the introduction of CO into electrolyte being at t=0. The curves are offset relative from zero so that they can easily be distinguished from each other. No current is noticed in the delay period that it takes CO to diffuse to the electrode surface. Moreover, after the displacement took place and the surface is completely covered by CO, the current drops to zero again. At potentials negative of the pztc, the measured displacement charge is positive, which means that the initially present adsorbate were mainly cations (predominantly adsorbed hydrogen from the H_{upd} region [8]). Coming closer to the pztc, also negative parts appear in the displacement curve, and at even higher potentials latter take over, indicating that adsorbed anions (OH^-, ClO_4^-) are being displaced by CO. Using a straight line between the initial delay and the end status for background subtraction, the charge density can be calculated and plotted versus the displacement potential

(insert Figure 4.7b). As already mentioned, the potential at which this curve crosses zero is considered as the pztc of the electrode in this electrolyte. For the 30nm catalyst a pztc of about 0.28V was found, an average error of roughly ±5mV is expected from the analysis of the three sets of independent measurements for all the high surface area catalysts. The results for the other three catalysts are summarized in Figure 4.8, where they are plotted against the inverse of the particle size. The pztc drops linearly from approximately 0.28V for the 30nm particles to 0.245V for the 1nm catalyst. This trend is in accordance with studies on stepped Pt single crystal surfaces, where increasing the step density leads to a decrease in the pztc, although the effect is slightly greater on latter samples [148;149]. It is noteworthy, that a polycrystalline Pt sample exhibited a pztc of ~0.285V (not shown) under the same conditions, which backs the assumption that the Pt support interaction is negligible. Interestingly, the dispersion of the catalyst, as described by the average coordination number for ideal cubo-octahedrons [138] in Figure 4.8 is also linear, confirming that the electronic (pztc) and geometric (average coordination number) factors are closely related:
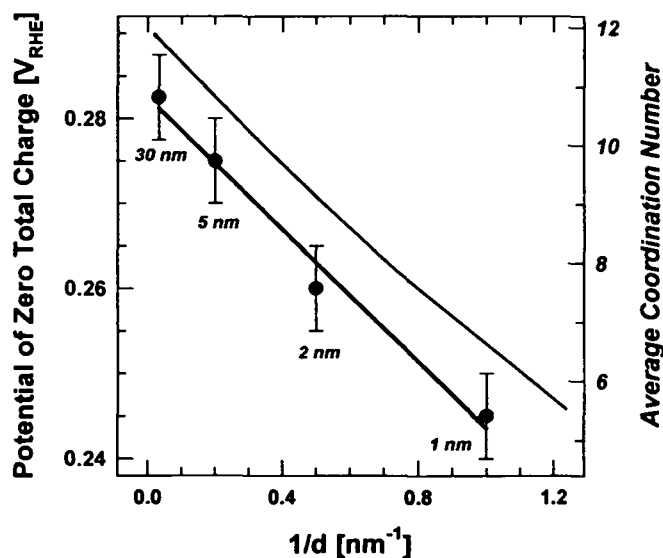
Figure 4.8: Variation of the potential of zero total charge with 1/d. The error of the displacement method is approximately 5mV. The average coordination number of atoms in an ideal cubo-octahedron is plotted against the same x-scale.

Based on this observation it appears that the *surface* electronic properties of each nanoparticle are unique, although the *bulk* electronic properties, given by the Fermi level of the material (the chemical potential μ_c), do not change decisively in this nanometer range. This effect can be understood in terms of the extent of electron "overspill" as a function of surface geometry [150]. The greater the overspill, i.e. the more atoms per unit surface area or the lower the dispersion, the larger will be the surface dipole D_s and thus the work function Φ ($\Phi = D_s - \mu_c$). As discussed by

Trasatti [144], the change in the work function can be directly correlated to the changes in the potential of zero total charge at the metal-solution interface and the variations in the pztc, in turn, will affect the electrosorption properties of the metal catalyst [151]. In line with Frumkin's and Trasatti's approach, Plieth [152] described the correlation between the shift in the likewise surface-specific redox-potential of metal clusters in a dispersed state and other electrochemical properties including the pzc in a simple phenomenological model using first order calculations. He suggested that a cathodic shift of the equilibrium potential is inversely proportional to the particle diameter d, with a simultaneous negative shift of the potential of zero charge and a decrease in the work function of the electrode surface, by

$$\Delta \varepsilon_D = \varepsilon_d - \varepsilon_b = -\frac{4\gamma \upsilon_M}{zF} \frac{1}{d}$$

(4.6)

where υ_M is the molar volume and γ is the surface tension, which is considered constant in a first order approximation (F is the Faraday constant, and z the number of electrons transferred upon the metal oxidation). Note that the surface tension is usually referred to vacuum and will most likely not be directly applicable in electrolyte, depending on the double layer properties.

In agreement with the equation (4.6), a relatively small, yet clearly discernable, negative shift in the pztc of ca. 35mV difference between the 30 nm and 1 nm Pt nanoparticles was observed, when the average coordination number drops in parallel from about 11.7 to 6. Electrosorption properties, such as the formation of H_{upd} or the adsorption of anions from the supporting electrolyte, will be strongly particle size dependent because of this shift in the pztc, which will be further examined with particular focus on the adsorption of OH_{ad}.

4.3.2. The influence of the particle size on the adsorption of oxygenated species

Although the characteristic shapes in the Cyclovoltammograms of high-surface area catalysts have been described already recently in literature, e.g. [110,132], the results for the catalysts will be briefly compared to each other to complement and support the presented work. CV's for the catalysts with a particle size of 1, 2, 5 and 30nm, respectively, and their pertaining adsorption/desorption "isotherms" (the term is used hereafter for a function of charge density versus potential) are depicted in Figure 4.9. Since a comparison of the measured voltammograms

is not quite as straightforward as for single crystals (section 3.2.1) due to the enormous differences in surface area of the different catalysts, the current signal as well as the integrated charge was normalized in terms of the specific surface area (cm^2_{real}) using the charge under the H_{upd} area (see 4.1.2.1). Furthermore the isotherms in Figure 4.9 (b) and (c) were calculated from the CV's by applying a background correction for the varying double-layer capacitance, which is mainly due to the different Pt-loadings of the catalysts and the additional support contributions.
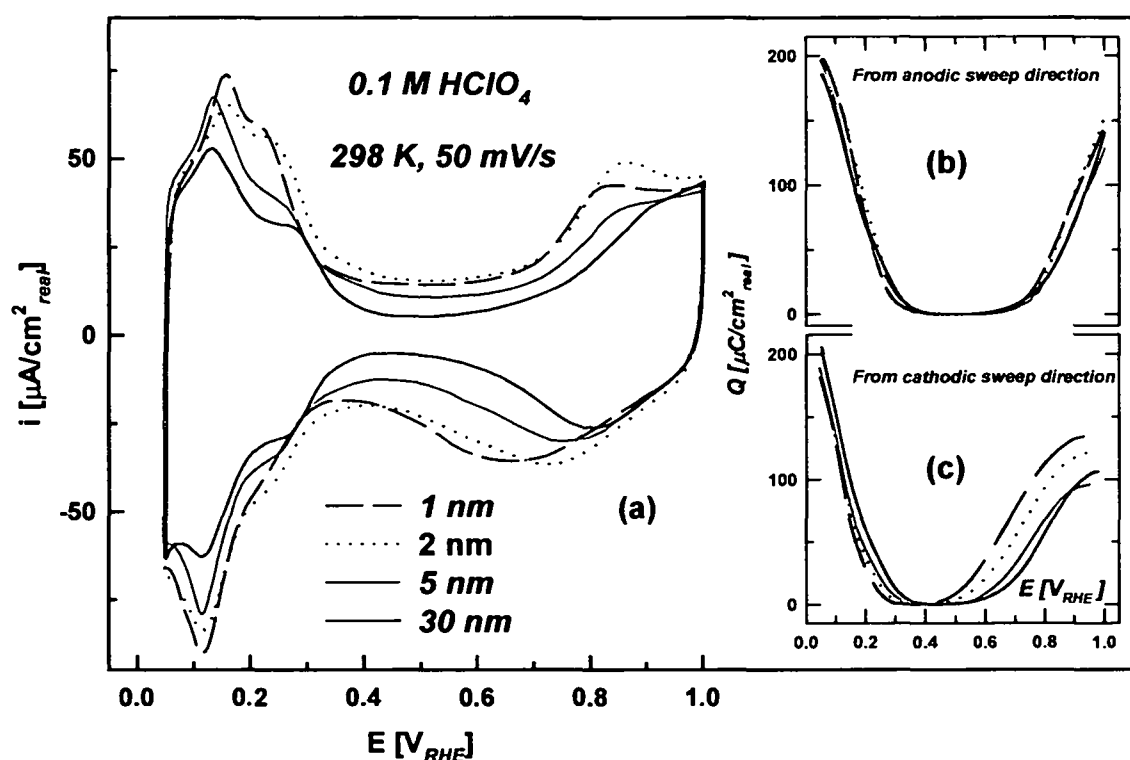
Figure 4.9: Cyclovoltammograms of the catalysts recorded in perchloric acid at room temperature with 50 mV/sec (a). The insets depict the background-corrected, integrated charge density against the potential for the anodic (b) and the cathodic sweep direction (c), respectively.

The three characteristic potential regions for Pt electrodes are well defined in Figure 4.9a for all voltammograms; the H_{upd}-region between 0.05V and 0.35V is followed by the double-layer potential region up to about 0.7V, where in turn the adsorption of oxygenated species begins. The peaks in the H_{upd}-region are generally not as distinct as for polycrystalline Pt (section 3.2.1), especially the one at about 0.25V seems to become less pronounced or merge slightly towards more negative potentials relatively with decreasing particle size (4.1.2.1). This is also observable in the isotherms on the right hand side, in particular during the cathodic sweep where the relatively

high sweep rate of 50mV/sec positively distorts the effect. When taking an average of both isotherms (not shown) to get rid of the influence of the sweep rate, the negative shift of the H_{upd}-region with decreasing particle size is still distinct, circa 25mV from 30nm to 1nm particles. Note, that the onset of hydrogen adsorption on Pt is not only determined by the Pt-H adsorption energy itself, but in addition by the Pt-anion interaction. The negative shift of the H_{upd}-region with decreasing particle size can therefore also be associated with an enhanced anion adsorption due to the changes in the electronic surface properties. The impact of the pztc becomes even more obvious for the adsorption and desorption of oxygenated species at more positive potentials. Although apparently explicit from the actual voltammograms at first glance, somehow the negative shift of the adsorption of OH_{ad} with decreasing particle size is not as distinct for the anodic sweep in the isotherms after double-layer capacity correction. However, the maximum of the oxide reduction peak in the cathodic sweep is shifted by more than 130mV towards negative potentials for 1nm particles compared to 30nm particles, with the 2nm and 5nm particles lying in between. This is also clearly reflected in the isotherm in Figure 4.9c, confirming that smaller particles are more irreversibly oxidized at lower potentials than larger ones, i.e. the oxophillicity of particles increases with decreasing particle size. This alteration of the adsorption/desorption properties of the electrode surface, induced by the change in the electronic properties with the particle size, will certainly affect the electrochemical reactions thereon.

4.4. The CO surface electrochemistry on Pt - nanoparticles

As seen in chapter 3.2.2, the adsorptive and catalytic behavior of platinum single crystals towards the CO oxidation has been extensively treated in literature. These model systems provided the opportunity to gain understanding of the activity pattern of Pt metal particles in the size range of few nanometers that ultimately can lead to the design of new catalysts. Interestingly, yet largely unexplored issues in the size-dependent physicochemical properties of Pt nanoparticles are the importance of "defect" sites, which are inherently present on Pt nanoparticles [40], and the impact of Pt oxide on the CO bulk oxidation. The latter issue is of practical importance considering that the catalyst is usually supplied by a continuous supply of CO to the surface.

4.4.1. Oxidation of a CO-monolayer

The mechanism of the oxidation of a CO monolayer on Pt nanoparticles in acid electrolytes has been extensively discussed in literature [50;55;142;153]. When CO is adsorbed at potentials close to the RHE and oxidized in the first positive sweep (recorded at relatively fast sweep rates), they found that the CO stripping peak shifts to positive potentials with decreasing the Pt particle size. Although it is misleading and fundamentally incorrect to correlate the position of the peak maximum in the CO stripping voltammetry with the catalytic activity of the Pt cluster, the authors correctly proposed that the rate of oxidative removal of CO is enhanced on larger Pt particles. Further insight into the particle size effects has been obtained from chronoamperometry, where the shape of transient currents has been simulated employing the active site model [50]. The model for perfect cubo-octahedral particle suggested restricted CO mobility on Pt nanoparticles below ca 2 nm size and a transition towards fast surface diffusion when the particle size exceeds 3 nm. Unfortunately, the model included neither the competitive adsorption of bisulfate anions (which can control the adsorption of OH_{ad} as well as the mobility of co-adsorbed CO [154]) nor the existence of irregularities on nanoparticles that may serve as the active sites for OH_{ad} adsorption, as in the case of extended single crystal surfaces (see 3.2.2). Therefore the effect of the particle size dependent number of defects in cubo-octahedral particles on the vibrational properties of CO and the CO_2 production will be demonstrated in the subsequent sections, and thus a novel interpretation for the oxidation mechanism will be proposed.

4.4.1.1. CO-stripping – cyclic voltammetry

Assuming that CO oxidation on small particles obeys the Langmuir-Hinshelwood reaction mechanism, which was previously proposed for catalysts with extended surfaces [8;22], the CO oxidation rate should increase in the same order as the oxophillicity of the Pt particles as demonstrated in chapter 4.3. In line with previous findings, however, Figure 4.10 unambiguously shows that the anodic CO stripping peak for 30 nm particles appears at lower potentials compared to the particles with a size between 1-5 nm. A cause for this behavior is still unclear, although Friedrich et al. [50;51;155] proposed that it originates from a stronger bonding of CO to the surface of smaller particles and a concomitant decrease in CO diffusion.
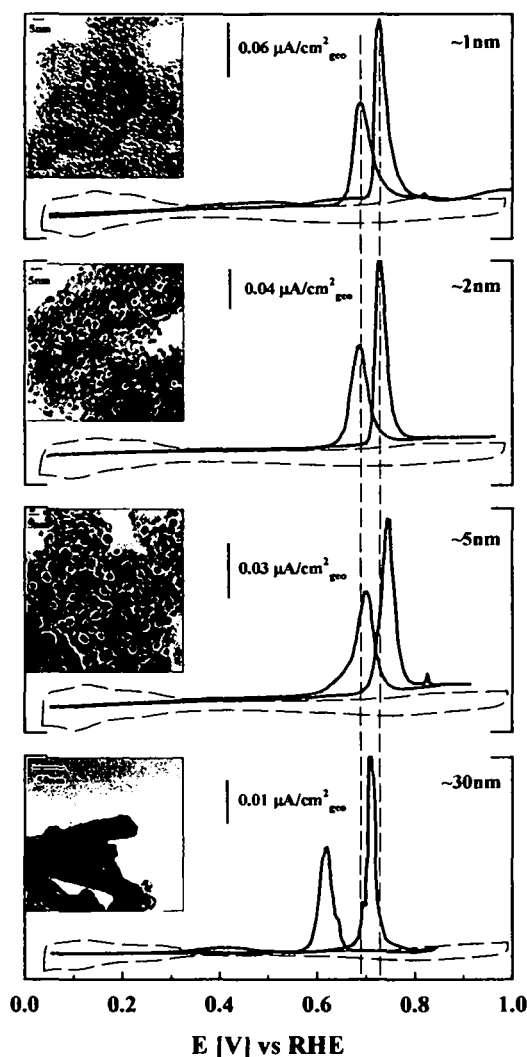
Figure 4.10: Comparison of CO stripping curves in 0.1M HClO4 solution purged after CO adsorption with argon for 30min at 0.05V; T=20C, scan rate 1mV/s; dashed gray curves show the base voltammograms of the four catalysts (50mV/s, currents divided by 50), the blue curves indicate the CO stripping curves after "oxide annealing" (method I) and the red curves after "CO annealing" (method II).

This puzzling particle size effect is further complicated by the observed difference in the CO-stripping curves recorded on "oxide-annealed" and "CO-annealed" surfaces. Figure 4.10 shows that two different potential regions can be distinguished for both surfaces: (i) the so-called pre-ignition potential region ($0.05 < E < 0.55$ V) where only small currents are observed (especially on the electrode prepared by the "CO-annealing" method) and (ii) the potential region where sharp stripping peaks are observed in the cyclic voltammogram ($E > 0.55$ V). Further examination of Figure 4.10 reveals that the CO stripping peak is shifted positive on the "CO-annealed" surfaces, consistent with the assumption that "CO-annealed" surfaces contain fewer "irregularities" than the corresponding surfaces that were not pretreated in CO saturated solution (see 3.2.2). Finally, the CO-stripping curves indicate that the most active Pt catalyst (based on the

position of the stripping peaks) is the one consisting of 30 nm particles, independent of the preparation method. In contrast to the results in ref. [142], the difference in the position of the stripping peaks for catalysts in size range of 1-5 nm is negligible (at least for the sweep rate used in this experiments), i.e. the most positive peak is the one obtained for the 5 nm particles, while those for the 1 and 2 nm particles are almost identical. Clearly, as for extended surfaces, for high surface area catalysts it is very difficult to use the CO stripping peak as a measure for the particle size effect in CO oxidation. In order to determine the onset potential for CO oxidation on the nanoparticle samples again the high sensitivity of IRAS to detect the O-C-O vibrational frequency of dissolved CO_2 will be utilized.

4.4.1.2. CO-stripping – FTIR measurements

4.4.1.2.1. Pt nanoparticle pretreated by "oxide-annealing" method

In contrast to standard infrared spectral data acquisition strategy where the potential is increased in steps of 50 or 100 mV, in this case the spectra were recorded every 2.5 s during a positive potential sweep of 1 mV/s. A representative set of spectra obtained by the latter tactics on the 5nm catalyst is summarized in Figure 4.11 (a) (CO band) and (b) (CO_2 band).
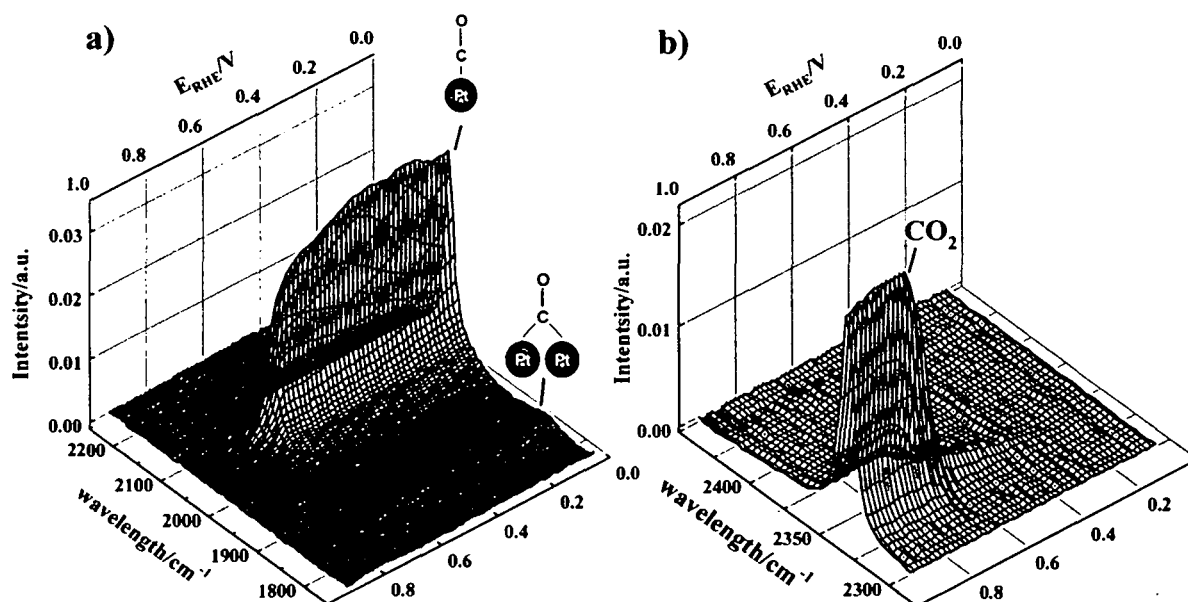
Figure 4.11: Representative "CO stripping series" of FTIR spectra (5nm sample) recorded while scanning with 1mV/s in argon saturated $HClO_4$, every fifth spectra is depicted; (a) absorption band of atop and bridge bonded CO; (b) CO_2 band.

The spectra in Figure 4.11a consist of a main band around 2060 cm^{-1}, which can be assigned to atop bonded CO on Pt [114], and a less pronounced CO band around 1880 cm^{-1}, which can be assigned to bridge bonded CO. The results obtained for the different catalyst samples are summarized in Figure 4.12 (for the sake of clarity the results of 2nm sample are not shown here; see Figure 4.14). In agreement with previous measurements [50;155;156], at 0.05 V v_{CO} redshifts as the particle size decreases, i.e. from 2062 cm^{-1} on 30nm particles to 2060, 2052 and 2049 cm^{-1} on 5, 2 and 1nm particles, respectively.
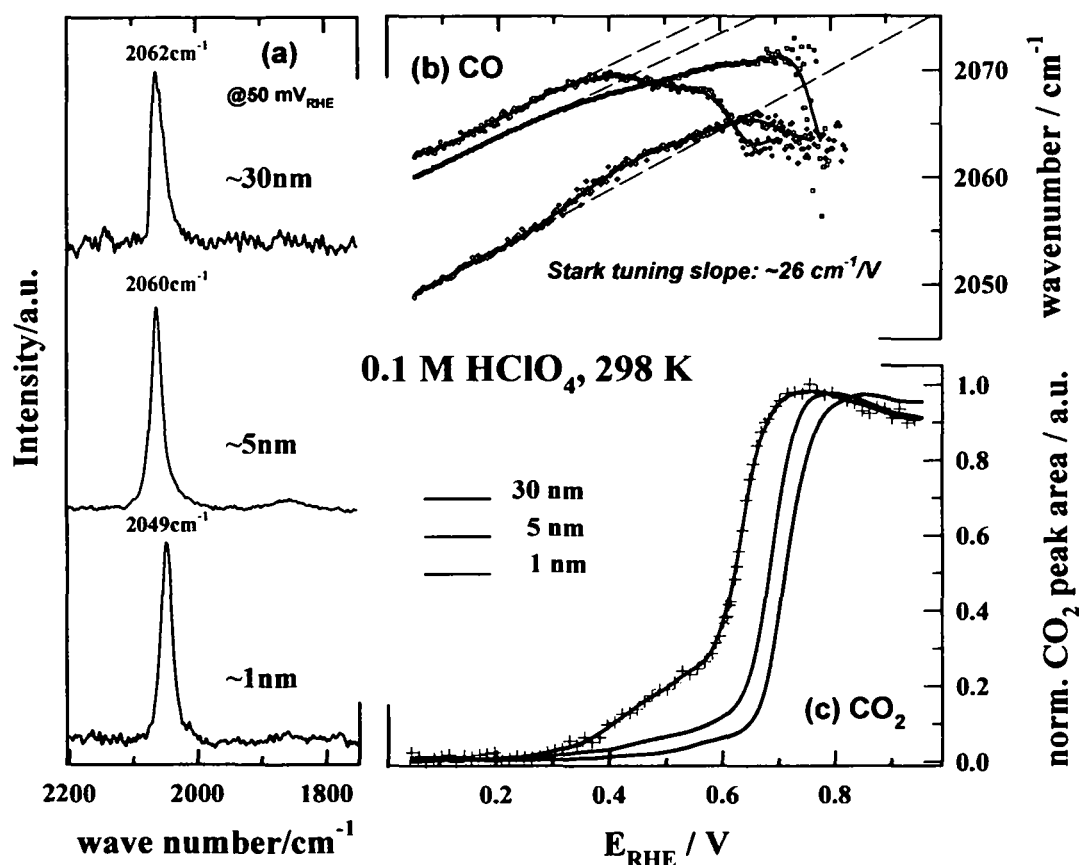
Figure 4.12: Summary of the results of a series of potential dependent CO adsorption spectra for the different nanoparticle samples; measurements were taken in Ar saturated solution after cycling in Ar saturated solution and subsequent CO adsorption at 50mV (method I); the potential was scanned with 1mV/s while continuously recording spectra; the first spectra of the respective catalysts are given in the part (a); the upper part, (b), shows the potential dependent C-O stretch frequency of atop adsorbed CO, the lower part, (c), compares the normalized peak area of CO₂ dissolved into solution (2343cm⁻¹).

The interpretation of the particle size dependent C-O stretching frequency can be offered in terms of the chemical interaction between CO and Pt (chemical shift) as well as CO-CO lateral

interactions (dipole-dipole coupling shift) [50;157;158]. In particular, the decreased vibrational frequencies on small particles have been proposed to arise due to a stronger interaction of CO with the high density of edge-corner coordination in small nanoparticles, which is in agreement with detailed theoretical density functional (DFT) calculations [64;159] of CO chemisorbed on low-coordination sites, compared to terrace Pt sites, as well as a reduced dipole-dipole interaction of the CO adlayer [53]. It should be noted, however, that DFT calculations show no general link between the metal-CO binding energy and the C-O stretching frequency [160]. Based on the measurements only it cannot be stated which effect is the predominant one, and the correlation between the C-O vibrational frequency and the detailed structure of the nanoparticles is far from being understood. In order to resolve this problem, isotopic labeling measurements are suitable [161] and are currently performed on Pt single crystals using the FTIR methodology.

Figure 4.12a also shows that the CO bands are rather symmetrical with a bandwidth (FWHM) being almost independent on the particle size (ca. 20 cm^{-1}). This observation differs from previous findings, namely that small particles exhibit a lower-wavenumber "tail" [53]. Stamenkovic et al. recently suggested that the observed "tailing" is most likely an artifact that can completely be avoided by uniformly anchoring the metal nanoparticles onto the Au substrate [136]. Furthermore, it can be clearly seen in (a) that the FWHM is independent of the particle size if the catalysts layer is uniformly dispersed on Au.

The summary of the results from the series of potential dependent CO adsorption spectra and the corresponding CO_2 production in Figure 4.12 intends to illustrate how the nanoparticle size affects the vibrational properties of CO_{ad} as well as the catalytic properties of Pt. As exemplified for the 30 nm Pt particles, three potential regions can be discerned from the v_{CO} vs. E and the I_{CO2} vs. E plots. In the potential region (0.05 < E <~0.35 V) where the CO adlayer is stable (no CO_2 production in Figure 4.12c), a linear frequency shift dv/dE (25 cm^{-1}/V) is observed, consistent with the so-called electrochemical Stark-tuning effect [75]. Between ~0.35 V and ~0.60 V, however, the Stark tuning slope dv/dE changes its sign while simultaneously a weak CO_2 band is detected in the spectra, indicating a slow but finite CO oxidation rate. In line with the previous discussion of the Pt(hkl)-CO system (section 3.2.2.1), the potential range where the CO oxidation rate is rather small is defined as the pre-ignition potential region. Finally at E ~0.60 V, the so-called ignition potential, a fast increase in I_{CO2} as well as a substantial change in dv/dE, directly indicative of rapid CO oxidation, occurs.

The spectral data of the 5 nm particles in Figure 4.12b reveal some important differences as well as some similarities with the 30 nm particles. As for larger particles, a linear positive Stark-tuning slope of ~25 cm^{-1}/V is observed over the potential region where no CO_2 is detected, 0.05 < E <~0.35 V. At E > 0.35 V the slope starts to decrease but, in contrast to the 30 nm particles, it still remains positive all the way up to 0.7 V. The small change in the Stark-tuning slope is accompanied by the appearance of a relatively weak CO_2 band. Although the onset potential for CO_2 production is the same on the 5 nm and 30 nm particles, Figure 4.12c shows that at low potentials the integrated intensities for the CO_2 band are much lower for the 5 nm particles, suggesting that the rate of CO_2 production is much smaller on the 5 nm particles than on the 30 nm particles. The confirmation that the oxidative removal of CO_{ad} on 30 nm particles is faster than on 5 nm particles is also obtained from the ignition potential region (the negative dv/dE slope and extensive production of CO_2), which is on the 5nm catalyst shifted by ca. 50 mV towards higher potentials.

For very small Pt nanoparticles (1nm and 2nm), an anomalous behavior in the v_{CO}-E frequency shift can be observed, which has not yet been reported in the literature for the case of nanoparticles. This anomalous behavior of the CO vibrational/catalytic properties is more pronounced for 1 nm than for 2 nm particles. Figure 4.12b shows that around 0.35V the Stark-tuning slope first slightly increases and then, while still remaining positive, at E > 0.55 V begins to decrease and finally at 0.7 V, where the rapid CO oxidation occurs, a negative sign in dv/dE is observed. Interestingly, the blueshift deviations in the v_{CO} frequency are accompanied by a small yet clearly discernable CO_2 production, indicating that although the surface is less covered by CO, the interaction energy of CO with the Pt particles is weaker (!). Note, that a similar blueshift in the v_{CO} frequency can be observed at the onset of CO oxidation on Pt(111) [154]. For the Pt(111)-CO system, it was suggested that the initial CO oxidation is accompanied by adsorption of anions from the supporting electrolyte. These co-adsorbed anions may lead to a compression of CO molecules, resulting in a higher local CO coverage and thus yielding blueshifted atop CO frequencies due to enhanced dipole-dipole coupling. Notice, the phenomenon of island compression is observed in segregated systems where the presence of one species causes the other species to segregate into patches in which the local density is higher than that observed when an equivalent amount of particular species is adsorbed alone see (for example ref. [162]). Extending this phenomenon to CO adsorbed on Pt nanoparticles, the surprising blueshift in the v_{CO} frequency

for 1 nm particles at $E > 0.3$ V may be a consequence of slow but continuous CO oxidation which is accompanied by anion adsorption (either ClO_4^- [163] or trace levels of Cl^- impurities [164]) and concomitant CO compression on (111) facets. Furthermore, the close similarity between the vibrational properties of CO adsorbed on Pt single crystals and very small Pt nanoparticles is in line with the TEM analysis, which showed that the surface of large particles contains undistorted (111) facets in a smaller fraction in contrast to the surface of small particles.

While the onset potential for CO oxidation is almost independent of the particle size, the rate of CO_2 production strongly depends on the particle size, i.e. 1nm $\leq$ 2nm $<$ 5nm $<<$ 30nm. Closely following the interpretation of the CO oxidation rate in the pre-ignition region on extended Pt single crystal surfaces, the next section will demonstrate that I_{CO2} is controlled by the presence of specific surface "irregularities" (see section 4.2), which serve as nucleation center for OH_{ad} adsorption.

4.4.1.2.2. Pt nanoparticles pretreated by the "CO-annealing" method
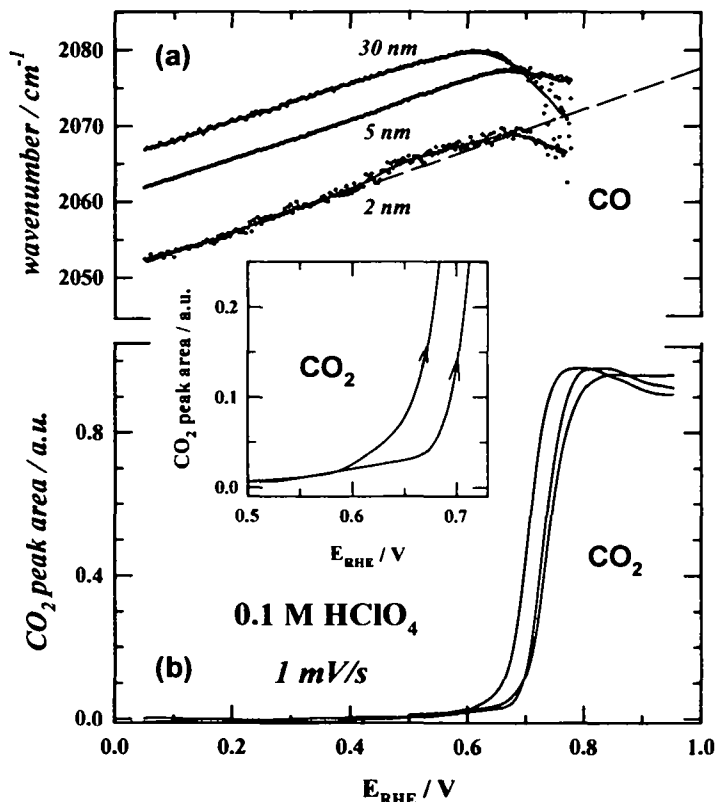

Figure 4.13: Summary of FTIR results of 2, 5 and 30 nm catalysts. In contrast to Figure 4, the CO adlayer was formed by the "CO annealing" procedure, i.e. by cycling in CO saturated solution for 5min, stopping at 0.05V and purging with Ar in order to completely remove CO from solution (method II).

For the purpose of the discussion here only the v_{CO} versus E plots for the 30, 5 and 2 nm particles are presented. As shown in Figure 4.13a and in agreement with the results in Figure 4.12, by decreasing the particle size the CO band position shifts towards lower wavenumbers, i.e. from 2067 to 2062 and 2052 cm⁻¹ for 30, 5 and 2 nm particles, respectively. As discussed in refs. [50,155] and in the previous section, the observed redshift can be rationalized by an interaction between the chemical shift (stronger CO adsorption on smaller nanoparticles) and the dipole-shift (enhanced CO-CO lateral interactions on larger particles). Further examination of Figure 4.13a shows that for 30 nm particles the "normal" Stark-tuning behavior with a slope of ~25 cm⁻¹/V is observed between 0.05 V to 0.65 V, then significant CO oxidation starts, indicated by an extensive CO_2 production (Figure 5b). For 5 nm particles a linear Stark-tuning slope of ~25 cm⁻¹/V is also clearly observed between 0.05 and 0.7 V. On both catalysts a small CO_2 production is observed at potentials as low as 0.6 V (see the insert of Figure 4.13). Intriguingly, on 2 nm particles the anomalous blueshift deviation from the "normal" Stark-tuning slope is observed over the potential range of 0.55 < E < 0.7 V. Again, the observed deviation coincides with a small yet clearly discernable CO_2 production (Figure 4.13b), confirming that the blueshift deviation is triggered by the slow oxidation of CO. The CO oxidation rate increases in the order 30 > 5 > 2 nm, if I_{CO2} would be used as a measure for the catalytic activity.

4.4.1.2.3. Effect of surface irregularities

In Figure 4.14 the IRAS data for the two different pretreatments of the nanoparticle catalysts are compared. For the 30 nm particles v_{CO} on the "CO-annealed" surface is blueshifted by ca. 5 cm⁻¹ relative to the surface pretreated by the "oxide-annealing" method. The observed blueshift would imply that the Pt-CO interaction is weaker with the "CO-annealed" than with the "oxide-annealed" nanoparticles. The CO_2 production in Figure 4.14b, however, is higher on the latter surface, suggesting that the Pt-CO adsorption energies do not control the reactivity of the Pt cluster for the oxidation of the CO adlayer.

Figure 4.14: Comparison of CO adsorption/oxidation properties obtained with different CO adsorption procedures "CO annealing" and "oxide annealing" (method I and II; for details see text); blue colors: 30nm sample, brown colors: 2nm sample. Scan rate is 1 mV/sec.
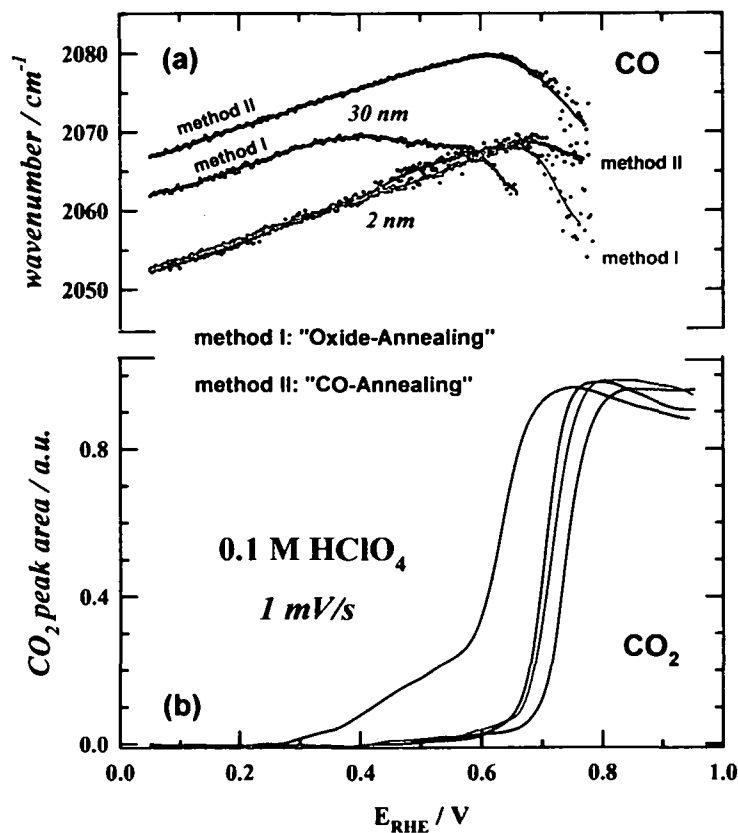
Due to the observation that surfaces containing more "irregularities" are more active, such as the "oxide annealed" 30 nm particles, the oxidation rate of a CO monolayer (CO stripping conditions) is controlled by the presence of catalytically active OH_{ad}, which is formed on those defect sites, rather than by the Pt-CO adsorption energies or the CO surface mobility. This is in agreement with the findings that on Pt single crystal surfaces the CO oxidation rate is also more influenced by the ability of the surface to dissociate water molecules and to form OH_{ad} on steps and defect sites (see 3.2.2 and [34,35;165]). Defect sites also play a role in CO "clustering" on the 30 nm nanoparticles, causing CO to decrease in local coverage on the "oxide annealed" surface relative to the "CO-annealed" surface. Consequently the higher local CO coverage on the latter surface yields the blueshifted v_{CO} frequencies due to enhanced dipole-dipole coupling, as shown in Figure 4.14a.

In this context it is also worth mentioning that over the potential range of $0.05 < E < 0.5$ V the v_{CO} frequency on the 2 nm particles (as well as on the 1 nm particles) is independent of the

number of defect sites. This observation is consistent with the analysis of the TEM images, showing that the "surface roughness" of the cubo-octahedrons increases with the particle size and, thus, the vibrational properties of CO_{ad} on smaller particles are less affected by the preparation method (see 4.2). The importance of defects is, however, observed at potentials E > 0.5 V, where a small production of CO_2 on "CO-annealed" particles is accompanied by an increase in the C-O vibrational frequency. Notice that the blueshift deviations from the "normal" Stark-tuning slope are more pronounced on the CO annealed, i.e. less irregular 2 nm particles. Most likely the microscopic effect responsible for the observed differences in the v_{CO} frequency is the same as the one proposed for the 30 nm particles, i.e. the smaller number of defects on the "CO-annealed" surface allows CO to increase in local coverage accounting for the observed blueshift in the v_{CO} frequencies due to enhanced dipole-dipole coupling. Therefore, considering that surfaces of larger particles are inherently rougher than those of smaller particles, the sequence of reactivity for CO monolayer oxidation (CO stripping) increases with growing size of the Pt nanoparticles. In accordance, the oxidative removal of CO on particles with nominally the same size is enhanced on the "oxide-annealed" surface, because "CO-annealed" surfaces contain fewer defects than "oxide-annealed" surfaces.

4.4.1.3. "CO bulk" oxidation – FTIR measurements

When analyzing the same experiment performed in CO saturated purged solution, a slightly different behavior is found in FTIR. Unfortunately, the special setup of the FTIR cell applied here (thin-layer configuration) and the impossibility to rotate the electrode prevents a comparison with kinetic data obtained from CO bulk oxidation measurements in an electrochemical RDE experiment (see chapter 4.4.2). Furthermore due to the very limited supply of CO from the tiny accessible fraction of the electrolyte and the lack of solution convection, these measurements should not be considered representative for high CO concentration conditions. Indeed, they are presented exactly for that purpose, namely to emphasize the importance of the experimental conditions on the CO oxidation. Additionally the findings are underlining the influence of defects on the reaction as described in the previous paragraph.
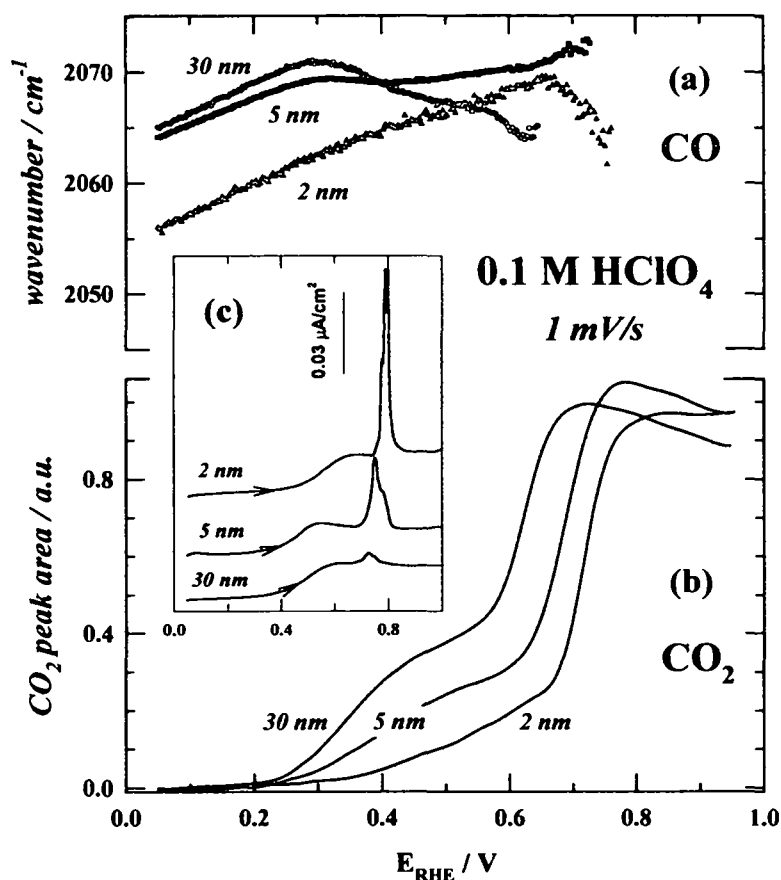
Figure 4.15: CO-adsorption spectra for different nanoparticles in a "CO-bulk" experiment (oxide-annealed electrode surface) in CO purged solution; the upper part (a) shows the potential dependent C-O stretch frequency of atop adsorbed CO, the lower part (b) compares the normalized peak area of CO_2 dissolved into the thin layer (peak position 2343cm⁻¹).

In agreement with the results presented in Figure 4.12, by decreasing the particle size the CO-band position shifts towards lower wavenumbers, i.e. from 2065 to 2064, 2056 and 2053 cm⁻¹ for 30, 5, 2 and 1nm particles, respectively. However, due to the higher partial pressure of CO in solution, the CO band position for all catalysts blueshifts by about 4-5 cm⁻¹ compared to CO-free solution. This can be rationalized by a weaker interaction of CO with the Pt-surface and an increased dipole-dipole coupling within the CO-adlayer, as a result of the higher coverage [50;114]. Initially, the Stark-tuning slope dv/dE of 25 cm⁻¹/V is identical to the value for in Ar-purged solution, however, a more pronounced redshift deviation is observed for 30 and 5nm above 0.35 V, when the oxidative removal of CO begins and the surface relaxes to the initial state. Concomitantly, the CO_2 production in the pre-ignition region is much more enhanced compared to Figure 4.12 for all catalysts. This indicates the reaction of additional CO that diffuses from the thin layer to the accessible surface sites, which are generated by the oxidation of CO_{ad} on defects.

The ignition potential for the four catalysts however, is not affected by CO in solution in the absence of forced convection and remains almost completely identical, in contrast to CO bulk oxidation. In agreement with the previous results, the rate of CO_2 production and the ignition potential depend on the relative amount of surface defects under these reaction conditions and therefore both increase with the particle size, i.e. 1nm $\leq$ 2nm $<$ 5nm $<<$ 30nm.

4.4.2. CO-bulk oxidation

As already seen for the model systems (section 3.2.2), applying RDE measurements in a CO saturated electrolyte to study the oxidative removal of CO is more suitable for practical applications than CO stripping experiments, since the catalyst is usually exposed to a continuous supply of CO to the surface. The well-defined diffusion conditions at the disc electrode [71] are also valid for the study of high surface area catalysts in a thin-film on GC, as shown by Schmidt et al. [129]. However, the CO bulk polarization curves obtained via RDE (Figure 4.12a) are not comparable with the FTIR characteristics in CO saturated solution, which is demonstrated in Figure 4.15, or in Figure 4.12 c' and c" for the 1nm catalyst. In the latter case no CO is adsorbed at a potential beyond approximately 0.8 V, on the oxide annealed as well as on the CO-annealed surface. Therefore the oxidation of CO in the thin-layer can proceed uninhibited and is complete at this potential. On the other hand, the CO bulk oxidation in a RDE is still highly impeded up to about 0.9 V, due to the continuous re-adsorption with CO from solution by the forced convection. For this reason also no correlation could be derived in the pre-ignition region, and therefore the discussion will be focused on the RDE results under high CO partial pressure conditions only.
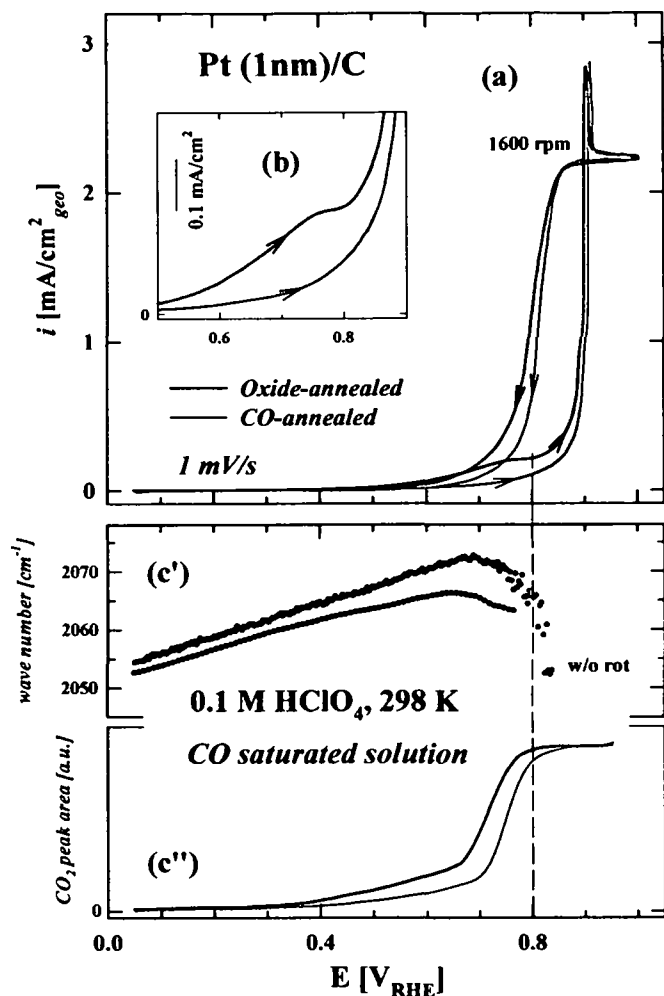
Figure 4.16: CO bulk oxidation on the 1nm catalyst (a) with a RDE at 1600 rpm in CO saturated perchloric acid electrolyte (sweep rate: 1 mV/sec, T=298 K). Curves are shown for an Oxide-annealed (black line) as well as a CO-annealed (gray line) electrode. Inset (b): Magnification of the pre-ignition region. The FTIR results for the same catalyst in CO saturated solution are depicted in (c') CO band frequency and (c") integrated CO_2 peak area, analogous to Figure 4.15.

Representative potentiodynamic curves for the CO bulk oxidation on carbon supported 1nm Pt catalyst are depicted in Figure 4.12a. Although the features of the polarization curves differ significantly from the CO-stripping ones discussed earlier, in the initial range one similarity can be found. When sweeping positive from the CO-adsorption potential of 0.05 V, at potentials around 0.35 V a growing current signal initiates the pre-ignition region. In analogy to CO-stripping, CO becomes oxidized on defect sites first, which act as the primary adsorption sites for the necessary OH_{ad}. Due to the fast mass transfer of CO from solution by rotating the electrode, however, the oxidation on these defects does not impact the adjacent sites as much as in CO-stripping. Continuous re-adsorption of CO on the surface sites shields the electrode from adsorbing additional reactive OH_{ad} on terrace sites, which leads to a decisive anodic shift of the ignition

potential to about 0.9 V. No clear trend for the CO oxidation depending on the particle size could be found in the pre-ignition region in this type of experiment. Even within two series of measurements of the same sample, variations of up to 50% in the peak current were observed. Moreover, the polarization curves reflect moderate changes of consecutive sweeps, especially in the pre-ignition region, due to restructuring of the surface by CO-annealing (see section 4.4.1). In order to avoid the influence of these surface irregularities on the reaction and to obtain reproducible results, the CO-annealing effect for the electrode surface was simply utilized as a preparation method, i.e. cycling the electrode in CO-saturated solution for 5 minutes. In contrast to oxide-annealing, the thus achieved CO-annealed surface exhibits fewer defect sites and is therefore almost completely inactive for OH_{ad} adsorption before the ignition potential, as it was previously described for CO-stripping. As a result the CO oxidation in the pre-ignition region vanishes, which can be seen in the inset (b) of Figure 4.12 for instance for the 1nm catalyst.

It is surprising that the CO-annealing has only little influence on the ignition potential itself, viz. a slight positive shift of about 20mV is observed for all nanocatalysts compared to an oxide-annealed surface. Obviously surface defects as OH_{ad}-adsorption sites do not play a major role any more. At the ignition potential the current signal rises abruptly to the diffusion-controlled limit, for a short period even beyond it. This can be ascribed to the oxidative removal of the remainder of the initially adsorbed CO in addition to the diffusion-limited oxidation of CO from solution, i.e. CO bulk is superimposed by a CO-stripping curve. In the region of the diffusion-limited CO oxidation above 0.9 V, the Pt surface is then mainly covered with oxygenated species and every arriving CO molecule will be immediately oxidized. At much higher potentials E>1.1 V these active OH_{ad} adsorbants form stronger bonds with the Pt surface sites, which in turn becomes inactive for the CO oxidation (see Figure 4.19).
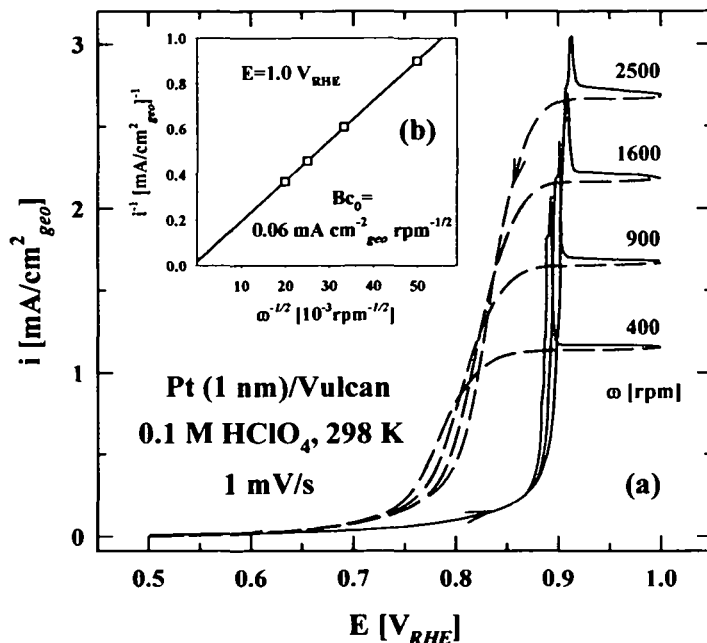
Figure 4.17: CO-bulk oxidation on the CO annealed 1nm catalyst at rotation rates of 400, 900, 1600 and 2500 rpm (a). The measurements were conducted in 0.1M perchloric acid at 298K, with a sweep rate of 1mV/sec. The according Levich-Koutecky plot for a potential in the diffusion-limited region is displayed in (b).

In Figure 4.17 the CO bulk oxidation is presented exemplarily on 1nm particles for various rotation rates. No significant current was detected in the so-called preignition potential region up to about 0.8V, due to the pretreatment of the catalyst by CO-annealing [110]. Around 0.9V, the ignition potential, the rate of the CO oxidation suddenly rises unrestrained to the diffusion-limited value and exceeds it, subsequently reaches a maximum and then declines back again to the diffusion limit for all rotation rates. Initially adsorbed CO is being stripped from the electrode surface, thus generating sites for OH_{ad} to adsorb and react with either still strongly adsorbed, adjacent CO on the surface but also with CO from solution. As a consequence the diffusion limit is surpassed for a short period until all initially site-blocking CO is oxidized. Notice, that the stripping peak on top of the diffusion-limited current is smaller but wider for higher rotation rates of the disc. Moreover the peak position is shifted slightly towards higher potentials, from 0.89V for 400rpm to 0.91V for 2500rpm. This can be attributed to the increased supply with CO from solution with the elevated rotation rate, which can adsorb instead of OH_{ad} to a larger extent and thereby block the active reaction sites. The same effect can be seen at the cathodic sweep at circa 0.8V, where the decline of the current signal is the fastest for 2500rpm, and at 400rpm the kinetic region is extended to the most negative potentials. Again, the re-adsorption of site-blocking CO is enhanced with increasing rotation rate, because of their relatively low concentration compared to competing OH-species from the aqueous electrolyte.

Between 0.9V and 1.0V the CO bulk oxidation proceeds at the diffusion limited rate. The magnitude of the diffusion limit is similar to the value obtained on extended surfaces (see 3.2.2.2), confirming that the diffusion resistance of the Nafion film for the applied thin-film method is negligible for this reaction (see 4.1.2). This is also confirmed by the Levich-Koutecky plot in Figure 4.17b, where all data values lie on a straight line that intercepts at $54mA/cm^2$ and has a slope of $0.057mAcm^{-2}_{geo}rpm^{-1/2}$. On the reversal of the sweep direction at 1.0V, the electrode surface is predominantly covered by oxygenated species and therefore the kinetic region extends much further to negative potentials compared to the positive sweep. Depending on the rotation rate, and thereby on the supply of CO, the current signal starts to drop between 0.8 and 0.85V and reaches zero at about 0.65 to 0.7V. At this point all adsorbed OH_{ad} has been consumed by the reaction, and the whole electrode surface is again covered by a layer of CO, completely inhibiting the adsorption of reactive oxygenated species and thereby the CO oxidation.

When the focus of attention is now brought to this reverse sweep, where initially at 1.0V the electrode surface is covered by reactive oxygenated species rather than by inhibiting CO on the positive sweep, the influence of the differences in OH_{ad} adsorption with the particle size can be extracted. This is shown in Figure 4.14 for the 1nm, 5nm and 30nm catalyst; the 2nm particles, which exactly follow the demonstrated trend in activity, were left out for better understanding.
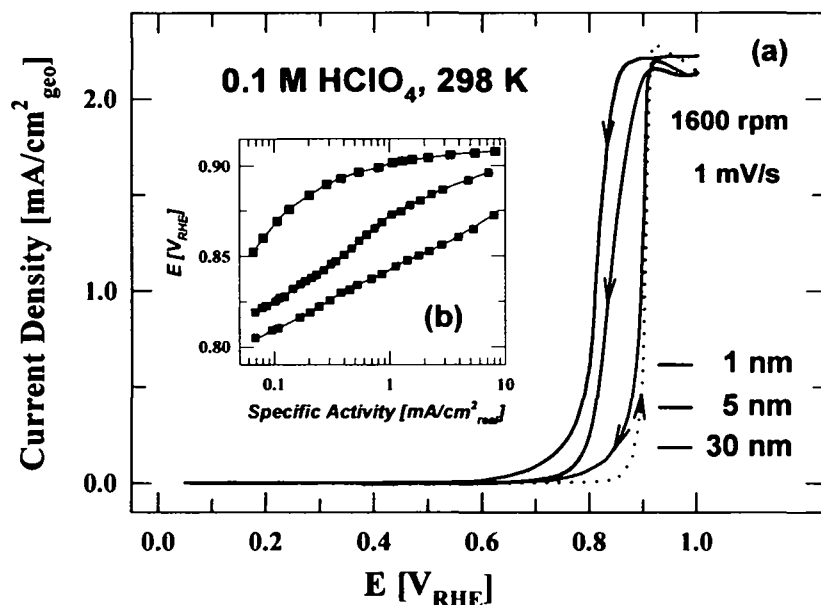
Figure 4.18: (a) Comparison of the CO bulk oxidation on the 1nm, 5nm and 30nm catalyst (the 2nm catalyst is not shown for clarity) at the negative going sweep from 1.0V where the surface is mainly covered with OH_{ad}. Only the positive sweep of the 30nm catalyst is illustrated for clarity, since the ignition potential is independent of the particle size. In the insert (b) the potential is depicted against the specific activity (Tafel plot).

It can be clearly seen from the polarization curves that the kinetic region for the CO oxidation is extended to more negative potentials for smaller particles, with 30nm revealing almost reversible behavior and becoming inactive already at the ignition potential in contrast to 1nm, which is fairly active till about 0.8-0.82V. This can also be retrieved from the Tafel-plot in the insert Figure 4.18b, where the potential is plotted against the logarithmic current density, normalized to the specific surface area of the corresponding catalyst. Except for the 1nm particles, no ideally linear Tafel relationship could be detected for the CO oxidation in the cathodic sweep over more than one order of magnitude. The reason for this could be that the defect sites, which govern the reaction on CO pre-covered surfaces (see chapter 4.4), also have an influence in the reverse sweep to a certain degree. Nevertheless, the trend in the CO bulk activity can be unambiguously determined over the whole potential region of interest, which leads to a sequence in activity of 30nm<5nm<1nm. Assuming that the Langmuir-Hinshelwood reaction mechanism for the CO oxidation reaction holds good for carbon supported Pt catalysts as it does for bulk Pt [8], then this reactivity trend is in perfect agreement with the change in oxophillicity with the particle size as shown in section 4.3.2. Namely, the smallest particles with the most negative pztc, i.e. 1nm, adsorb OH_{ad} to more negative potentials, and as a consequence are more active for the CO oxidation. On the contrary, 30nm particles with a more positive pztc are less oxophillic, therefore they become faster covered by blocking CO and are less active for the CO bulk oxidation.

Another interesting characteristic property of the CO surface electrochemistry can be seen from the anodic sweep in Figure 4.18, namely that the ignition potential for CO oxidation is identical for all CO-annealed nanocatalysts and independent of the particle size. Furthermore the ignition potential is also equivalent to the value observed on the extended surfaces of Pt(hkl) and polycrystalline Pt samples (see 3.2.2.2). This is an unexpected finding, considering the major influence of the defect sites on the one and the OH_{ad}-adsorption on the other hand. The sharp, specific increase of the current signal at the ignition potential indicates a fast transformation of the surface composition in a narrow potential range from an inactive to an active state. This effect is triggered by a direct displacement of CO_{ad} from the Pt surface by OH_{ad} from water dissociation, under these reaction conditions when no (or only few) defect sites are available and the surface is completely blocked by CO. Once the adsorption of OH_{ad} becomes more favored compared to the re-adsorption of CO, the removal of the remaining CO patches cannot be avoided and the bulk

CO oxidation reaction becomes rapid and completely self-sustained. This conclusion is further supported by the fact that the CO-stripping peak superimposes the CO bulk oxidation within 20mV of the ignition potential (see Figure 4.16). Beyond the ignition potential the surface becomes oxidized and the CO oxidation can proceed, limited only by CO diffusion.

At sufficiently high potentials, E>1.1 V, the Pt surface becomes gradually covered with oxygen species that are inactive for the CO oxidation, which leads to a decrease in the observed current density, as for instance for polycrystalline Pt in Figure 4.19. A similar behavior was found for nanocatalysts, however, the analysis of this data in the diffusion-limited region with the thin-film method is not applicable at all, and that is why only results for extended surfaces are discussed here.

Figure 4.19: CO bulk oxidation on CO-annealed polycrystalline Pt with a RDE at 1600 rpm in CO saturated perchloric acid electrolyte (sweep rate: 1 mV/sec, T=298 K). Polarization curves for three positive potential limits are demonstrated.
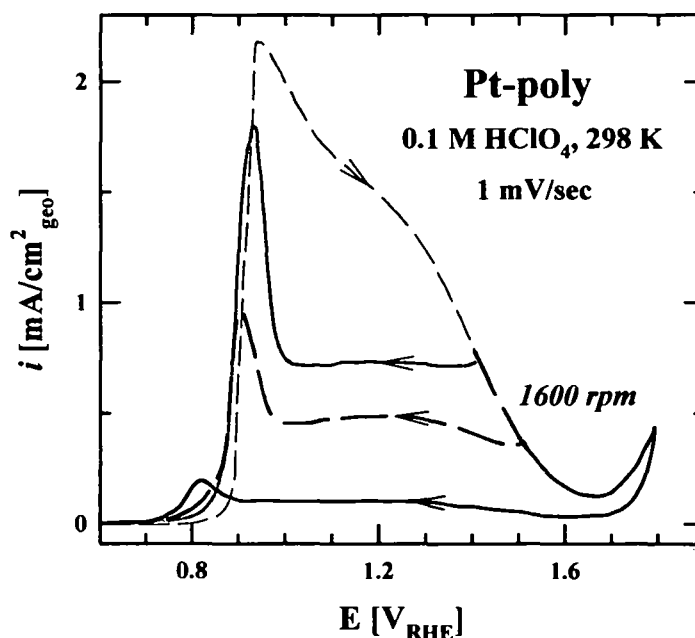
The further the anodic limit lies in the oxide region, the more the surface becomes oxidized and as a consequence blocked for CO adsorption and oxidation, respectively. The surface of Pt-poly is covered to approximately 65% and 80% by oxides at 1.4 and 1.5 V, respectively. Past a potential of 1.6 V, significant oxygen evolution begins on a surface that is considered to be completely oxidized, which results in a negligible current signal obtained upon reversing the sweep direction at 1.8 V. In the cathodic sweep the current signal stays roughly constant at the

value of the positive limit, indicating no change in the available surface sites by additional adsorption or desorption. An increase in current cannot be observed until a potential of about 0.9 to 1.0 V is reached, where the reduction of the Pt surface takes place. CO can then compete for the extricated sites with reactive OH_{ad} and after a maximum in oxidation is observed, the current drops to zero again due to poisoning of the surface by CO. As seen from Figure 4.19, for surface oxidized to a higher degree the position of the peak maximum shifts to more negative potentials and becomes less pronounced. With the highest positive limit of 1.8 V the peak almost vanishes, because the surface transforms virtually direct from an oxide-blocked into a CO-blocked state. However, it can be clearly seen that at a potential of 0.8 V the most active surface is the one that was the most oxidized previously, which supports the conclusions drawn above for the influence of the increased oxophillicity of smaller particles and its consequences for the oxidation reaction.

4.4.3. Summary of the CO-oxidation and comparison with gas-phase catalysis

To point out the striking similarities, the obtained results from the electrochemical measurements will now be summarized and related with the various effects observed in vacuum and gas-phase catalysis for the same reaction under comparable conditions in literature (extended Pt surfaces and high CO partial pressures). Unfortunately, studies of nanocatalysts in gas phase cannot be correlated in a straightforward manner to conclusions drawn from this work on carbon-supported Pt, since they are generally conducted with catalysts on oxide supports, which are known to exert decisive influence on the reactivity [37].

(i)   Applying two different preparation procedures, oxide- and CO-annealing, the role of surface irregularities or defects could be elucidated in the CO monolayer as well as in the "bulk" CO oxidation. These sites facilitate the dissociative adsorption of water in acid electrolyte in the pre-ignition region, which is the initial step in the oxidative removal of a compact CO layer. In a stripping experiment the oxidation continues to adjacent terrace sites and then spreads unstoppable from there. In contrast, with CO in solution and forced convection, continuous re-adsorption of the CO on the surface occurs so that a diffusion limited reaction is not established up to the ignition potential. Clearly, if specific sites on the surface are active for OH_{ad} adsorption, then the electrocatalytic activity for CO oxidation

changes as the concentration of these sites changes with particle size, in agreement with gas-phase catalysis [112;166]. From stripping experiments using FTIR, an increasing activity with growing particle size could be observed in the pre-ignition potential region, concomitant with the increase of the number of defect sites, i.e. $1 \geq 2 > 5 > 30$nm. Accordingly, high-pressure studies of CO oxidation on Pt(111) below a certain temperature with use of SFG spectroscopy [167] reveal that the active CO species are those adsorbed at defect (or distorted) Pt surface sites. Moreover, the reaction rate increases linearly in this case with the surface concentration of those sites, similar to the qualitative results for nanoparticles presented here.

(ii)   In a CO bulk oxidation experiment on an initially completely CO covered surface a sudden rise in the reaction rate emerges at a potential of about 0.9 V. This ignition potential was found to be independent of the particle size, hence the reactivity sequence remains equal $30 = 5 = 2 = 1$nm. Since the isotropic heat of adsorption of CO doesn't change significantly with the surface structure [168], this effect was explained by the initiation of CO bulk oxidation by the direct displacement of CO_{ad} by OH_{ad}. At the ignition potential the OH_{ad} adsorption becomes more favorable than the re-adsorption with CO, the oxidation of the adsorbed monolayer proceeds rapidly and the CO bulk oxidation becomes self-sustained. The critical CO inhibition of O_2 adsorption at CO saturation coverage was described for gas-phase for instance by Su et al. and Burnett et al. [167;169]. For the fully covered Pt(111) surface, the CO oxidation is completely suppressed below the CO desorption temperature, independent of the partial pressure of O_2. A surface with such a densely packed overlayer is no longer active for dissociative chemisorbtion of oxygen, which is the reactive intermediate in gas phase CO oxidation in contrast to dissociatively adsorbed H_2O in acid electrolyte. However, once the temperature of CO desorption is reached, analogically defined as the ignition temperature, more and more adsorption sites become accessible for oxygen and the oxidation proceeds rapidly and directly proportional to the oxygen concentration.

(iii)   In the potential region beyond the ignition potential the surface is predominantly covered by oxygenated species and the rate-determining step in the CO oxidation is the diffusion of dissolved CO to the electrode surface. However, when oxides become so strongly bond to the Pt surface at high enough potentials, they can block the adsorption of CO and therefore inhibit the progress of the reaction. The surface oxide formation on Pt at positive potentials,

which was extensively described in by Conway [170], is very similar to the one in gas-phase and vacuum at elevated temperatures. For instance Niehus and Comsa [171] demonstrated the decisive transformation of a simple chemisorbed state to an bulk-oxide state on Pt(111) during oxygen exposure above 800K. Concomitantly other groups [172;173] found a decrease in the CO oxidation reactivity under high temperature and oxygen partial pressure conditions, which is attributed to the blocking of surface sites by inactive (sub-surface) oxide.

(iv)   Under experimental conditions when the surface is initially covered with active OH_{ad} species, which is the case in the cathodic sweep starting from 1.0V, the electrocatalytic activity of supported Pt catalysts for CO oxidation follows closely the change in oxophillicity with the particle size, i.e. 30<5<2<1nm. This sequence is exactly the one that is expected in electrochemistry, considering the well known desorption rate of OH_{ad} on Pt nanocatalysts from characteristic cyclovoltammograms [110;132]. As already mentioned, the particle size effects observed on oxide-supported catalysts in gas phase are not suitable [37] to directly confirm the influence of the change in oxygen adsorption properties. However, Ertl [174] demonstrated by studying the CO oxidation on an oxide-covered Pt(111) surface using STM, how first CO competes for the step sites in the oxide overlayer, but then starts to react on the domain boundary of that phase, instead of randomly reacting in the mixed phase. With progressing consumption and oxidation of O_{ad}, the empty sites become occupied by the impinging CO molecules (in the absence of O_2 in the molecular beam), which form continuously growing CO patches. If, however, oxygen would be present in the molecular beam, a competitive process for the defect sites would occur, depending on the relative binding energies. Taking into account the results from XPS and EXAFS measurements on carbon-supported Pt in vacuum that showed a higher oxygen binding energy for decreasing particle size [45;47], an identical size effect as in electrochemical measurements would be also expected in gas-phase catalysis on non oxide-supported catalysts.

The selection of these presented results shall intend to demonstrate the high degree of complexity of such an apparently simple reaction like the CO oxidation on Pt. Varying reaction conditions can alter the macroscopic kinetics so extensively, that electrocatalytic activity sequences for the investigated carbon-supported high surface area catalysts of either

30>5>2>1nm, 30=5=2=1nm or 30<5<2<1nm can be established. Only the understanding of the microscopic elementary processes occurring on atomic scale at the catalyst surface can give a further insight into the phenomenon of the catalysis of this oxidation. Examined from this perspective, it is essential to always consider firstly the mutations of the catalyst surface with the surrounding conditions, before the reactions thereon are analyzed and discussed.

4.5. The Oxygen Reduction Reaction on Pt - nanoparticles

The ORR on Pt electrodes is an extensively studied process on bulk polycrystalline and single crystals in various electrolytes (see chapter 3.2.3) as well as high surface area catalysts [115;130;132]. Although effects like the change in specific activity for oxygen reduction with the particle size have been reported previously [39-41;45] and confirmed several times, many important details related to the relationships between the rate of reaction and the size of Pt nanoparticles are still not completely solved and remain challenging. Consequently it is necessary to carefully investigate the oxygen reduction on Pt catalysts and establish some benchmark activities for future catalyst research under consideration of the sources of errors (3.2.3.2 and 4.1.2). Furthermore the effect of the Pt particle size will be demonstrated and set it in relation to the other effects reported in the previous sections. In the end the ORR activities on small particles will be compared to those obtained from extended surfaces.

In Figure 4.20 the ORR polarization curves are exemplarily depicted for the 1nm catalyst at various rotation rates, complementary also the produced peroxide has been detected at the ring.
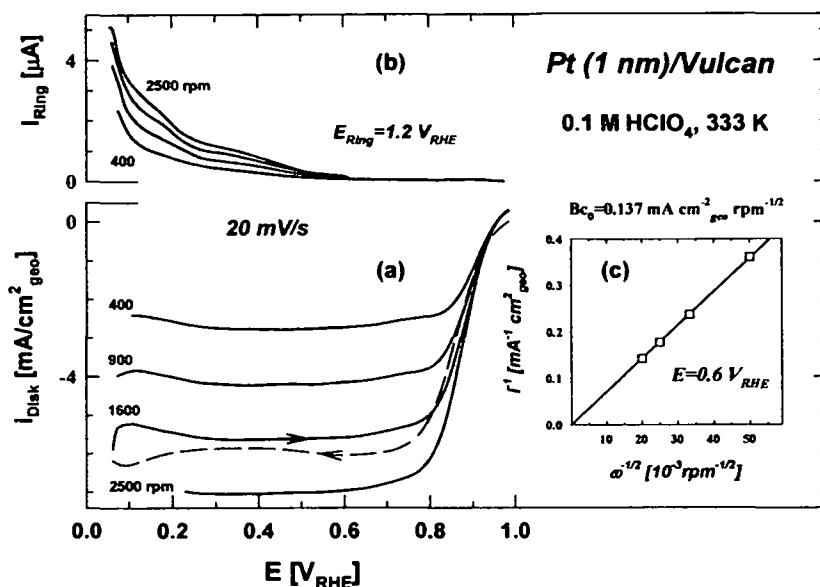
Figure 4.20: Polarization curves for the oxygen reduction reaction (a) and the peroxide production on the ring (b) exemplarily for the 1nm catalyst at different rotation speeds. Experiments were conducted in 0.1M perchloric acid at 333K, with a scan rate of 20mV/sec. Insert (c) shows the Levich-Koutecky plot at 0.6V (diffusion-limited region).

As shown in Figure 4.20a, after sweeping the potential positive from 0.05V the diffusion limiting currents are observed up to about 0.8V. At more positive potentials the ORR is first under mixed diffusion-kinetic limitations and finally, for E > 0.9 V, under a pure kinetic control. In the cathodic sweep, which is only shown for 1600rpm, a similar behavior can be found. However, a slight hysteresis in the kinetic region due to the irreversible formation of oxides at the electrode surface, as well as a deviation due to the double-layer capacity of the high-surface area catalyst exists on sweep reversal, which can be clearly seen in the diffusion-limited region especially for the 1nm catalyst at a sweep rate of 20mV/sec. The latter can be simply corrected by subtracting the cyclovoltammogram recorded in Ar purged solution at the same sweep rate. Similar to the CO oxidation reaction, the Levich-Koutecky plot calculated from data at 0.6V is shown in Figure 4.20c. Close to the data that has been reported in literature for ORR on Pt electrodes [130] and previously for extended surfaces (3.2.3), the slope of the straight approximation, which intercepts at almost zero, is about $0.137 mAcm^{-2}_{geo}rpm^{-1/2}$. Altogether the ORR on HSAC is very similar to model systems, the Tafel slopes are parallel to each other (see Figure 4.3), the apparent activation energies are also in the range of 23 to 29 kJ/mol at the same overpotentials as in Figure 3.10, and a slightly increasing peroxide production with increasing H_{upd} coverage can be noticed at potentials below 0.4V (Figure 4.20b), although the thin-film RRDE method might not be so suitable as expected for HSAC [175;176] and needs further investigation. The same reaction

mechanism is applicable for the ORR on HSAC as on Pt(hkl), and instead of repeating the discussion of chapter 3.2.3.1 only the particle size effect for the ORR will be investigated.

Interestingly enough, the kinetic region of the ORR comprises over the same range of potentials where also the reaction rate of the CO oxidation changes dramatically. In contrast to what was shown for the CO bulk oxidation, however, adsorbed OH_{ad} is not a necessary reactant but rather a product of the reaction [65] that can also be formed in acid electrolyte by the dissociation of water at the electrode surface (section 4.3.2). In either case the OH_{ad} is considered to be a spectator species and thus reduces the number of active sites for the ORR to proceed. Considering that the surface coverage by OH_{ad} is particle size dependent (4.3.2), one may expect that the reaction rate of the ORR will also be determined by the oxophillicity of Pt nanoparticles, which is demonstrated below.
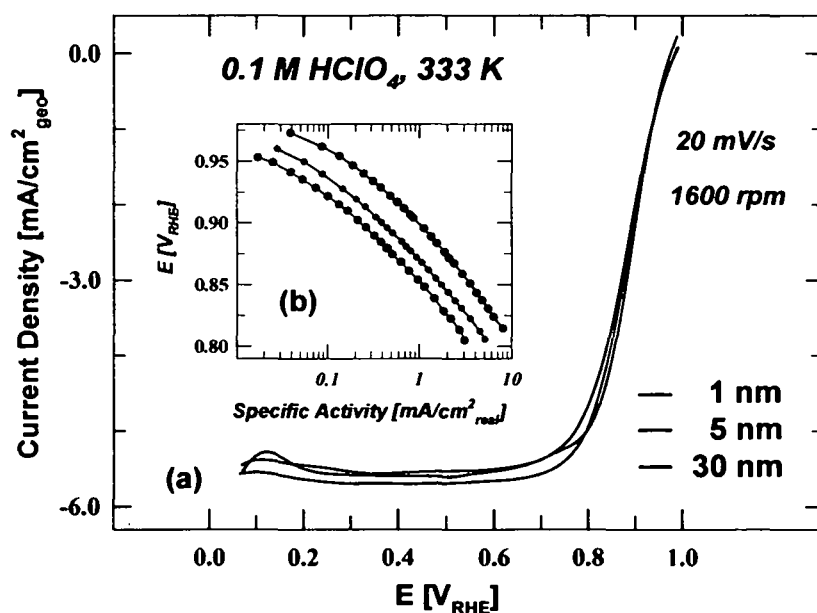
Figure 4.21: (a) Comparison of the oxygen reduction reaction on the 1nm, 5nm and 30nm catalyst (the 2nm catalyst is not shown for clarity) at the positive going sweep. Only the cathodic sweep of the 30nm catalyst is illustrated. In the insert (b) the potential is plotted against the specific activity (Tafel plot).

The anodic polarization curves given in Figure 4.21a for 1nm, 5nm and 30nm catalysts at 1600rpm exhibit the same diffusion-limited current and are overlapping in the kinetic region. In order to obtain reliable, comparable data they have to be corrected for the specific surface area, which was determined from CO stripping experiments (see 4.1). The results are depicted in the logarithmic Tafel plots in insert Figure 4.21b for the kinetic region between 0.95 and 0.85V. A

clear trend can be seen for the activity of the oxygen reduction over the whole potential range, i.e. the smaller the particles the lower the specific current density. Unfortunately it was not possible to fit one single, unambiguous approximation into the plots and determine the Tafel slope, due to the continuous increase of the slope with increasing potential. When comparing different particle sizes however, the overall shape of the curves only changes negligibly, which indicates that the same reaction mechanism is most likely valid for all catalysts as already mentioned. Furthermore it appears that the Tafel plots for different particle sizes are shifted parallel to each other, from 1nm to 30nm for about 50mV or by a factor of 6 when expressed on a potential scale or as specific current density, respectively. This is in excellent agreement with the shift in the pztc of approximately 35mV and the concomitant trend in oxophillicity as described in section 4.3.1 and 4.3.2.
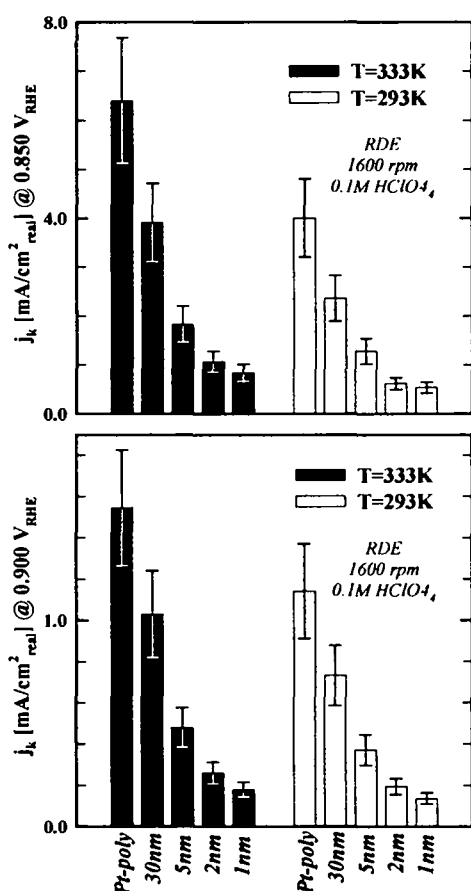

Figure 4.22: Comparison of the ORR specific activity from polycrystalline Pt and carbon supported Pt nanoparticles in RDE measurements in 0.1M HClO₄, at 1600rpm and a sweep rate of 20mV/sec. The kinetic current densities are depicted in the top bargraph at 0.850 V_{RHE} and in the bottom graph at 0.900 V_{RHE}, in each case at 333K and 293K respectively.

To indicate the effect of the particle size on the ORR more clearly, the absolute values of specific activity are depicted in the bargraphs of Figure 4.22 at two potentials and two temperatures for the carbon supported Pt high surface area catalysts as well as Pt-poly. Independent of the temperature or the potential, the specific activity in the kinetic region is enhanced with growing particle size and reaches a maximum on the extended polycrystalline surface. Because of the increased particle size, the 30nm catalyst almost behaves like poly Pt and is only approximately 1/3 less active. The factor between the 5, 2 and 1nm samples and Pt-poly are roughly 3, 6 and 8 respectively. According to the initially discussed experimental parameters for the thin-layer method (4.1.2) and the general errors when evaluating the ORR (3.2.3.2), a precision of approximately 20% is expected, with the major part coming from the determination of the active surface area by CO-stripping. This is in concordance with the error from the actual measurements for each catalyst, which were repeated at least 4 times.

In order to shed more light onto this size effect, a further investigation of the ORR in various electrolytes is summarized in Figure 4.23 below. Since the shape of the ORR polarization curves in H_2SO_4, $HClO_4$ and KOH are equal, only the specific activities of the catalysts are plotted against the specific surface area in Figure 4.23a. Although the absolute values vary slightly, a similar decreasing tendency with increasing the specific surface area, i.e. decreasing the particle size, is clearly demonstrated. In parallel the mass activity in Figure 4.23b initially increases with increasing specific surface area and remains approximately constant in the 1 and 2nm range (within the error of measurement). This particle size effect itself has already been discussed in previous works, it was first observed in phosphoric and sulfuric acid [39-41;44], and later also found also for $HClO_4$ electrolyte [45;132]. The most plausible earlier explanation of the effect by Kinoshita et al [41], however, fails to predict this independence on the supporting electrolyte. Based on the plain geometric consideration that the surface average distribution of single crystalline facets of particles changes with size, i.e. bigger particles contain more (111) and (100) facets, but fewer edge and corner sites that are tentatively modeled by (110) facets, he proposed that the specific activities has to change accordingly. While this is indeed true for KOH, where (111) is the most active surface and thus bigger particles are also superior, the trend in perchloric acid and especially sulfuric acid is unexpected. In the latter electrolyte the (111) surface is the least active due to the specific adsorption of site-blocking sulfate anions [8], but the particle size effect remains the same as in KOH.
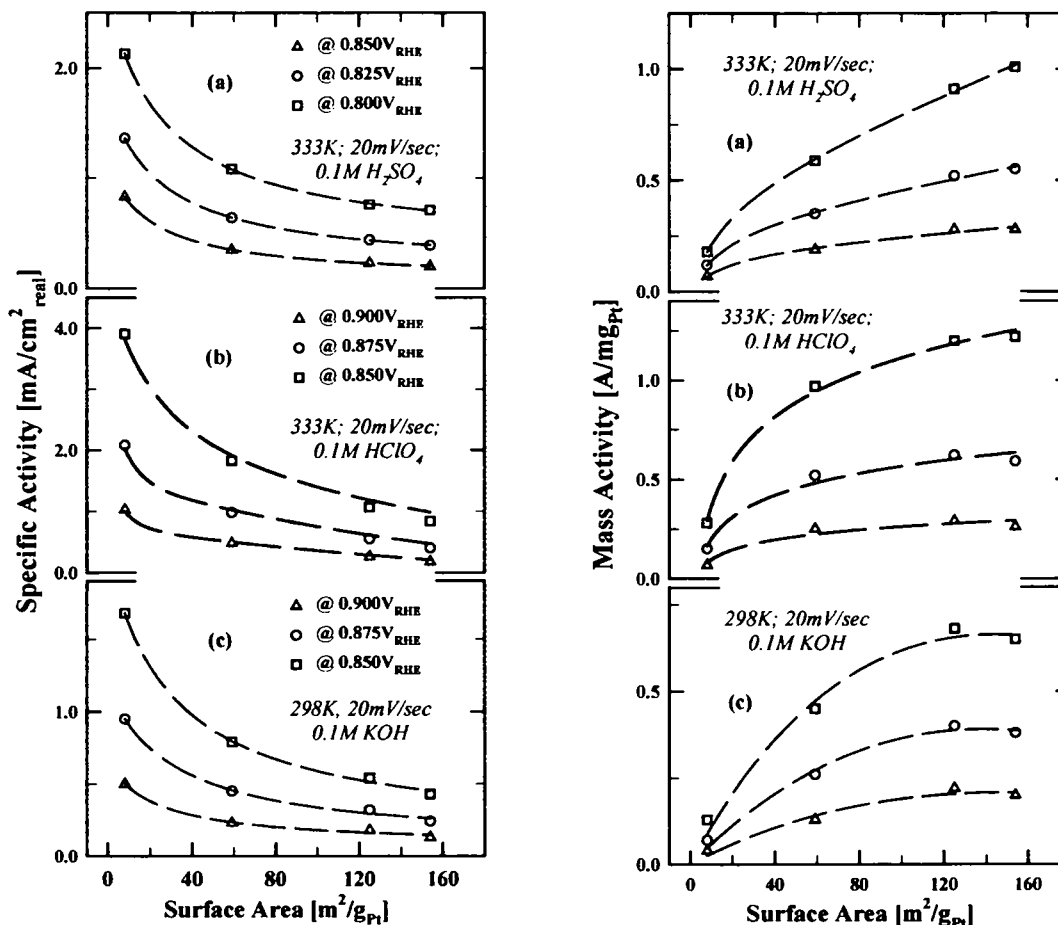
Figure 4.23: Specific and mass activity trends in 0.1mol H₂SO₄, 0.1mol HClO₄ and 0.1mol KOH for the ORR at various potentials. Instead of using the particle size, the activities are plotted here against the specific surface area of the respective catalysts. The potentials given in the left-hand graph are also valid for the mass activity on the right. The temperature was set at 333K in a and b, and at 298K for KOH.

As a consequence a novel explanation is proposed, which links the experienced variation in catalytic activity to the changes in surface electronic as well as geometric parameters with the cluster size. Due to an increase in the dispersion of the catalyst and the concomitant decrease of the average coordination number of atoms by a decrease in the particle size, the potential of total zero charge shifts negative from 0.285V for poly-Pt and 0.282V for 30nm to about 0.245V for 1nm, as seen in 4.3.1. In agreement with Frumkin and Petrii [151], the essential electrosorption properties of the metal catalysts are therefore also dependent on the cluster size (chapter 4.3.2). In particular the energy of adsorption of oxygenated species is more enhanced, i.e. at the same potential the surface coverage by OH_{ad} increases by decreasing the particle size. As a consequence

for the ORR the increase in oxophillicity with smaller particles leads to a decrease in specific activity, because OH_{ad} can effectively block the active sites required for the adsorption of O_2 and/or the splitting of the O-O bond. In agreement with single crystal studies (3.2.3), the rate equation is given by expression (1.1). The reaction rate is thus not determined by the Pt-oxygen heat of adsorption, but rather by the adsorption isotherm of site-blocking oxygenated species, generated from the dissociation of water at the Pt-surface in acid electrolyte.

4.6. Summary and Discussions

In this chapter on Pt HSAC the thin-film method was initially introduced. Additionally the issues of the determination of the active surface area and the specific activity of a catalyst, as well as the optimum Pt loading for the experiment, were treated. Thereafter the structure of the catalyst samples was analyzed by HR-TEM, from the results of which it was concluded that the nanoparticles are not ideal cubo-octahedron's, but also consist of defects and steps. As for model systems, this plays a major role in the kinetics of reactions, which was demonstrated for the oxidation of a CO monolayer. The fact that smaller particles are less active for this reaction than larger ones is in contradiction with the expectations from a more negative pztc or higher oxophillicity. However, it was clearly shown that not the heat of adsorption of the catalyst is the decisive parameter for this particle size effect for CO stripping, but rather the particle size dependent amount of irregularities. They serve as adsorption sites for catalytically active OH_{ad} at low potentials that initiate the oxidation of the adsorbed CO, and therefore control the rate of the reaction. It was therefore suggested that the kinetic reactivity for the CO oxidation should rather be obtained via the CO bulk method, in a CO saturated solution and under the well-defined diffusion conditions at the RRDE, to investigate the impact of the oxophillicity. In case of the ORR the activities of single crystals cannot be used directly to explain the particle size effect for this reaction based on purely geometrical considerations. This was deduced from the independence of the effect of the supporting electrolyte, where single crystals exhibit varying orders of reactivity.

The particle size effect was discussed in a novel approach by investigating the crucial dependence of the adsorption of oxygenated species at the Pt surface in acid electrolyte with regard to the variation of the physical-chemical characteristics of nanoparticles. The main conclusions thereof are summarized in Figure 4.24 below.
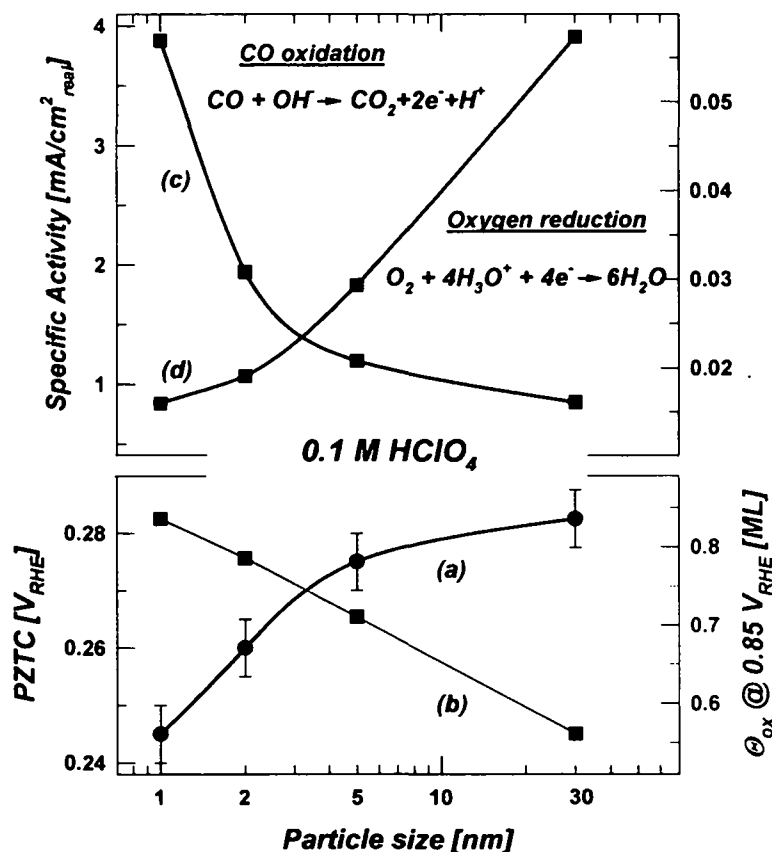
Figure 4.24: Summary of the results from the CO-displacement (a) and cyclovoltammetry (b), as well as from CO bulk oxidation (c) and Oxygen reduction reaction (d), showcasing the adsorption of OH_{ad} and its impact on the electrochemistry at the Pt electrode-solution interface depending on the particle size.

(i)   The potential of total zero charge shifts approximately 35mV in negative direction by decreasing the particle size from 30nm down to 1nm (Figure 4.24a). In agreement with Frumkin and Petrii [151], it was found that the electrosorption properties of the metal catalysts are therefore also dependent on the cluster size. The Pt - H_{upd} interactions appear to be weaker on smaller particles, whereas the heat of adsorption of anions, in particular OH⁻, is more enhanced, i.e. at the same potential the surface coverage with oxygenated species increases by decreasing the particle size (Figure 4.24b).

(ii)   The reaction rate of the CO bulk oxidation (Figure 4.24c) as well as the ORR (Figure 4.24d) is dependent on the particle size, in complete agreement with the variation of the oxophillicity, i.e. the coverage with oxygenated species. If adsorbed OH_{ad} is a promoter of a reaction such as the CO bulk oxidation, then an increase in oxophillicity with a decrease in particle size results in increased specific activity. On the contrary for the ORR the increase in oxophillicity with smaller particles leads to a decrease in specific activity, because OH_{ad} can effectively block the active sites required for the adsorption of O_2 and/or the splitting of the O-O bond, in agreement with the results from single crystal studies (chapter 3.2.3). The reaction rates are not determined by the Pt-oxygen heat of adsorption, but rather by the adsorption isotherm of oxygenated spectator species, generated from the dissociation of water at the Pt-surface in acid electrolyte.

The results clearly indicate that as in heterogeneous catalysis, at the electrified metal-solution interface the catalytic activity is determined by the interaction of surface geometric and electronic factors. Since the distribution of surface atoms varies with the characteristic dimension of aggregates, which was described in this case by the dispersion of the catalyst (average coordination number), each size cluster exhibits unique electronic properties, as demonstrated in this chapter by the potential of zero total charge. This can be considered as the origin of the variation of the reaction rate with the particle size for the presented reactions.

5. Platinum alloys

After introducing the basics of electrocatalysis on fuel cell reactions for Pt model systems in chapter 3 and linking this knowledge to the phenomena related to practical catalysts in chapter 4, the recent, most outstanding approach for improvement of the efficiency of Pt will be investigated. Pt alloys are actually already well established as anode catalysts for fuel cells, due to their superior resistance against poisoning CO compared to pure Pt. The alloying component in applied catalysts such as Pt_3Ru [48;61] or Pt_3Sn [49;62] does not interact with CO but rather serves as an adsorption site for OH_{ad} at low potentials, which can react in a Langmuir-Hinshelwood type reaction with the site-blocking CO_{ad} on adjacent Pt atoms. Despite of this desired bifunctional effect for the oxidation of CO, the enhancement of the activity of the ORR by alloying Pt with transition metals (TM=Co, Ni, Fe, Cr, V) has only recently attracted higher attention and is still insufficiently understood. Several studies with supported alloy catalysts report an improved activity compared to Pt [57;58;177;178], however the considerable impact of the particle size and other uncertainties in the kinetic measurements as previously described in section 4.1 were usually neglected, which is reflected in the contradictory interpretations in literature. Furthermore no fundamental insight into a possible improvement can be achieved by utilizing only the electrochemical information gained without knowledge of the exact surface composition or the stability of this kind of nanoparticles. Therefore it is essential to again start out first with well-characterized alloy model systems with extended surfaces, before high surface area bimetallic catalysts are studied.

One major issue of alloys that has been the object of intensive studies in the past few decades is the change of the surface composition due to surface segregation phenomena, i.e. the enrichment of one element at the surface relative to the bulk concentration. Aside from a few very first reports from Stamenkovic et al. [59;60], however, the impact of the surface segregation on the kinetics of bimetallic surfaces in the electrochemical case has not been explored sufficiently.

The authors mentioned above compared the reaction rate of the ORR on the bulk alloys of Pt_3Co and Pt_3Ni, as well as on the so-called "Pt-skin" structure that was produced by surface segregation of Pt, i.e. an exchange of Pt and Co in the first few layers after annealing. The LEISS results revealed that for a polycrystalline Pt_3Co alloy the outermost layer of the clean annealed surface is pure Pt, with predicted Pt depletion in the second layer. It was found that especially the latter surface is uniquely active for the ORR, the rate of reaction being higher by a factor of four compared to pure Pt. Similar results were observed in the case of Pt_3Ni.

Continuing in a surface science approach, in this chapter a detailed investigation of the Pt-alloy systems will be presented on the basis of Pt_3Fe, i.e. the surface composition and stability will be correlated to the ORR activity.

5.1. Experimental

5.1.1. Surface preparation and characterization

The polycrystalline bulk alloy materials used in this study were prepared by conventional melting metallurgy. The composition of the bulk (x_b) was determined via x-ray fluorescence spectroscopy; x-ray diffraction showed all specimens to be single-phase fcc solid solutions of Pt and TM having the expected lattice constant for 75 % Pt [179]. Cleaning, modification and surface characterization procedure were performed in UHV system, which is equipped with an angular-resolving double pass cylindrical mirror analyzer (PHI-DPCMA Φ15-255GAR) with an electron source at its center, under pressure in the $1 \cdot 10^{-10}$ Torr range. UHV cleaning procedures were done by repeating of sputtering-annealing cycles with Ar^+ and oxygen until Auger electron spectroscopy (AES) indicated that, for given experimental conditions, an ideally clean (carbon and oxygen free) surface was produced. AES spectra were recorded in derivative mode using the 3 keV electron beam energy, 3 eV_{p-p} modulation and -5 μA beam current in the range from 140 to 900 eV.

In order to produce different surface compositions, clean samples were either annealed at 1000 K in UHV or mildly sputtered with a 0.5 keV beam of Ar^+ ions. The surface compositions of alloy samples were determined by low energy ion scattering spectroscopy (LEISS), a compilation of surfaces analyzed applying LEISS by Watson et al. [180] was used as a reference. LEISS spectra were taken with Ne^+ beam energy of 1 keV with sample currents from 5 to 30 nA at residual Ne pressure of $2.5 \cdot 10^{-8}$ Torr. Scattering angle was 127°, and the incidence angle was 45°. A differentially pumped ion gun (Φ04-303A) was used to raster the Ne^+ ion beam over approximately 3mm × 3mm surface area. The recording time was 60 s/spectrum. The clean Pt reference sample was prepared in the same manner by conventional metallurgy and pre-treated in UHV using mild sputter cleaning and/or annealing techniques in exactly the same way.

The UPS measurements are carried out at beamline 9.3.2 of the Advanced Light Source, Lawrence Berkeley National Laboratory. All UPS measurements are taken under 5×10^{-10} torr or below and a hemispherical electron analyzer (Scienta SES-100) is used. The incident photon energy is set to 90 eV and the total energy resolution of spectrum is set to 0.05 eV or less. All UPS spectra are taken at normal emission direction from the sample surface. The integration background, i.e. Shirley background, is applied to the measured spectrum and the center of d-band is calculated from the background-subtracted spectrum.

5.1.2. Electrochemical measurements

The UHV prepared and characterized alloy surfaces were withdrawn from the UHV introductory port (field with argon) into air and covered immediately with a drop of triply-pyrolitically distilled water, for details see references [59;181]. The electrodes were then mounted in a rotating ring disc electrode setup and finally immersed into the electrolyte under potential control at ~0.05V vs. RHE in 0.1M $HClO_4$ as described in detail in section 3.2 for Pt crystals.

5.2. Surface Analysis

In several studies from Gauthier et al. [182-184] and Bardi et al. [185] single-crystals of Pt based alloys, predominantly of Pt-TM surfaces, exhibit oscillations in the composition of the alloying component in the first several atomic layers. For the most (111) and (100) oriented crystals the outermost layers of the clean, annealed surfaces are *pure* Pt, which are hereafter simply called "skin" structure, combined with Pt depletion (=TM enrichment) in the second layer. In previous studies it was reported that catalytic properties of the "Pt-skin" structures are superior in comparison with the surfaces having both alloying components in the outermost atomic layer and/or pure polycrystalline Pt surface [59;60]. The origin of the catalytic enhancement was predicted to be the consequence of the electronically modified topmost Pt layer where the catalytic reaction takes place.
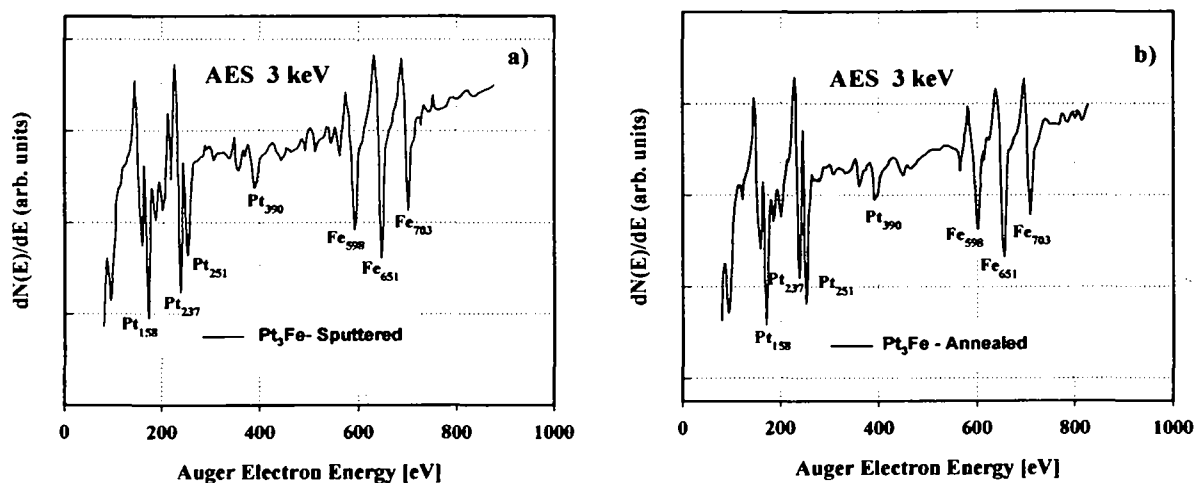
Figure 5.1: Auger electron spectra of Pt₃Fe surfaces: (a) mildly sputtered and (b) annealed at 1000K.

The Auger electron spectra (AES) of polycrystalline Pt₃Fe, obtained after either mild sputtering or annealing of specimens, are given in Figure 5.1. It was thereby confirmed that after sputtering or annealing cycles both alloy surfaces were clean, showing only the characteristic Pt (158, 168, 189, 199, 237, 251, 390 eV) and Fe (600, 647, 705 eV) peaks. No shift of any peak was observed when comparing both AES spectra, however a significant change of the peak intensities has been found for both elements. The annealed surface in Figure 5.1b exhibited a decrease in all three Fe peak intensities relative to the Pt peaks. This is a first indication that the surface

segregation of Pt occurs on the polycrystalline Pt_3Fe alloy, similar to the previously studied systems. Since quantitative surface analysis with AES is quite complicated, requiring modeling of the emission from several subsurface layers with dynamic scattering of the Auger electron, only a qualitative interpretation of the data is attempted.
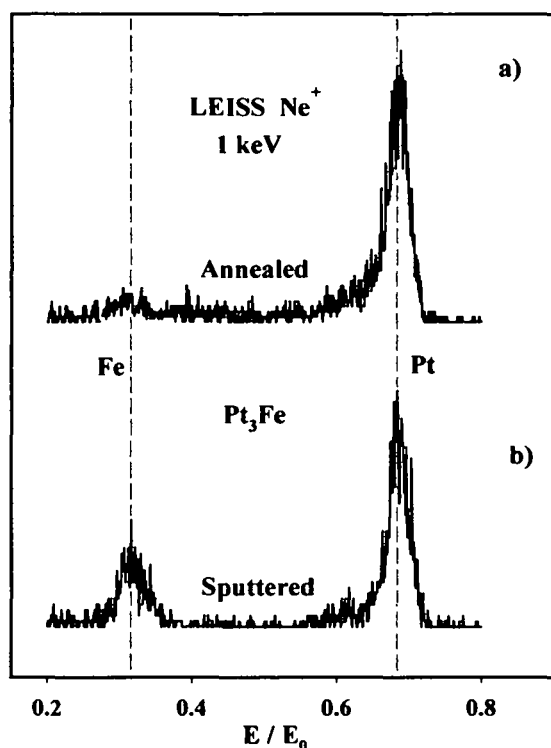
Figure 5.2: LEISS spectra of Pt_3Fe surfaces: (a) annealed and (b) mildly sputtered.

A precise analysis of the surface composition of the Pt_3Fe alloy was obtained by optimizing LEISS, which is the most surface specific technique and most suitable for studies of segregation phenomena. The LEISS results using a 1 keV Ne^+ beam are shown in the Figure 5.2, where the positions of the scattering peaks of the Pt and Fe correspond to the ones calculated from the classical equation for elastic collisions (section 2.6). In contrast to the bulk-like 3:1 surface composition after sputtering Figure 5.2 (b), after annealing at 1000 K the outermost atomic layer consists of almost only Pt atoms (a), revealing that the "Pt-skin" structure can also be formed on the Pt_3Fe alloy. The exact surface composition is found to be 97 at.% Pt by integration of the corresponding peaks and applying the elemental sensitivity factors of polycrystalline materials [186]. This result is in very good agreement with Gauthier's reported findings for the composition of the first atomic layer on $Pt_{80}Fe_{20}(111)$ alloy [184].
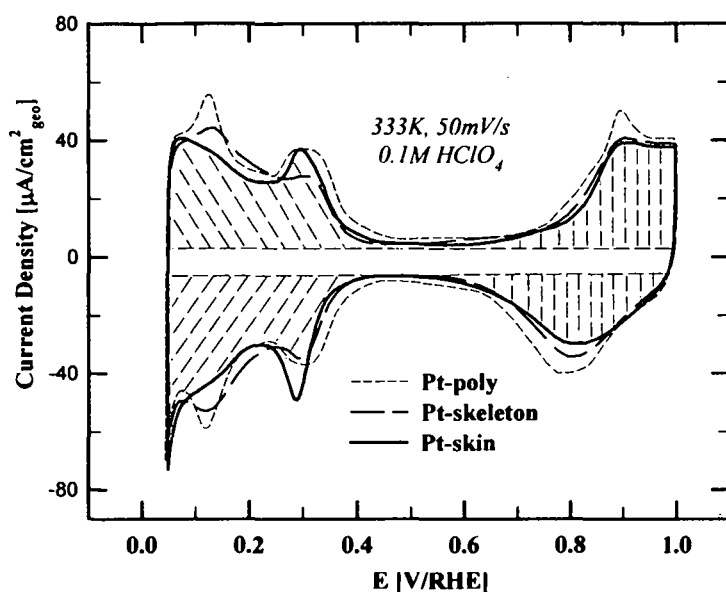
Figure 5.3: CV's of Pt₃Fe-annealed and Pt₃Fe-sputtered compared to Pt-poly in 0.1M perchloric acid with 50mV/s at 293K.

Both annealed and sputtered electrode surfaces were transferred and mounted into the electrochemical cell for additional characterization. CVs of Pt₃Fe surfaces were resembling those from previously characterized polycrystalline electrodes recorded in argon purged 0.1 M HClO₄ at 293 K. Two general findings emerge from the voltammograms in Figure 5.3:

(i) Similar to polycrystalline Pt a striking H_{upd} region is observed between $0.05V < E < 0.4V$, which is also accompanied by a rather weak adsorption/desorption process of anions of the supporting electrolyte. The peaks located at 0.15 and 0.3V are somewhat distorted, the integrated H_{upd} area for the bimetallic surfaces appears to be equal to the one of pure Pt however (see Table 5.1). The total charge for the annealed surface is $175\mu C/cm^2$, the sputtered surface $203\mu C/cm^2$ compared to $195\mu C/cm2$ on a polycrystalline Pt electrode (section 3.2.3.2).

Integrated H_{upd} region	Pt₃Fe [µC/cm²]	Pt-poly [µC/cm²]
Annealed	175	210
Sputtered	203	210

Table 5.1: The total charge under the H_{upd} region for different surfaces

(ii) Despite the similar overall shape of the CVs, the onset of oxide formation at $E > 0.7V$ on the Pt surface atoms is clearly affected by the presence of subsurface Fe atoms and a shift towards more positive potentials on Pt_3Fe surfaces becomes obvious. For the annealed surface, this positive shift is more pronounced, which produces lower oxide coverage at the potential region where the oxygen reaction starts, i.e. $0.75V < E < 0.95V$. In accordance with the earlier discussions on the ORR on Pt single crystals and HSAC in sections 3.2.3 and 4.5 respectively, this is the essential factor to achieve enhanced catalytic activity.

Since in principle the CVs are very similar and no additional peaks for the alloying component can be defined, most likely the top layer of the electrodes in each case consists of Pt atoms only. The small deviations however suggest that alloying with TM does affect the adsorption properties, even if the TM is not directly at the surface of the catalyst.
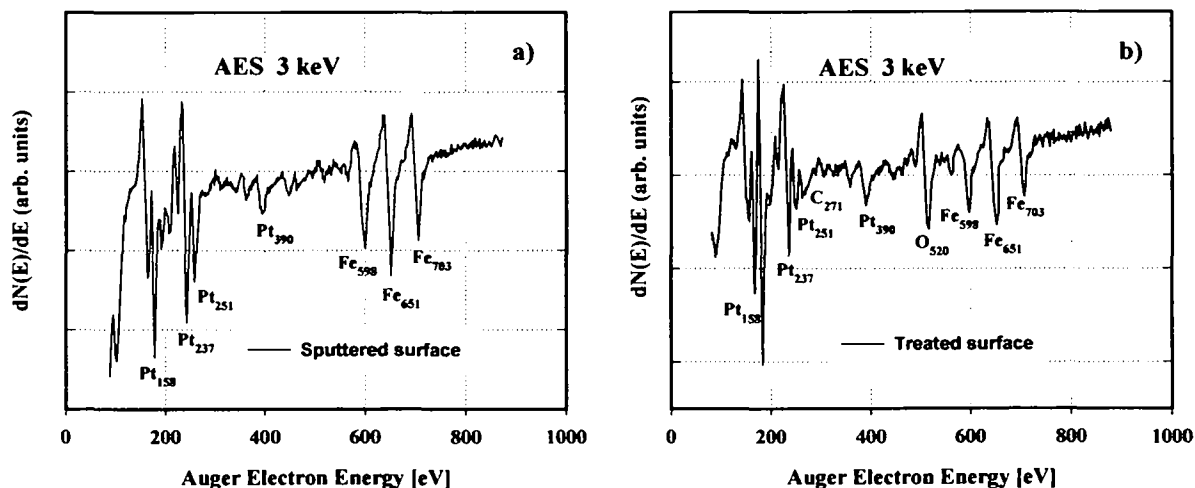
Figure 5.4: AES of mildly sputtered (a) and the same surface after electrochemical treatment (b).

In order to check the surface composition after exposure to the electrolyte and confirm the conclusions from CV, the electrode was transferred back to the UHV chamber for further analysis. A set of representative Auger spectra demonstrates the behavior of the alloys in Figure 5.4. A significant decrease of intensities for Fe peaks is detected in Figure 5.4b, whereas signals for carbon at 271 eV and oxygen at 520 eV were in the reasonable range indicating the

'clean'/successful transfer to UHV chamber. From these and all other observations it was concluded that dissolution and/or leaching out of alloying component indeed takes place in the near surface region when the electrode is brought in contact with the electrolyte. So the alloy surface consists of only Pt atoms in the top-layer, and due to roughening in the case of the sputtered surface it has a little higher surface area than corresponding annealed surface (see Table 5.1).

The physical picture that was developed of the sputtered and annealed Pt_3TM surface composition before and after exposure to electrolyte is summarized in Figure 5.5. Briefly, the TM from the is leached out from the sputtered surface upon transfer to electrolyte and generates a so-called "Pt-skeleton" structure, whereas the Pt-skin structure of the annealed surface formed already in UHV remains stable.
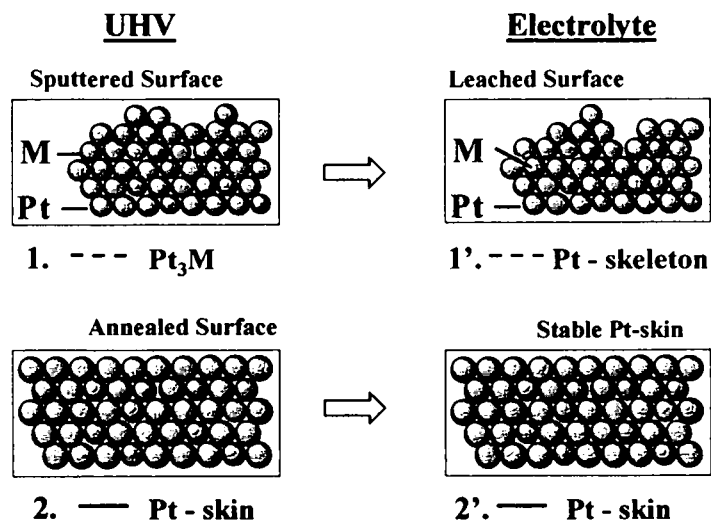
Figure 5.5: Cross section of the surface of a Pt_3TM alloy in UHV (left) and electrolyte (right). The TM atoms (blue spheres) from the sputtered surface (top row) leach out upon transfer to electrolyte and generate a Pt-skeleton structure, whereas the Pt-skin structure of the annealed surface (lower row) formed already in UHV remains stable.

Insight into the electronic surface properties was provided by UPS characterization of the Pt_3Fe (annealed as well as sputtered) surfaces and Pt poly surfaces (Figure 5.6). Based on extensive density functional theory (DFT) studies of transition metals systems, Nørskov and co-workers [66;187] have concluded that the most consistent correlation between electronic structure and binding energy of adsorbates like H_2, O_2, and CO is the d-band center. The p-th center of calculated d-band is defined as $\mu_p = \int N(\varepsilon)\varepsilon^p d\varepsilon$, where $N(\varepsilon)$ is the density of states (DOS), p is the order of momentum, and μ_1 / μ_0 is the first moment of DOS or its center of gravity. Thus

derived values for d-band centers for these surfaces are given in Figure 5.6 next to each experimental curve in brackets.
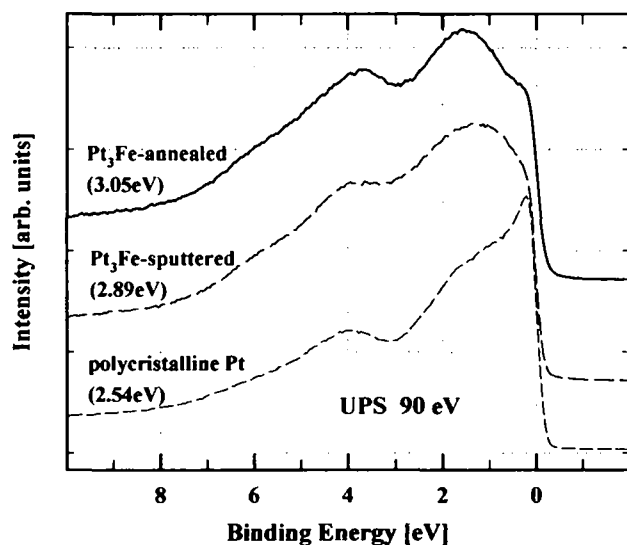
Figure 5.6: UPS data of Pt₃Fe sputtered and annealed as well as Pt-poly using an incident beam of 90eV. The characteristic d-band center was calculated from these curves after applying a Shirley background correction.

The significant shift of the d-band center for sputtered and annealed alloy surfaces compared to the Pt poly surface (sputtered and annealed exhibit the same d-band structure), obvious from the reduced density of the states at the Fermi level, indicates a difference in electronic properties. According to the electronic theory of Nørskov and co-workers [65;66] the shift in the d-band center for Pt₃Fe vs. pure Pt should be correlated to a *reduced* heat of adsorption of molecules like H_2, O_2 and CO. The higher ORR activity could therefore be explained by less stronger bonding of O_2 molecules and the consequently reduced blocking of active sites. Note that the approach formally deviates from the results and process explanations earlier, since it is actually assumed that the blocking effect of OH_{ad} is caused by the aqueous electrolyte rather than by the gaseous O_2 (see also sections 3.2.3 and 4.5). The electrochemical characterization of Pt₃Co and Pt₃Ni alloys already displayed these expected differences in adsorption properties as well as their catalytic activities in comparison with Pt-poly [59;60], and in the following this will be extended to the analysis of the Pt₃Fe surfaces.

5.3. Activity for the ORR

Independent of a Pt-skin or skeleton structure for Pt-alloys, a similar behavior for the ORR was also experienced during the same experiments performed with pure Pt electrodes. As a consequence the basics of the ORR on a Pt surface shall not be repeated, only the impact of the alloying component on the activity will be presented.

5.3.1. Pt-alloy model systems

All potentiodynamic measurements of the ORR reported in this work were reproducible in consecutive scans and remained stable at all temperatures $(293K < T < 333$ K). Thus there were no signs of additional surface changes during the experiments, which was also confirmed by cyclic voltammograms before and after the catalytic measurements. The activities for the ORR obtained for Pt_3Fe surfaces, expressed as diffusion corrected kinetic current densities, are compared to the one of Pt-poly in Figure 5.7. At several electrode potentials, from 0.85 to 0.925 V_{RHE}, both skin and skeleton surfaces exhibit uniquely high activity for the ORR. The catalytic acceleration of the ORR on the Pt_3Fe-skeleton and Pt_3Fe-skin surface compared to Pt approaches a factor of 2 and 3, respectively, quite similar to the results for well-defined Pt_3Co and Pt_3Ni electrodes. This is no surprising result, considering that the similar chemistry of these transition metals may induce also an analogous change of the electronic properties of the topmost Pt atoms. As already mentioned previously, pronounced activity is in agreement with inhibition of oxide formation on the alloy surfaces. A positive shift of more than 50 mV in oxidation potential (Figure 5.3) results in a parallel shift of the ORR polarization curve relative to Pt-poly.
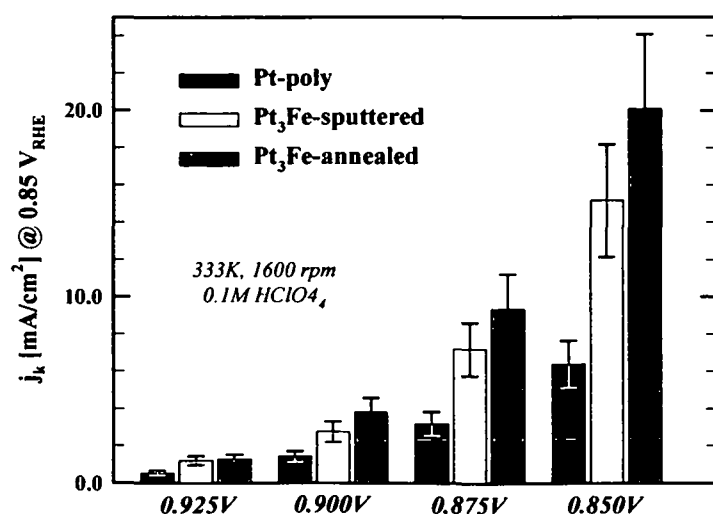

Figure 5.7: Histograms with error bars of the kinetic currents densities for the ORR at several electrode potentials at 333 K for Pt_3Fe and Pt-poly surfaces.

The characteristic behavior for all Pt_3TM metal electrodes in general [59;60] and Pt_3Fe in particular for the oxygen reduction can be summarized as follows:

i) Well defined diffusion limiting currents j_d for the ORR ($0.2 < E < 0.7$ V) are followed by a region of mixed kinetic-diffusion control between $0.8V < E < 1.0V$. Levich-Koutecky analysis confirmed a $4e^-$ process as well as a reaction order of unity with respect to the O_2 partial pressure.

ii) In both potential regions the ring currents are only a small fraction of the disc current, revealing that the ORR proceeds almost entirely through a $4e$ reduction pathway. The increase of peroxide oxidation currents is combined with the adsorption of hydrogen ($E < 0.2$ V), approaching the maximum of approximately 10% at 0.075V.

iii) The Tafel slopes obtained from the potentiodynamic measurements were found to be in the range between 65 and 70 mV/dec, however only for a narrow region above $E > 0.83V$. The apparent activation energies determined in the temperature interval (between 293-333 K) from the least square regressions were essentially identical on polycrystalline Pt and Pt_3Fe surfaces covering the range from 23 to30 kJ/mol. These values are in close agreement with the data obtained for single crystal platinum electrodes, polycrystalline platinum (section 3.2.3 and ref. [8;188], carbon supported Pt (section 4.5) and well-defined Pt_3Co and Pt_3Ni electrodes.
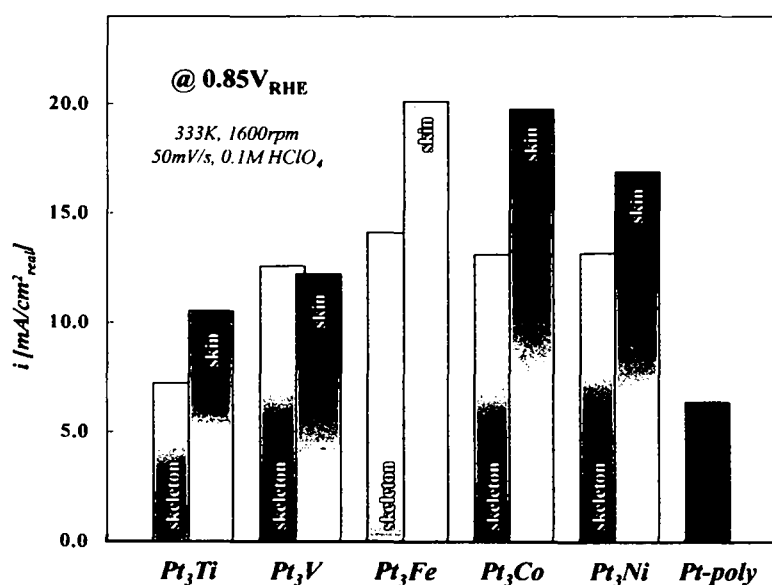

Figure 5.8: Comparison of the activities of various well-characterized Pt_3TM alloys and Pt-poly at $0.85V_{RHE}$ and 333K.

Therefore the reaction mechanism on all of these electrodes must be identical due to the same/similar potentiodynamic behavior, Tafel slopes and apparent activation energies, i.e. a "series" 4e⁻ reduction pathway leading to water as a reaction product as presented schematically in Figure 1.1 in the introduction. Moreover the reaction rate of the ORR on Pt_3TM alloy surfaces in $HClO_4$ is primarily determined by the potential dependent surface coverage of OH_{ad} species, i.e. by the $(1-\Theta_{OH})$ term from equation (1.1), with all other terms being essentially the same.

This is confirming the previously proposed explanation that the catalytic improvement of Pt-skin/annealed and Pt-skeleton/leached out electrodes can be attributed to the weaker $Pt-OH_{ad}$ interaction on an electronically modified layer of Pt atoms. This effect is indeed much more pronounced on annealed surfaces then on sputtered surfaces due to the higher content of alloying TM component in subsurface layers, where the segregated Pt overlayer plays a protective role, i.e. preventing dissolution of underlying, enriched transition metal atoms. The electronic modification of Pt has been confirmed by the shift of the metallic d-band center relative to the Fermi level, which caused a desirable change of the surface adsorption properties and the improvement of catalytic activity for ORR.

5.3.2. High surface-area Pt-alloys

The ultimate goal of all the studies on the ORR is the development of a superior catalyst for practical applications. Pt-alloys seem to be promising systems, so a further investigation was launched whether an improvement in activity can also be achieved with high surface-area catalysts as found for the extended surfaces. Using the same experimental setup and conditions as described in chapter 4, various binary and ternary PtTM-alloys supported on organic whiskers [133] with different compositions were analyzed. In contrast to pure Pt-HSACs, which are generally stable over the timeframe of an experiment, the CVs of dispersed alloys indicate changes of the particle structure, especially in the initial sweeps after immersion into electrolyte (see Figure 5.9).
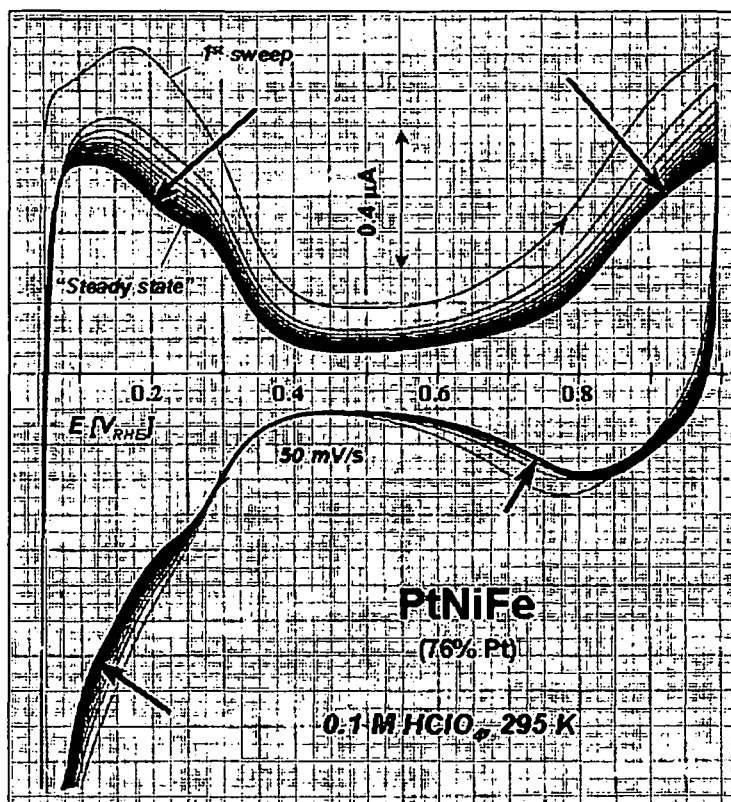
Figure 5.9: Initial changes in the CV of a HSA Pt-alloy after contact with electrolyte.

The catalysts seem to undergo a surface restructuring process, in which the alloying component is leached out from the top-layer of the electrode in analogy to the effect described for sputtered surfaces in section 5.2. Only when a stable Pt-skeleton structure is formed, the process stops and reproducible CVs can be obtained. Supporting this view is also that the extent of the dissolution of TM is more pronounced the lower the Pt content in the catalysts is. As a consequence the particle size of these catalysts decreases relative to the identically synthesized 30nm pure Pt-catalyst previously discussed in chapter 4, and according to the particle size effect a concomitant decrease in the specific activity would be expected. As seen from Figure 5.10, however, the specific current densities of the alloys remain relatively unchanged at all potentials in the mixed kinetic-diffusion region.

Figure 5.10: Specific current density of a 30nm pure Pt and various PtNiFe-alloy catalysts supported on organic whiskers at 333K in perchloric acid.

This finding can be explained by the electronic effect introduced by the remaining TM in the subsurface region onto the surface Pt-atoms that are in direct contact with the electrolyte. As displayed in 5.3.1, an enhancement factor of 2-3 in the specific activity can be achieved for alloy surfaces, depending on the physical arrangement of the elements in the near-surface region. Therefore, although some of the TM was lost due to leaching from the outermost layers, still enough seems to be left in the bulk of the particles to electronically compensate for a reduced specific ORR activity caused by the reduced particle size. The benefit of these novel catalysts becomes obvious when the Pt mass activity is derived applying equation (4.4), as shown in Figure 5.11:
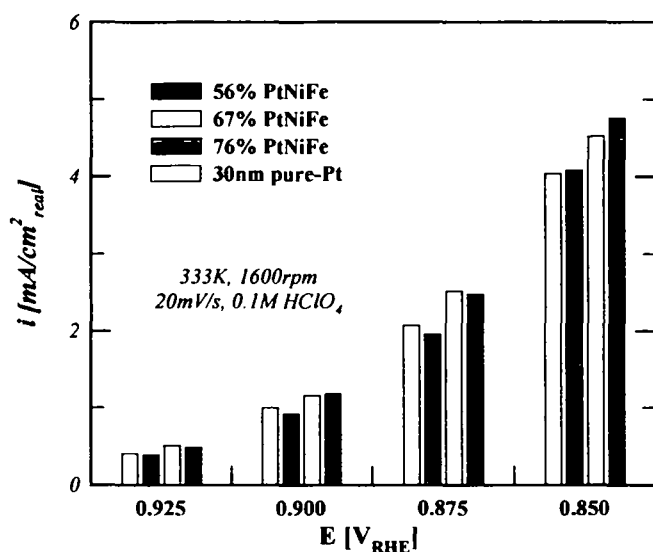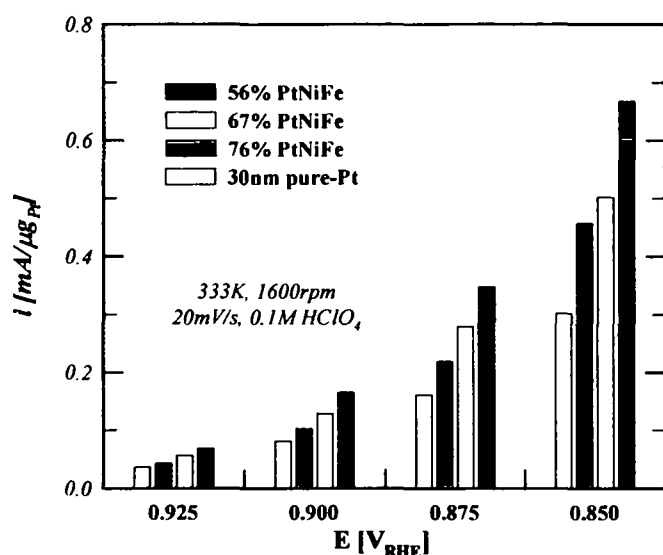
Figure 5.11: Mass Activity of a 30nm pure Pt and various PtNiFe-alloy catalysts supported on organic whiskers at 333K in perchloric acid.

The tendency of increasing mass activity with a decrease in the relative Pt content is clearly visible. This is a logical consequence of the fact that smaller particles with a similar specific activity due to the alloying effect, exhibit a superior surface area because of roughening of the surface. The roughness factors r_f, determined by CV (section 4.1), of the samples are 3.0, 4.4, 4.8 and 5.9 respectively. The most active PtNiFe catalyst consists of 56% Pt ($r_f = 5.9$) and its Pt mass activity is enhanced by a factor of more than two. Note that as discussed in 5.3.1, the basic concepts of the ORR, like the 4e⁻ pathway (Figure 1.1), the rate-determining step (equation (1.1)) or the apparent activation energy, remain valid for all the catalysts described here and will not be repeated here.

The advantages of PtTM-alloys over pure Pt HSACs have been unambiguously demonstrated. Based on the previous fundamental considerations of the particle size effect and the investigations on extended alloy surfaces, a novel, improved understanding of the dispersed Pt-alloys could be gained. More efforts are however required to achieve a complete picture of the properties of these catalysts prior to a feasible commercialization. Future work should hence focus on FTIR and TEM analysis of alloy particles, as well as practical electrochemical studies of the corrosion behavior.

5.4. Summary and Conclusions

The influence of the surface composition of Pt_3TM alloys on the kinetics of the fuel cell cathode reaction has been demonstrated using Pt_3Fe as a standard. All electrode surfaces were characterized in UHV and subsequently transferred into the electrochemical setup.

Depending on the preparation procedure, two different surface compositions of Pt_3Fe electrodes have been produced in UHV: a sputtered surface with 75 % Pt and an annealed surface with ~100 % Pt atoms. UHV immersion experiments revealed that transition metals are leached out from the top surface layers of the sputtered sample after contact with electrolyte (Pt-skeleton), whereas the annealed crystals with a TM-enriched subsurface layer remained stable.

Both surfaces exhibited different electronic properties, which was established from UPS measurements of the d-band center relative to the Fermi level, with the highest shift in the d-band center position relative to Pt-poly electrode corresponding to the Pt-skin surface. The electrochemical characterization in 0.1 M $HClO_4$ electrolyte clearly indicated that the cyclovoltammetic features for sputtered and annealed surfaces are the same as those for pure polycrystalline Pt. This is an important confirmation that in both cases the top layer consists of only Pt atoms with about the same surface area (no major roughening).

The order of activities at 333 K was Pt-skin> Pt-skeleton > Pt with the enhancement of catalytic activity for Pt-skin being more than 3 times higher at various potentials than for a pure Pt electrode. The superior activity of the Pt-skin electrode has been attributed to the larger electronic modification of the Pt overlayer from enrichment of alloying component in the subsurface atomic layer and the consequent slight positive shift in the adsorption potential of OH_{ad}. Both, the leaching out of TM from the top-layer of particles as well as an enhancement of the catalytic activity was also found for high surface area Pt-alloys. These systems most definitely provide the basis for the future design and development of high surface area catalysts for fuel cells.

6. Summary

The objective of this work was to investigate the CO oxidation and the oxygen reduction reaction on different types of Pt electrodes to improve the understanding of those important fuel cell reactions. The reactions were first studied on single crystal and polycrystalline model electrodes, in order to demonstrate the importance of fundamental research, and then compared with the results obtained with high-surface area catalysts, which are used for practical applications. Applying both, electrochemical analysis with in-situ FTIRAS and regular cyclovoltammometry, as well as surface characterization techniques, such as TEM, AES, UPS and LEISS, novel insights on the reaction mechanism and the particle size effects could be achieved. Based on this information from pure Pt systems, also more complicated mixed catalysts such as the promising Pt-alloys were analyzed unambiguously.

(1)   The *oxidation of a CO monolayer* (CO stripping) was evaluated on the Pt model systems as well as on platinum nanoparticles in the size range from 1 to 30 nm. The importance of defects, step and kink sites as adsorption sites for catalytic OH_{ad} was investigated in FTIRAS experiments by monitoring the vibrational frequency of a-top CO (ν_{CO}) as well as the concomitant development of the asymmetric O-C-O stretch of dissolved CO_2. On Pt single crystals the reaction rate depends on the number of step and kink sites, which can be controlled by the pretreatment of the electrode. CO annealing always reduces the amount of irregularities and therefore thus prepared surfaces are less active for the oxidation of a CO monolayer than oxide annealed ones. For Pt cluster TEM analysis revealed that they are not perfect cubo-octahedrons and that large particles have rougher surfaces than small particles, which show fairly smooth (111) facets. It was found that defects play a significant role in CO "clustering" on nanoparticles, causing a decrease or increase in local CO coverage, which yields anomalous redshift or blueshift

V_{CO} frequency deviations from the normal Stark-tuning behavior. The observed V_{CO} deviations are accompanied by CO_2 production, which is enhanced with increasing number of defects on the nanoparticles, i.e. 1nm $\leq$ 2nm < 5nm << 30nm. Moreover it was concluded that the catalytic activity for CO adlayer oxidation is predominantly influenced by the activity of the surface to dissociate water and causing the formation of reactive OH_{ad} on step, kink and defect sites.

(2)   The *particle size effect* on the formation of OH_{ad} adlayer, the anodic CO bulk oxidation and the cathodic oxygen reduction reaction was studied on Pt nanoparticles in perchloric acid electrolyte. From measurements of the CO displacement charge at controlled potential, the corresponding surface charge density vs. potential curves permitted the determination of the potentials of total zero charge (pztc), which shifts approximately 35mV in negative direction by decreasing the particle size from 30nm to 1nm. As a consequence the energy of adsorption of OH_{ad} is more enhanced, i.e. at the same potential the surface coverage with OH_{ad} increases by decreasing the particle size, which in turn affects the catalytic reactions. The impact of the electronically induced potential shift in the OH_{ad} adsorption is demonstrated by the CO bulk oxidation, in which adsorbed OH_{ad} is an educt species and promotes the reaction, and additionally by the ORR, where it can act as a surface site blocking species and inhibit this reaction.

(3)   The *Platinum alloys* were demonstrated as the most promising systems for future development of practical fuel cell catalysts. Using a bulk Pt_3Fe electrode as an example, it was shown that two different surface compositions could be produced for Pt-alloys by pretreatment, i.e. the Pt-skeleton and the Pt-skin structure. Cyclovoltammograms and LEISS revealed that after immersion into the acid electrolyte the surface layers in both cases consist of Pt only, because the transition metal at the surface of the Pt-skeleton structure was leached out and the Pt-skin structure remained stable. Both structures exhibited different electronic properties compared to polycrystalline, described by the d-band center of the crystal, which led to a change of the potential dependent adsorption of oxygenated species and as a consequence to an enhancement of the catalytic activity for the oxygen reduction by a factor up to three. The high-surface area Pt-alloys exhibited a similar improvement of the reactivity, but unfortunately also the total loss of the transition metal from the surface layers was found due to the undesired leaching process.

The results of this work provide a new perception of known effects in electrocatalysis and a better understanding of the fundamental aspects in particular for important practical fuel cell reactions. Furthermore these novel explanations offer promising pathways for the improvement of the electrocatalytic properties of the described practical materials.

Zusammenfassung in Deutsch

Das Ziel dieser Arbeit war die Untersuchung der CO Oxidations- und der Sauerstoffreduktionsreaktion an verschiedensten Typen von Platinelektroden, um das Verständniss für diese wichtigen Brennstoffzellenreaktionen zu verbessern. Die Reaktionen wurden zuerst anhand von Einkristall- und Polykristallmodelsystemen ausgeführt, um die Wichtigkeit der Grundlagenforschung hervorzuheben, und anschließend mit den Reaktionen von Nanokatalysatoren, die in der Praxis eingesetzt werden, verglichen. Unter Anwendung sowohl elektrochemischer Analyseverfahren wie in-situ FTIRAS und normaler Zyklovoltammetrie, als auch Oberflächenuntersuchungsmethoden wie TEM, AES, UPS und LEISS, konnten neue Einsichten in die Reaktionsmechanismen, sowie in die Effekte, die von der Partikelgröße bestimmt sind, gewonnen werden. Basierend auf den Ergebnissen an Systemen mit reinem Pt, konnten komplizierter aufgebaute Mischkatalysatoren wie vielversprechende Platinlegierungen erfolgreich untersucht werden.

(1) Die *Oxidation einer adsorbierten CO Monolage* (CO-Stripping) wurde an den Pt Modellsystemen und an Pt Nanopartikeln in einer Größe von 1 bis 30nm untersucht. Die besondere Rolle von Defektgitterstellen, Stufen- und Kantenlagen für die katalytischen Eigenschaften als Adsorptionsplätze für reaktives OH_{ad} wurde mittels FTIRAS Experimenten nachgewiesen, indem die Schwingungsfrequenz von „a-top" CO sowie die begleitende Entwicklung der asymmetrischen O-C-O Stretchbande von gelöstem CO_2 bestimmt wurde. Für Pt Einkristalle ist die Reaktion von der Anzahl der Stufen und Kanten abhängig, die durch die Art der Vorbehandlung der Elektrode beeinflusst werden kann. Mit „CO annealing" wird in jedem Fall die Zahl dieser Unregelmäßigkeiten verringert, wodurch diese Oberflächen nicht so aktiv für die Oxidation einer CO Monolage sind wie die mit einer Vorbehandlung durch „oxide annealing" erhalten werden. Für Pt Cluster konnte mittels TEM Analyse gezeigt werden, dass diese keine perfekten cubo-Oktaeder sind und dass große Partikel rauhere Oberflächen aufweisen als kleinere Partikel, welche einigermaßen ebene (111) Kristallflächen besitzen. Defekte spielen eine signifikante Rolle beim „CO-clustering" auf Nanopartikeln - sie können eine Veränderung des

124

lokalen Oberflächenbedeckungsgrades und damit eine ungewöhnliche Abweichung der CO Streckschwingung von dem sonst vorherrschenden Stark-tuning Verhalten herbeiführen. Die beobachten Frequenzabweichungen werden von der CO_2 Bildung begleitet, die mit der Anzahl der Defektstellen auf den Nanopartikeln zunimmt, d.h. 1nm $\leq$ 2nm < 5nm << 30nm. Die katalytische Aktivität für die Oxidation einer adsorbierten Monolage an CO ist haupsächlich von der Fähigkeit der Dissoziation von Wasser und der Bildung von OH_{ad} an Stufen, Kanten und Defekten auf der Oberfläche abhängig.

(2) Der *Effekt der Clustergröße* auf die Adsorption von OH_{ad}, die kontinuierliche anodische Oxidation von CO und die kathodische Sauerstoffreduktion wurden auf Pt Nanokatalysatoren in perchlorsaurem Elektrolyten untersucht. Durch Messungen der CO Verdrängungsladung bei konstanten Potentialen konnte die Oberflächenladungsdichte gegen das Verdrängungspotential aufgetragen werden. Daraus konnte das wichtige Nullladungspotential (pztc) abgelesen werden, welches sich bei Verkleinerung der Partikelgröße von 30nm auf 1nm um ungefähr 35mV zu negativeren Potentialen verschiebt. Dies bedeutet, dass die Adsorptionsenergie von OH_{ad} sich erhöht, i.e. bei konstantem Potential nimmt die Oberflächenbedeckung mit OH_{ad} mit abnehmender Clustergröße zu, wodurch wiederum die katalytischen Reaktionen beeinflusst werden. Der Einfluss der Verschiebung des OH_{ad} Adsorptionspotential wird anhand der kontinuierlichen CO Oxidation, bei der OH_{ad} ein notwendiges Edukt ist und die Reaktion beschleunigt, sowie der Sauerstoffreduktion, da es aktive Oberflächenplätze blockieren kann und dadurch die Reaktion behindert wird, demonstriert.

(3) Die *Platinlegierungen* wurden im letzten Kapitel als aussichtsreiche Systeme für die zukünftige Entwicklung von Brennstoffzellenkatalystatoren vorgestellt. Anhand des Beispieles von Pt_3Fe wurde gezeigt, dass für Pt-Legierungen zwei verschiedene Oberflächenzusammensetzungen durch unterschiedliche Vorbehandlung der Legierung erzeugt werden können, nämlich „Pt-skeleton" (Pt-Skelett) und „Pt-skin" (Pt-Haut). Zyklovoltammetrie und LEISS zeigten, dass in beiden Fällen nach dem Eintauchen in den sauren Elektrolyten die Oberfläche nur noch aus Pt bestand, wobei das Legierungsmetall aus den Oberflächenschichten des Pt-skeletons herausgelöst wurde, die Struktur des Pt-skin's hingegen stabil blieb. Die elektronischen Eigenschaften beider Strukturen waren anders als die des polykristallinen Pt's, bestätigt durch die unterschiedlichen Zentren der d-Bänder der Kristalle, was zu einer

Veränderung der potentialabhängigen Adsorption von OH_{ad} und dadurch zu einer Verbesserung der katalytischen Aktivität für die Sauerstoffreduktion um einen Faktor bis zu drei führte. Auch die Reaktivität der Nanokatalysatoren aus Platinlegierungen war in einem ähnlichen Ausmass besser als die reiner Pt-Nanokatalysatoren, jedoch ist bei ihnen ebenfalls die unerwünschte korrosive Auflösung des Legierungsmetalls aus der Clusteroberfläche zu berücksichtigen.

Die vorliegenden Ergebnisse der Arbeit liefern neue Erkenntnisse zur Deutung bekannter fundamentaler Effekte und ermöglichen ein vertieftes Verständnis der Funktionsweise von Elektrokatalysatoren im besonderen für Brennstoffzellenreaktionen. Ferner werden durch diese neuen Erklärungen vielversprechende Wege für eine Verbesserung der Wirksamkeit der beschriebenen Materialien aufgezeigt.

Reference List

1. Mayrhofer, K. J. J. Stromdichteverteilung in PEM Brennstoffzellen. TU Vienna, 2005.

2. Berzelius J. J. *Jahresberichte aus der Chemie*, 15 ed.; 1836; p. 237.

3. Kobosev, N.; Monblanova, W. *Acta Physicochim.URSS* **1934**, *1*, 611.

4. *Nature* **1963**, 883.

5. Bockris, J. O. M.; Reddy, A. K. N. *Modern Electrochemistry*, Plenum Press, New York: 1970.

6. Somorjai, G. A. *Introduction to Surface Chemistry and Catalysis*, Wiley, New York: 1994.

7. Rodriguez, J. A. and Goodman, D. W. "Surface Science Reports," 1991.

8. Markovic, N. M.; Ross, J. *Surface Science Reports* **2002**, *45*, 117-229.

9. Bewick, A.; Kunimatsu, K. *Surface Science* **1980**, *101*, 131-138.

10. Binnig, G.; Rohrer, H. *Helv.Phys.Acta* **1982**, 726.

11. *Scanning Tunneling Microscopy and Spectroscopy - Theory, Techniques and Applications*, VCH, New York: 1993.

12. Conway, B. E.; Bockris, J. O. 'M. *The Journal of Chemical Physics* **1957**, *26*, 532-541.

13. Parsons, R. *Trans.Faraday Soc.* **1958**, 1053.

14. Gerischer. *H.Bull.Soc.Chim.Belg.* **1958**, 506.

15. Trasatti, S. *Journal of Electroanalytical Chemistry* **1972**, *39*, 163-184.

16. Trasatti, S. *Surface Science* **1995**, *335*, 1-9.

17. Kinoshita, K. *Electrochemical Oxygen Technology*, Wiley, New York: 1992.

18. Wroblowa, H. S.; Yen, C. P.; Razumney, G. *Journal of Electroanalytical Chemistry* **1976**, *69*, 195-201.

19. Hoare J. P. *Encyclopedia of Electrochemistry of the Elements*, New York, 1982.

20. Appleby, A. J. *Catal.Rev.* **1970**, *4*, 221.

21. Tarasevich M. R.; Sadkowski, A.; Yeager, E. *Comprehensive Treatise of Electrochemistry*, Plenum Press, New York: 1983.

22. Markovic, N. M.; Gasteiger, H. A.; Grgur, B. N.; Ross, P. N. *Journal of Electroanalytical Chemistry* **1999**, *467*, 157-163.

23. Markovic, N. M.; Adzic, R. R.; Cahan, B. D.; Yeager, E. B. *Journal of Electroanalytical Chemistry* **1994**, *377*, 249-259.

24. Markovic, N. M.; Gasteiger, H. A.; Ross, P. N. *Journal of Physical Chemistry* **1995**, *99*, 3411-3415.

25. Perez, J.; Villullas, H. M.; Gonzalez, E. R. *Journal of Electroanalytical Chemistry* **1997**, *435*, 179-187.

26. Ross P. N. *Handbook of Fuel Cells*, John Wiley & Sons: 2003; Chapter 35.

27. Zurawski, D.; Wasberg, M.; Wieckowski, A. *J.Phys.Chem.* **1990**, *94* , 2076.

28. Lucas, C. A.; Markovic, N. M.; Ross, P. N. *Surface Science* **1999**, *425*, L381-L386.

29. Villegas, I.; Weaver, M. J. *J.Phys.Chem.* **1994**, *101*, 1648.

30. Markovic, N. M.; Grgur, B. N.; Lucas, C. A.; Ross, P. N. *Journal of Physical Chemistry B* **1999**, *103*, 487-495.

31. Kita, H.; Naohara, H.; Nakato, T.; Taguchi, S.; Aramata, A. *Journal of Electroanalytical Chemistry* **1995**, *386*, 197-206.

32. Wieckowski, A.; Rubel, M.; Gutierrez, C. *Journal of Electroanalytical Chemistry* **1995**, *382*, 97-101.

33. Lebedeva, N. P.; Koper, M. T. M.; Herrero, E.; Feliu, J. M.; van Santen, R. A. *Journal of Electroanalytical Chemistry* **2000**, *487*, 37-44.

34. Markovic, N. M.; Lucas, C. A.; Grgur, B. N.; Ross, P. N. *Journal of Physical Chemistry B* **1999**, *103*, 9616-9623.

35. Markovic, N. M.; Schmidt, T. J.; Grgur, B. N.; Gasteiger, H. A.; Behm, R. J.; Ross, P. N. *Journal of Physical Chemistry B* **1999**, *103*, 8568-8577.

36. Vayenas C. G.; Pliangos, C.; Brosda, S.; Tsiplakides, D. *Catalysis and Electrocatalysis on Nanoparticle Surfaces*; Marcel Dekker, Inc.: New York, 2003; Chapter 19, p. 667.

37. Henry, C. R. *Surface Science Reports* **1998**, *31*, 231-325.

38. Arico A. S.; Antonucci, V.; Antonucci, P. L. *Catalysis and Electrocatalysis on Nanoparticle Surfaces*; Marcel Dekker, Inc.: New York, 2003; Chapter 17, p. 613.

39. Bregoli, L. J. *Electrochimica Acta* **1978**, *23*, 489-492.

40. Sattler, M. L.; Ross, P. N. *Ultramicroscopy* **1986**, *20*, 21-28.

41. Kinoshita, K. *J.electrochem.Soc.* **1990**, *137*, 845.

42. Markovic, N. M.; Gasteiger, H. A.; Ross, P. N. *J.electrochem.Soc.* **1997**, *144*, 1591.

43. Watanabe, M.; Sei, H.; Stonehart, P. *Journal of Electroanalytical Chemistry* **1989**, *261*, 375-387.

44. Giordano, N.; Passalacqua, E.; Pino, L.; Arico, A. S.; Antonucci, V.; Vivaldi, M.; Kinoshita, K. *Electrochimica Acta* **1991**, *36*, 1979-1984.

45. Takasu, Y.; Ohashi, N.; Zhang, X.-G.; Murakami, Y.; Minagawa, H.; Sato, S.; Yahikozawa, K. *Electrochimica Acta* **1996**, *41*, 2595-2600.

46. Kuhrt, C.; Harsdorff, M. *Surface Science* **1991**, *245*, 173-179.

47. Mukerjee, S.; McBreen, J. *Journal of Electroanalytical Chemistry* **1998**, *448*, 163-171.

48. Gasteiger, H. A.; Markovic, N. M.; Ross, P. N. *Journal of Physical Chemistry* **1995**, *99*, 8290-8301.

49. Wang, K.; Gasteiger, H. A.; Markovic, N. M.; Ross, P. N. *Electrochimica Acta* **1996**, *41*, 2587-2593.

50. Friedrich, K. A.; Henglein, F.; Stimming, U.; Unkauf, W. *Colloids and Surfaces A: Physicochemical and Engineering Aspects* **1998**, *134*, 193-206.

51. Friedrich, K. A.; Henglein, F.; Stimming, U.; Unkauf, W. *Electrochimica Acta* **2000**, *45*, 3283-3293.

52. Rice, C.; Tong, Y.; Oldfield, E.; Wieckowski, A.; Hahn, F.; Gloaguen, F.; Leger, J. M.; Lamy, C. *Journal of Physical Chemistry B* **2000**, *104*, 5803-5807.

53. Park, S.; Wasileski, S. A.; Weaver, M. J. *Journal of Physical Chemistry B* **2001**, *105*, 9719-9725.

54. Dunietz, B. D.; Markovic, N. M.; Ross, P. N.; Head-Gordon, M. *Journal of Physical Chemistry B* **2004**, *108*, 9888-9892.

55. Cherstiouk, O. V.; Simonov, P. A.; Savinova, E. R. *Electrochimica Acta* **2003**, *48*, 3851-3860.

56. Cherstiouk, O. V.; Simonov, P. A.; Zaikovskii, V. I.; Savinova, E. R. *Journal of Electroanalytical Chemistry* **2003**, *554-555*, 241-251.

57. MUKERJEE, S.; Srinivasan, S.; SORIAGA, M. P.; MCBREEN, J. *Journal of the Electrochemical Society* **1995**, *142*, 1409-1422.

58. Toda, T.; Igarashi, H.; Uchida, H.; Watanabe, M. *J.electrochem.Soc.* **1999**, *146*, 3750-3756.

59. Stamenkovic, V.; Schmidt, T. J.; Ross, P. N.; Markovic, N. M. *J.Phys.Chem.* **2002**, *106*, 11970-11979.

60. Stamenkovic, V.; Schmidt, T. J.; Ross, P. N.; Markovic, N. M. *Journal of Electroanalytical Chemistry* **2003**, *554-555*, 191-199.

61. Gasteiger, H. A.; Markovic, N. M.; Ross, P. N. *Journal of Physical Chemistry* **1995**, *99*, 16757-16767.

62. Stamenkovic, V.; Arenz, M.; Blizanac, B. B.; Mayrhofer, K. J. J.; Ross, P. N.; Markovic, N. M. *Surface Science* **2005**, *576*, 145-157.

63. Hammer, B.; Norskov, J. K. *Surface Science* **1995**, *343*, 211-220.

64. Hammer B.; Norskov, J. K. Kluwer, Netherlands: 1997; pp. 285-351.

65. Norskov, J. K.; Rossmeisel, J.; Logadottir, A.; Lindqvist, L.; Kitchin, J. R.; Bligaard, T.; Jonsson, H. *J.Phys.Chem.B* **2004**, *108*, 17886-17892.

66. Kitchin, J. R.; Norskov, J. K.; Barteau, M. A.; Chen, J. G. *The Journal of Chemical Physics* **2004**, *120*, 10240-10246.

67. Bard, A. J.; Faulkner, L. R. *Electrochemical Methods*, 2nd ed.; John Wiley & Sons, Inc.: 2000.

68. Gileadi, E. *Electrode Kinetics for Chemical Engineers and Material Scientists*, VCH-Publisher, London (UK): 1993.

69. Pleskov, Y. V.; Filinovskij, V. Y. *The Rotating Disc Electrode*, Consultant Bureau, New York: 1976.

70. Levich, V. G. "Physicochemical Hydrodynamics"; 1962. Ref Type: Conference Proceeding

71. Albery, W. J.; Hitchman, M. L. *Ring Disk Electrodes*, Claredon Press, Oxford: 1971.

72. Greef, R.; Peat, R.; Peter, L. M.; Pletcher, D.; Robinson, J. *Instrumental methods in electrochemistry*, Ellis Horwood: 1990.

73. Nicholsen R. S. 37 ed.; 1965; Chapter 11, p. 1351.

74. Beden, B.; Lamy, C. *Infrared Reflectance Spectroscopy in Spectroelectrochemistry-theory and practice*, Plenum Press: 1988.

75. Bishop, D. M. *Journal of Chemical Physics* **1993**, *99*, 4875.

76. Lambert, D. K. *Electrochimica Acta* **1996**, *41*, 623-630.

77. Iwasita, T. and Nart, F. C. Progress in Surface Science 55[4], 271-340. 1997. 1997. Ref Type: Journal (Full)

78. Nichols R. *Adsorption of molecules at metal electrodes*, VCH Weinheim: 1992.

79. Flegler, S. L.; Heckman, J. W.; Klomparens, K. L. *Scanning and transmission electron microscopy : an introduction*, W.H. Freeman, New York: 1993.

80. Graef, M. *Introduction to Conventional Transmission Electron Microscopy*, 2003.

81. Park R. L. *Methods of Experimental Physics*, Academic Press, Inc: 1985; Chapter 4.

82. Werner, W. S. M.; Tilinin, I. S. *Applied Surface Science* **1993**, *70-71*, 29-34.

83. Zhou, X.-L.; Zhu, X.-Y.; White, J. M. *Surface Science Reports* **1991**, *13*, 73-220.

84. Niemantsverdriet, J. W. *Spectroscopy in Catalysis - An introduction*, VCH - Weinheim: 1993.

85. Briggs, D.; Seah, M. P. *Practical Surface Analysis*, John Wiley & Sons, Chichester: 1990.

86. Ross P. N. *Electrocatalysis*, Wiley, VCH: 1998.

87. Niehus H. *Practical Surface Analysis, Vol.: 2*; Wiley, Chichester: 1992; Chapter 9.

88. Niehus, H., Heiland, W., and Taglauer, E. "Surface Science Report," 1993.

89. Boudart, M. *Topics in Catalysis* **2000**, *13*, 147-149.

90. Van Hove, M. A.; Weinberg, W. H.; Chan, C.-M. *Low-Energy Electron Diffraction: Experiment, Theory and Structural Determination*, Springer Verlag: Heidelberg, Berlin, 1986.

91. Van Hove M. A. *Structure of Electrified Interfaces*, VCH Publishers, Inc.: Weinheim, Germany, 1993; Chapter 1, pp. 1-34.

92. Itaya, K. *Progress in Surface Science* **1998**, *58*, 121-247.

93. Samant, M. G.; Toney, M. F.; Borges, G. L.; Blurton, K. F.; Melroy, O. R. *J.Phys.Chem.* **1988**, *92*, 220-225.

94. Clavilier, J. *Journal of Electroanalytical Chemistry* **1980**, *107*, 211-216.

95. Kolb, D. M. *Progress in Surface Science* **1996**, *51*, 109-173.

96. Ross P. N. *Structure of Electrified Interfaces*, VCH Publishers, Inc.: Weinheim, Germany, 1993; Chapter 2, pp. 35-64.

97. Somorjai, G. A. *Chemistry in Two-Dimensions: Surfaces*, Cornell University Press: Ithaca, New York, 1981.

98. Hamelin A. *Modern Aspects of Electrochemistry*, eds. Plenum: New York, 1985; Chapter 1, p. 1.

99. Adzic R. R. *Modern Aspects of Electrochemistry*, eds. Plenum: New York, 1990; p. 163.

100. Lebedeva, N. P.; Koper, M. T. M.; Feliu, J. M.; van Santen, R. A. *Journal of Physical Chemistry B* **2002**, *106*, 12938-12947.

101. Arenz, M. Model electrodes for electrocatalysis: Ultrathin palladium films on Pt(111). Universitaet Bonn, 2002.

102. Markovic, N. M.; Hanson, M.; McDougall, G.; Yeager, E. *Journal of Electroanalytical Chemistry* **1986**, *214*, 555-566.

103. Clavilier, J.; Armand, D.; Sun, S. G.; Petit, M. *Journal of Electroanalytical Chemistry* **1986**, *205*, 267-277.

104. Wagner, F. T.; Ross, J. *Journal of Electroanalytical Chemistry* **1988**, *250*, 301-320.

105. Feddrix, F. H.; Yeager, E. B.; Cahan, B. D. *Journal of Electroanalytical Chemistry* **1992**, *330*, 419-431.

106. Yoshima, K.; Song, M.; Ito, M. *Surf.Sci.* **2005**, *368*, 389.

107. Ertl, G.; Neumann, M.; Streit, K. M. *Surface Science* **1977**, *64*, 393-410.

108. Bergelin, M.; Feliu, J. M.; Wasberg, M. *Electrochimica Acta* **1998**, *44*, 1069-1075.

109. Bergelin, M.; Herrero, E.; Feliu, J. M.; Wasberg, M. *Journal of Electroanalytical Chemistry* **1999**, *467*, 74-84.

110. Arenz, M.; Mayrhofer, K. J. J.; Stamenkovic, V. R.; Blizanac, B. B.; Tada, T.; Markovic, N. M.; Ross, P. N. *Journal of the American Chemical Society* **2005**, *127*, 6819-6829.

111. Kibler, L. A.; Cuesta, A.; Kleinert, M.; Kolb, D. M. *Journal of Electroanalytical Chemistry* **2000**, *484*, 73-82.

112. Castell, R.; Reiff, S.; Drachsel, W.; Block, J. H. *Surface Science* **1997**, *377-379*, 770-774.

113. Kitamura, F.; Takahashi, M.; Ito, M. *Surface Science* **1989**, *223*, 493-508.

114. Chang, S. C.; Weaver, M. J. *Surface Science* **1990**, *238*, 142-162.

115. Schmidt, T. J. Electrocatalysis of Low-Temperature Fuel Cell Reactions. University Ulm, Germany, 2000.

116. Appleby, A. J. *Journal of Electroanalytical Chemistry* **1993**, *357*, 117-179.

117. Kinoshita, K. *Electrochemical Oxygen Technology*, Wiley and Sons, Inc.: New York, 1990.

118. Adzic R. R. *Electrocatalysis*; Wiley-VCH, Inc.: 1998; Chapter 5, pp. 197-242.

119. Damjanovic, A.; Brusic, V. *Electrochimica Acta* **1967**, *12*, 615-628.

120. Sepa, D. B.; Vojnovic, M. V.; Damjanovic, A. *Electrochimica Acta* **1981**, *26*, 781-793.

121. Sepa, D. B.; Vojnovic, M. V.; Vracar, L.; Damjanovic, A. *Electrochimica Acta* **1987**, *32*, 129-134.

122. Tarasevich, M. R.; Vilinskaya, V. S. *Elektrokhimiya* **1973**, *9*.

123. Yeager E. B.; Razaq, M.; Gervasio, D.; Razaq, A.; Tryk, D. *Structural Effects in Electrocatalysis and Oxygen Electrochemistry*, Proc vol. *92-11*; The Electrochemical Society. Inc: Pennington NJ, 1992; p. 440.

124. El Kadiri, F.; Faure, R.; Durand, R. *Journal of Electroanalytical Chemistry* **1991**, *301*, 177-188.

125. Gloaguen, F.; Andolfatto, F.; Durand, R.; Ozil, P. *Journal of Applied Electrochemistry* **1994**, *24*, 863-869.

126. Gojkovic, S. L.; Zecevic, S. K.; Savinell, R. F. *Journal of the Electrochemical Society* **1998**, *145*, 3713-3720.

127. Gloaguen, F.; Convert, P.; Gamburzev, S.; Velev, O. A.; Srinivasan, S. *Electrochimica Acta* **1998**, *43*, 3767-3772.

128. Perez, J.; Gonzalez, E. R.; Ticianelli, E. A. *Electrochimica Acta* **1998**, *44*, 1329-1339.

129. Schmidt, T. J.; Gasteiger, H. A.; Staeb, O. D.; Urban, P. M.; Kolb, D. M.; Behm, R. J. *Journal of the Electrochemical Society* **1998**, *145*, 2354-2358.

130. Paulus, U. A.; Schmidt, T. J.; Gasteiger, H. A.; Behm, R. J. *Journal of Electroanalytical Chemistry* **2001**, *495*, 134-145.

131. Schmidt T. J.; Gasteiger, H. A. *Handbook of Fuel Cells - Fundamentals, Technology and Applications*, Wiley: 2003; Chapter 22, p. 316.

132. Gasteiger, H. A.; Kocha, S. S.; Sompalli, B.; Wagner, F. T. *Applied Catalysis B: Environmental* **2005**, *56*, 9-35.

133. Debe M. K. *Handbook of Fuel Cells - Fundamentals, Technology and Applications*, John Wiley & Sons: 2002; pp. 576-589.

134. Steinrueck, H. P.; Pesty, F.; Zhang, L.; Madey, T. E. *Phys.Rev.B* **1995**, *51*, 2427.

135. Libuda, J.; Sandell, A.; Baumer, M.; Freund, H.-J. *Chemical Physics Letters* **1995**, *240*, 429-434.

136. Stamenkovic, V. R.; Arenz, M.; Ross, P. N.; Markovic, N. M. *J.Phys.Chem.B* **2004**, 17915-17920.

137. Kinoshita K.; Stonehart, P. *Modern Aspects of Electrochemistry*, Plenum Press, New York: 1977; Chapter 4, p. 183.

138. Montejano-Carrizales, J. M.; Aguilera-Granja, F.; Moran-Lopez, J. L. *Nanostructured Materials* **1997**, *8*, 269-287.

139. Mayrhofer, K. J. J.; Blizanac, B. B.; Arenz, M.; Stamenkovic, V. R.; Ross, P. N.; Markovic, N. M. *J.Phys.Chem.B* **2005**, *109*, 14433-14440.

140. Markovic N. M.; Radmilovic, V.; Ross, P. N. *Catalysis and Electrocatalysis at Nanoparticle Surfaces*, Marcel Dekker: New York, 2003.

141. Markovic, N. M.; Grgur, B. N.; Lucas, C. A.; Ross, P. N. *Surface Science* **1997**, *384*, L805-L814.

142. Maillard, F.; Eikerling, M.; Cherstiouk, O. V.; Schreier, S.; Savinova, E.; Stimming, U. *Faraday Discussions* **2004**, *125*, 357-377.

143. Frumkin, A. N.; Petrii, O. A. *Electrochimica Acta* **1975**, *20*, 347-359.

144. Trasatti S. *Advances in Electrochemistry and Electrochemical Engineering*, Wiley, New York: 1977; p. 221.

145. Weaver, M. J. *Langmuir* **1998**, *14*, 3932-3936.

146. Climent V.; Gomez, R.; Orts, J. M.; Rodes, A.; Aldaz, A.; Feliu, J. M. *Interfacial Electrochemistry*, Marcel Dekker, New York: 1999; p. 463.

147. Cuesta, A. *Surface Science* **2004**, *572*, 11-22.

148. Climent, V.; Gomez, R.; Feliu, J. M. *Electrochimica Acta* **1999**, *45*, 629-637.

149. Climent, V.; Attard, G. A.; Feliu, J. M. *Journal of Electroanalytical Chemistry* **2002**, *532*, 67-74.

150. *Topics in Applied Physics - Photoemission in Solids I*, Springer Verlag: Berlin, 1978.

151. Frumkin A. N.; Petrii, O. A.; Damaskin, B. B. *Comprehensive Treatise of Electrochemistry*; Plenum Press: New York, 1980; p. 221.

152. Plieth, W. J. *J.Phys.Chem.* **1982**, *86*, 3166-3170.

153. Jusys, Z.; Kaiser, J.; Behm, R. J. *Physical Chemistry Chemical Physics* **2001**, *3*, 4650-4660.

154. Stamenkovic, V. R.; Chou, K. C.; Somorjai, G. A.; Ross, P. N.; Markovic, N. M. *J.Phys.Chem.B* **2005**, *109*, 678-680.

155. Friedrich, K. A.; Henglein, F.; Stimming, U.; Unkauf, W. *Electrochimica Acta* **2001**, *47*, 689-694.

156. Rice, C.; Tong, Y.; Oldfield, E.; Wieckowski, A.; Hahn, F.; Gloaguen, F.; Leger, J.-M.; Lamy, C. *J.Phys.Chem.B* **2000**, *104*, 5803-5807.

157. Severson, M. W.; Stuhlmann, C.; Villegas, I.; Weaver, M. J. *Journal of Chemical Physics* **1995**, *103*, 9832-9843.

158. Severson, M. W.; Weaver, M. J. *Langmuir* **1998**, *14*, 5603-5611.

159. Hammer, B.; Norskov, J. K. *Catalysis Letters* **1997**, *46*, 31-35.

160. Shubina, T. E.; Koper, M. T. M. *Electrochimica Acta* **2002**, *47*, 3621-3628.

161. Chang, S. C.; Roth, J. D.; Weaver, M. J. *Surface Science* **1991**, *244*, 113-124.

162. McIntyre, B. J.; Salmeron, M.; Somorjai, G. A. *Surface Science* **1995**, *323*, 189-197.

163. Ataka, K.; Yotsuyanagi, T.; Osawa, M. *J.Phys.Chem.* **1996**, *100*, 10664-10672.

164. Arenz, M.; Stamenkovic, V.; Schmidt, T. J.; Wandelt, K.; Ross, P. N.; Markovic, N. M. *Surface Science* **2003**, *523*, 199-209.

165. Grgur, B. N.; Markovic, N. M.; Ross, P. N. *J.Phys.Chem.B* **1998**, *102*, 2494-2501.

166. Boudart, M. *Advances in Catalysis* **1969**, 153.

167. Su, X.; Cremer, P. S.; Shen, Y. R.; Somorjai, G. A. *Journal of the American Chemical Society* **1997**, *119*, 3994-4000.

168. Lee, W. T.; Ford, L.; Blowers, P.; Nigg, H. L.; Masel, R. I. *Surface Science* **1998**, *416*, 141-151.

169. Burnett, D. J.; Capitano, A. T.; Gabelnick, A. M.; Marsh, A. L.; Fischer, D. A.; Gland, J. L. *Surface Science* **2004**, *564*, 29-37.

170. Conway, B. E. *Progress in Surface Science* **1995**, *49*, 331-452.

171. Niehus, H.; Comsa, G. *Surface Science* **1980**, *93*, L147-L150.

172. Golchet, A.; White, J. M. *Journal of Catalysis* **1978**, *53*, 266-279.

173. Segner, J.; Campbell, C. T.; Doyen, G.; Ertl, G. *Surface Science* **1984**, *138*, 505-523.

174. Ertl, G. *Journal of Molecular Catalysis A: Chemical* **2002**, *182-183*, 5-16.

175. Inaba, M.; Yamada, H.; Tokunaga, J.; Tasaka, A. *Electrochemical and Solid State Letters* **2004**, *7*, A474-A476.

176. Chen, S. L.; Kucernak, A. *J.Phys.Chem.B* **2004**, *108*, 3262-3276.

177. Paulus, U. A.; Wokaun, A.; Scherer, G. G.; Schmidt, T. J.; Stamenkovic, V.; Radmilovic, V.; Markovic, N.; Ross, P. N. *J.Phys.Chem.B* **2002**, *106*, 4181-4191.

178. Antolini, E.; Passos, R. R.; Ticianelli, E. A. *Electrochimica Acta* **2002**, *48*, 263-270.

179. Vasiliev, M. A. *Journal of Physics D: Applied Physics* **1997**, 3037-3070.

180. Watson, P. R.; Van Hove, M. A.; Herman, K. *Atlas of Surface Structure*, ACS Publications: Washington DC, 1995.

181. Gasteiger, H. A.; Ross, P. N.; Campbell, C. T. *Surf.Sci.* **1993**, *293*, 67-80.

182. Beccat, P.; Gauthier, Y.; Baudoing-Savois, R.; Bertolni, J. C. *Surface Science* **1990**, *238*, 105-118.

183. Gauthier, Y.; Baudoing-Savois, R.; Bugnard, J. M.; Bardi, U.; Atrei, A. *Surface Science* **1992**, *276*, 1-11.

184. Gauthier, Y. *Surface Review and Letters* **1996**, *3*, 1663-1689.

185. Bardi, U.; Atrei, A.; Zanazzi, E.; Rovida, G.; Ross, P. N. *Vacuum* **1990**, *41*, 437-440.

186. Taglauer, E. *Appl.Phys.A* **1985**, *38*, 161-170.

187. Greeley, J.; Norskov, J. K.; Mavrikakis, M. *Annual Review of Physical Chemistry* **2002**, *53*, 319-348.

188. Damjanovic, A.; Sepa, D. B. *Electrochimica Acta* **1990**, *35*, 1157-1162.

Curriculum vitae:

I was born on the 30. December 1977 in Villach, Austria, 1984 I entered elementary school and four years later I changed to the Perau Grammar School in Villach. I stayed there for eight years and graduated in 1996 (the so called "Abitur") with honours. Since the school offered plenty of elective courses, I made use of these options to improve both mentally and physically. Besides others I attended soccer, chess and extra maths and chemistry classes, which were an excellent preparation for University.

After my Abitur I jobbed for two months at the company OMYA in a quality assurance laboratory, where I conducted examinations on rock-drill samples and controlled the product quality.

Yet the same year I enrolled at the Technical University of Vienna "Technical Chemistry" and "Business Informatics". Soon I realized that Chemistry is much more interesting to me, but especially the lab courses were pretty time consuming, consequently I had to give up Informatics. After three years I finished with the first part of my studies, the so-called 1.Diplomprüfung which is comparable to a Bachelor degree, with an extensive and solid base-knowledge in theoretical and practical chemistry and generally in technical-scientific subjects.

In summer of 1998 I did a three-month internship at an analytical-research laboratory of the Chemetall GmbH in Frankfurt, Germany. The focus at the headquarter facility of this international company is research on various areas of chemistry, for instance glas, polymers, metal surfaces, Li – organic molecules. My task in the analytical lab was to optimise some existing analytical methods on the HPLC and HPTLC and to assist various research groups. Due to the close cooperation with the different groups I was always familiar with their projects and could therefore gain some experience on industrial research. Moreover I learned a lot about different analytical methods like GC-MS or NMR, since the laboratory was very well equipped.

For the school year of 1999/2000 I obtained a place in the TransAtlantic Scientific Student Exchange Program (TASSEP), and decided to attend graduate courses at the University of Texas

in Austin. There I specialized in Physical and Analytical Chemistry and took courses like "Quantum Mechanics" or " Statistical Thermodynamics" besides others. Moreover I worked half the day in the research group for surface chemistry, where I learned a lot about research work at University. The most interesting of all however was the "Electrochemistry" course by Dr. A.J.Bard, one of the most qualified and acknowledged electrochemists. He did really arouse my enthusiasm.

Back from Austin, I worked an internship for three month at Ballard Power Systems in Nabern, Germany. This company is one of the worldwide leaders in the fuel cell technology for mobile application. My actual main assignment was the optimisation of a program for data acquisition in Delphi, which should give the operator a fast survey of the data of a working fuel cell and enable an easier evaluation afterwards. Since this task could be executed in less than the predetermined time, I was also engaged in other general subjects concerning fuel cells. Thus I supported the electronic engineers and programmers in my group with electrochemical issues, and besides I also tested various new temperature measuring methods for fuel cells.

From October 2000 till June 2001 I completed my last courses at University that I needed for my Masters degree. In July I started with the work on my Masters Thesis, again at Ballard Power Systems in Germany, but this time in the "Membrane-Electrode-Assembly" group. One of their focuses in research at that time were the lifetime of Membrane-Electrode-Assemblies (MEA's) of Polymer-Electrolyte-Membrane fuel cells (PEMFC's). Since measuring the lifetime is usually highly time consuming, Ballard developed the so-called "Current Mapping". With this analytical device one can see the current density distribution over the MEA of a working fuel cell. According to preceding investigations, an inhomogeneous current density distribution shortens the lifetime of a MEA drastically. My job was to analyse my self-produced MEA's under various operation conditions with the Current Mapping tool, and interpret the obtained data. Afterwards I tried to get more homogeneous current density distributions by changing the structure of the MEA. Since I did everything by myself, beginning with the producing of the MEA's till the interpretation of the data, I could improve my knowledge on fuel cell technology a lot and I gained very valuable hands-on experience.

In June 2002 I graduated with honours from the TU Vienna with a Master in Technical Chemistry. In fall I enrolled again at the TU Vienna for my PhD in Technical Sciences, which was supervised by Univ. Prof. DI Dr. Fabjan from the Institute for Chemical Technologies and Analysis. After attending the courses necessary for specialization in the first semester, I started to work on my thesis "Oxygen Reduction and Carbon Monoxide Oxidation on Pt - from Model to Real Systems for Fuel Cell Electrocatalysis" at the Lawrence Berkeley National Laboratory in Berkeley, California, under the excellent guidance of P.N. Ross and N.M. Markovic. In their internationally best-known research group I could independently work on the ideas that came up during my Masters Thesis in an extended time frame. The results were presented here in this work and additionally in several peer-reviewed papers, which are listed below. After my return to Vienna I joined the Austrian Army to do my compulsory military service at the NBC Defenseschool in Korneuburg for eight months. Currently I act as a „MilwEx", i.e. a military-scientific expert, and work on several chemistry and chemical warfare related topics, such as the preparation of a textbook on chemical weapons for an MBA course.

My aim for the near future is, once I am done with the defence of the thesis and the military service in February 2006, to apply for an independent junior research scholarship at an international recognized institute to implement my ideas gained over the last couple of years.

Reference List

a) Arenz, M.; Mayrhofer, K. J. J.; Stamenkovic, V. R.; Blizanac, B. B.; Tada, T.; Markovic, N. M.; Ross, P. N. *Journal of the American Chemical Society* **2005**, *127*, 6819-6829.

b) Mayrhofer, K. J. J.; Arenz, M.; Blizanac, B. B.; Stamenkovic, V. R.; Markovic, N. M.; Ross, P. N. *Electrochimica Acta* **2005**, *50*, 5144-5154.

c) Mayrhofer, K. J. J.; Blizanac, B. B.; Arenz, M.; Stamenkovic, V. R.; Ross, P. N.; Markovic, N. M. *J.Phys.Chem.B* **2005**, *109*, 14433-14440.

d) Stamenkovic, V.; Arenz, M.; Blizanac, B. B.; Mayrhofer, K. J. J.; Ross, P. N.; Markovic, N. M. *Surface Science* **2005**, *576*, 145-157.

e) Arenz, M.; Stamenkovic, V. R.; Blizanac, B. B.; Mayrhofer, K. J. J.; Markovic, N. M.; Ross, P. N. *Journal of Catalysis* **2005**, *232*, 402-410.

f) Stamenkovic, V. R.; Mayrhofer, K. J. J.; Moon, B. S.; Arenz, M.; Blizanac, B. B.; Ross, P. N.; Markovic, N. M. *Proceedings Article of Honolulu 206th ECS Meeting, December 21, 2004* **2005**.

g) Stamenkovic, V. R.; Moon, B. S.; Mayrhofer, K. J. J.; Ross, P. N.; Lucas, C. A.; Markovic, N. M. *Nature Materials* **2005**, *(submitted)*.

h) Stamenkovic, V. R.; Moon, B. S.; Mayrhofer, K. J. J.; Ross, P. N.; Markovic, N. M.;Rossmeisel, J.; Greeley, J.; Norskov, J. K. *Angewandte Chemie* **2005**, *(submitted)*.

Karl J.J. Mayrhofer